



Leibniz-Institut für  
Astrophysik Potsdam

Masterarbeit im Studiengang Physik

# Non-thermal Emission from Galaxies

vorgelegt von Maria Werhahn, Matr.-Nr. 380509

Berlin, den 17.08.18

Gutachter: Prof. Dr. Christoph Pfrommer, Prof. Dr. Dieter Breitschwerdt

## Abstract

I developed and tested a framework to calculate the non-thermal emission from simulated galaxies originating from cosmic rays (CR). This comprises the synchrotron, inverse Compton (IC) and bremsstrahlung emission from CR electrons, as well as the gamma-ray emission from neutral pion decay resulting from hadronic interactions of CR protons with the ambient medium. Moreover, the secondary electron and positron production is calculated and their contribution to the non-thermal emission is evaluated. The resulting code is applied to magneto-hydrodynamic simulations of galaxies, which include a self-consistent treatment of CRs, that are injected at remnants of core-collapse supernovae, within a sub-grid physics treatment. Assuming steady-state and neglecting explicit spatial diffusion and advection of CR electrons, we take into account all relevant energy loss processes and obtain an equilibrium spectrum for the primary and secondary electrons and positrons. In addition to the CMB, we also account for the stellar radiation field as seed photons for IC scattering. We show the resulting multifrequency spectra and the corresponding radio- and gamma-ray emission maps for four simulated galaxies, i.e., a dwarf galaxy and a Milky-Way like galaxy at two evolutionary stages, respectively. These indicate a minor contribution of primary to secondary emission. While the obtained luminosities agree with the observed FIR-gamma-ray relation, they can not reproduce the observed FIR-radio correlation, since the magnetic field of the analyzed galaxies is still in the early phase that is characterized by exponential growth. Hence, the magnetic dynamo has not saturated yet, in contrast to the low-redshift galaxies we observe today. Further improvement of the code will enable the post-processing of simulations with higher resolution at more time steps in order to obtain further insight into the underlying physics of the observed FIR-radio and FIR-gamma-ray relations and to test the impact of CR feedback on galaxy formation.

## Zusammenfassung

In dieser Arbeit wurde eine Methodik zur Berechnung der nicht-thermischen Strahlung von simulierten Galaxien entwickelt, die durch kosmische Strahlung (cosmic rays, CR) hervorgerufen wird. Diese beinhaltet Synchrotronstrahlung, Inverse Compton (IC) Strahlung und Bremsstrahlung von CR-Elektronen sowie Gammastrahlung durch den Zerfall von neutralen Pionen, die in hadronischen Interaktionen der CR-Protonen mit dem umgebenden Medium entstehen. Des Weiteren wird der Beitrag der Strahlung von sekundären Elektronen und Positronen berechnet. Der entwickelte Code wird anschließend auf magneto-hydrodynamische Simulationen von Galaxien angewendet, basierend auf einem selbst-konsistenten Modell von CRs, die an der Schockfront von Supernovas injiziert werden. Unter der Annahme eines dynamischen Gleichgewichtszustandes und unter Vernachlässigung von räumlicher Diffusion und Advektion der Elektronen erhalten wir ein Gleichgewichtsspektrum der Elektronen, wobei alle relevanten Energie-Verlustprozesse berücksichtigt werden. Zusätzlich zur kosmischen Hintergrundstrahlung verwenden wir für die IC Streuung auch Photonen des Strahlungsfeldes von Sternen. Schließlich erhalten wir Multifrequenz-Spektren und Emissions-Karten der Radio- und Gammastrahlung für vier simulierte Galaxien: eine Zwerg-Galaxie sowie eine Milchstraßen-ähnliche Galaxie zu jeweils zwei unterschiedlichen Zeitpunkten. Diese deuten darauf hin, dass die primären Elektronen nicht erheblich zur gesamten Strahlung beitragen. Während die erhaltenen Leuchtkräfte mit der beobachteten Relation von Ferninfrarot- zu Gammastrahlung übereinstimmen, können sie die Korrelation von Radio- zu Ferninfrarot-Strahlung nicht reproduzieren, da das Magnetfeld der hier analysierten Galaxien sich noch im frühen Stadium des exponentiellen Wachstums befindet. Daher ist der magnetische Dynamo noch nicht im saturierten Zustand, im Gegensatz zu den heute beobachteten Galaxien bei niedriger Rotverschiebung. Weitere Verbesserungen am Code werden es uns in Zukunft ermöglichen, Simulationen mit besserer Auflösung zu mehreren Zeitpunkten der Entwicklung zu analysieren und somit einen tieferen Einblick in die Physik der beobachteten Relationen von Ferninfrarot-, Gamma- und Radiostrahlung zu erhalten und die Auswirkungen von CRs auf die Entstehung von Galaxien zu untersuchen.

# Contents

<b>1</b>	<b>Introduction</b>	<b>3</b>
<b>2</b>	<b>Non-thermal Emission of Cosmic Rays</b>	<b>4</b>
2.1	Electrons . . . . .	5
2.1.1	Synchrotron Emission . . . . .	5
2.1.2	Inverse Compton Emission . . . . .	12
2.1.3	Relativistic Bremsstrahlung . . . . .	16
2.1.4	Overview and Cross-Check . . . . .	20
2.2	Hadronic Interactions . . . . .	20
2.2.1	Gamma-ray Emission from Neutral Pion Decay . . . . .	23
2.2.2	Secondary Electrons and Positrons . . . . .	30
<b>3</b>	<b>From the Simulation of a Galaxy to its Multi-frequency Spectrum</b>	<b>33</b>
3.1	Steady-State Equation . . . . .	33
3.2	Energy Loss Processes and Timescales . . . . .	36
3.3	Steady-State Spectra and Multi-Frequency Emission from Simulated Galaxies . . . . .	38
<b>4</b>	<b>Results and Discussion</b>	<b>40</b>
<b>5</b>	<b>Conclusion</b>	<b>55</b>
<b>A</b>	<b>Selbstständigkeitserklärung</b>	<b>57</b>
<b>B</b>	<b>Danksagung</b>	<b>57</b>
	<b>References</b>	<b>57</b>

# 1 Introduction

More than 100 years ago, on 7 August 1912, a ballon flight by F. Hess (1912) led to the discovery of cosmic rays (CR). Instead of a decrease, the electroscopes on board measured an increase in ionization of the atmosphere with altitude, suggesting that the origin of this finding is non-terrestrial. Still, the nature of these particles remained unclear. Today we know that most of CR particles constitute of ionized nuclei, about 90% protons, 9% alpha particles and a few heavier nuclei, as well as a small fraction of electrons, positrons and antiprotons (Gaisser 1990). Their energy spectrum, i.e., the number of particles at energy  $E$  in an interval  $dE$ , is measured to be a power law. It ranges from a few hundred MeV up to  $10^{20}$  eV, hence, CRs are relativistic particles, a few of them are even ultra-relativistic. At around  $10^{15}$  eV, the differential spectrum has a characteristic feature that is called “knee”, where it changes its slope from a spectral index of around  $-2.7$  to  $-3.1$ . It flattens again to a spectral index of  $-2.6$  at around  $10^{18}$  eV at the so called “ankle”. This corresponds to a huge change in the integral flux, i.e., the number of particles incident per unit time, area and steradian. Whereas at  $\sim 1$  TeV, about  $10^5$  particles per square kilometer, second and steradian reach the earth’s atmosphere, only 1 particle per square kilometer and per steradian arrives per century with an energy of  $\sim 10^{20}$  eV (Beig et al. 2001). Despite the rarity of these high energetic particles, since only 1 out of  $10^9$  interstellar particles is a cosmic ray particle, their energy density is comparable to that of thermal particles (Zweibel 2013). Hence, they inevitably play a crucial role in galaxy formation and evolution, e.g., by driving galactic winds (Breitschwerdt et al. 1991). Up to the ankle, cosmic rays are assumed to be accelerated in core-collapse supernovae (SN), driving strong shocks in the interstellar medium (ISM), and therefore being of Galactic origin. Beyond the ankle though, they do not seem to be confined to the Galaxy, since the gyro radii of these highly relativistic particles are larger than the size of the Galaxy. Hence, the source of these CRs has to be extragalactic. The very low-energy part of the CR spectrum on the other hand is modified by interactions of the charged particles with the magnetic field of solar winds, that prevents them to reach the Earth up to an energy per unit charge  $Z$  of a particle of around  $10 \text{ GeV}/Z$ , above which the impact of solar winds can be neglected (Gaisser 1990).

The strong connection between CRs and the physical properties of a galaxy can be deduced from observationally obtained relations, such as a tight linear correlation between the star formation rate (SFR) and radio luminosities, as well the gamma-ray luminosities of star-forming galaxies. Since CRs contain relativistic electrons interacting with magnetic fields, they emit synchrotron radiation, which is mainly visible in radio wavelengths. The young stellar population of massive stars in actively star-forming galaxies leads to core-collapse SN explosion, which drive the acceleration of CRs and thus the emission of radio synchrotron radiation. Moreover, the radiation from stars is mainly emitted in form of ultraviolet (UV) light, which is reradiated in the far-infrared (FIR) due to the absorption by dust grains. Assuming the galaxy to be optically thick to UV radiation and assuming an universal electron acceleration efficiency at supernova remnants (SNR), the radio emission is thus a calorimetric measure of the star formation rate of a galaxy. Furthermore, the CR electron population also interacts with the ambient radiation field from stars, dust and the cosmic microwave background (CMB). These seed photons can scatter off of the highly relativistic leptons and thus lead to X-Ray or gamma-ray emission. As a consequence of free-free transitions of the electrons in the electrostatic field of ions in the ISM, relativistic bremsstrahlung contributes to the radiation spectrum as well. Another contribution to the gamma-ray emission originates from the hadronic interactions of the CR proton population with the ambient medium, leading to the creation of pions that subsequently decay into two gamma-ray photons, if the pions are neutral. Consequently, the gamma-ray luminosities of star-forming galaxies are similarly linked to the SFR and thus also the FIR emission. However, the positively and negatively charged pions produced in proton-proton collisions decay further into muons and hence constitute a source of secondary electrons and also positrons. These again undergo the same radiation processes as the so called primary electrons, that have been directly injected into the ISM. The surprisingly tight relation and the normalization of these relations give fundamental insights into the physical processes happening in galaxies with properties in a large dynamical range. In case of the FIR-radio correlation, it spans over five decades in luminosity and gas surface density (e.g. van der Kruit 1971, 1973; Condon 1992; Bell 2003) and it holds also on smaller scales of a few hundred parsecs, not only for the entire galaxy (e.g. Beck and Golla 1988; Bica and Helou 1990; Murphy et al. 2008).

The goal of this work is to develop a tool that calculates the multifrequency non-thermal emission from a given CR proton and electron distribution. This distribution is not required to be a simple power law, since due to energy loss processes the spectra can be modified. Therefore, we first derive the required formulas for the leptonic radiation processes, before we discuss different models for the description of hadronic interactions. From this we obtain also the hadronic contribution to the non-thermal emission, which comprises the gamma-ray emission from neutral pion decay and the emission from secondary electrons and positrons. This code is then used for the post-processing of hydrodynamical galaxy simulations. Consequently, we obtain spatially and temporally resolved overall emission spectra of simulated galaxies that can be used to reconcile the existing models and compare the results to observations.

## 2 Non-thermal Emission of Cosmic Rays

As already mentioned, the distribution of CRs is observed to be a power-law distribution, which can be motivated by the following considerations (see e.g. Bell 1978; Gaisser 1990). In the process of first-order Fermi acceleration (Fermi 1949), a charged particle gains energy in each scattering process back and forth an astrophysical shock front, where the post-shock medium acts as an approaching mirror. If the particle gains an amount of energy that is proportional to its energy,  $\Delta E = \xi E$ , it has after  $n$  encounters the energy  $E_n = (1 + \xi)^n E_0$ . Rearranging this gives the number of encounters needed to obtain an energy  $E$  as

$$n = \frac{\ln\left(\frac{E}{E_0}\right)}{\ln(1 + \xi)}. \quad (1)$$

The probability, that this same particle is after  $n$  encounters still participating in this process, is given by  $(1 - P_{\text{esc}})^n$ , where the escape probability is denoted by  $P_{\text{esc}}$ . Hence, we can sum over  $m \geq n$  to obtain the number of particles that have an energy larger than  $E$ :

$$N(> E) \propto \sum_{m=n}^{\infty} (1 - P_{\text{esc}})^m = (1 - P_{\text{esc}})^n \sum_{m=0}^{\infty} (1 - P_{\text{esc}})^m. \quad (2)$$

This can be further simplified by using the geometrical series to yield the expression

$$N(> E) \propto (1 - P_{\text{esc}})^n \frac{1}{1 - (1 - P_{\text{esc}})} = \frac{(1 - P_{\text{esc}})^n}{P_{\text{esc}}}. \quad (3)$$

After substituting equ. (1) for  $n$  we can rewrite this as the desired power law

$$N(> E) \propto \frac{1}{P_{\text{esc}}} \left(\frac{E}{E_0}\right)^{-\tilde{a}}, \quad (4)$$

with

$$\tilde{a} = \frac{\ln\left(\frac{1}{1 - P_{\text{esc}}}\right)}{\ln(1 + \xi)} \approx \frac{P_{\text{esc}}}{\xi}. \quad (5)$$

It can be further derived that  $P_{\text{esc}} \approx 4v_2/c$  and  $\xi = 4(v_2 - v_1)/(3c)$ , where  $v_1$  is the velocity of the approaching gas ('upstream') and  $v_2$  the velocity of the shocked gas ('downstream') in the rest frame of the shock. Hence, we obtain the spectral index for the cumulative distribution

$$\tilde{a} = \frac{3}{\frac{v_1}{v_2} - 1}, \quad (6)$$

which yields for the differential spectrum an index  $a = \tilde{a} + 1$ . For a strong shock, the ratio  $v_1/v_2 = 4$  and hence  $a = 2$ , which is very close to the observed spectral index of galactic CRs.

In the following, we define the differential CR particle spectrum per unit volume as a power law in momentum

$$N_i(p_i) = \frac{d^2 N_i}{dp_i dV} = C_i p_i^{-a_i} \theta(p_i - q_i), \quad (7)$$

where the index  $i = \{e, p\}$  represents either electrons or protons. Here,  $C_{e,p}$  gives the normalization of the spectrum,  $q$  denotes the lower momentum cut-off of the distribution and  $\theta$  is the Heaviside step function. We normalize the momentum  $p_e$  to  $m_e c$  for the distribution of electrons and  $p_p$  to  $m_p c$  for the distribution of protons. Note that in the literature, the power-law distribution is frequently given as a distribution in energy, i.e., as a function of the Lorentz factor  $\gamma_{e,p} = \sqrt{1 + p_{e,p}^2} = E/(m_{e,p} c^2)$ . Only in the relativistic limit  $p \gg 1$ , this yields the same spectrum. The normalization of the proton spectrum can be obtained from the energy density of the CR population

$$\begin{aligned} \varepsilon_{\text{CR}} &= \int_0^\infty dp_p N_p(p_p) E_{\text{kin}}(p_p) \\ &= \frac{C_p q^{1-a_p}}{a_p - 1} \left[ \frac{1}{2} B_x \left( \frac{a_p - 2}{2}, \frac{3 - a_p}{2} \right) + q^{1-a_p} \left( \sqrt{1 + q^2} - 1 \right) \right], \end{aligned}$$

where  $B_x(a, b)$  with  $x = 1/(1 + q^2)$  denotes the incomplete Beta function and the kinetic energy is given by  $E_{\text{kin}}(p_p) = \left( \sqrt{1 + p_p^2} - 1 \right) m_p c^2$ . We define the ratio of electrons to protons  $K_{ep}$  as the ratio of the differential distributions at a momentum  $p_0$  that is given in units of  $m_p c$ , i.e.,

$$K_{ep} = \frac{N_e \left( \frac{p_0 m_p c}{m_e c} \right) dp_e}{N_p(p_0) dp_p}. \quad (8)$$

Using  $dp_e = dp_p m_p / m_e$  and the definitions for the momentum distributions with the same power law index  $a$ , this yields

$$K_{ep} = \frac{C_e \left( \frac{p_0 m_p}{m_e} \right)^{-a} m_p}{C_p (p_0)^{-a} m_e} = \frac{C_e}{C_p} \left( \frac{m_p}{m_e} \right)^{-a+1}. \quad (9)$$

The non-thermal emission processes of electrons that are distributed according to such a continuous power law distribution can be described analytically, under the assumption of highly relativistic electrons and a spectrum with no cut-off. In reality though, the initial simple power law CR electron spectrum is modified due to several energy loss processes (see Section 3.2). Hence, we aim to calculate the emission spectrum for a general distribution of electrons, that we approximate by a binned spectrum in logarithmic scale.

## 2.1 Electrons

Highly relativistic electrons experience different processes that lead to the emission of non-thermal radiation. These are being discussed in the following, where the derivations of the formulas mainly follow the calculations by Rybicki and Lightman (1986) and Longair (2011), as not stated otherwise in the text.

### 2.1.1 Synchrotron Emission

When charged particles are accelerated by a magnetic field, they radiate according to Larmor's formula. While cyclotron radiation from non-relativistic particles emits the frequency that corresponds to the frequency of gyration, the so called synchrotron radiation is generated by relativistic particles and the emission spectrum is much more complex.

Starting with the motion of a particle that gyrates around a magnetic field with frequency  $\omega_B = qB/(\gamma mc)$  we have the equation of motion:

$$m\gamma \frac{d\mathbf{v}}{dt} = \frac{q}{c} \mathbf{v} \times \mathbf{B}. \quad (10)$$

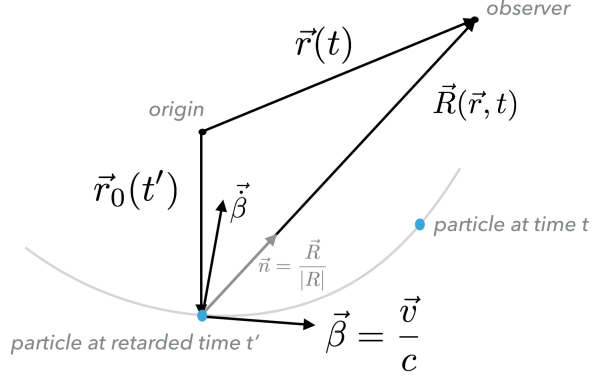


Figure 1: Geometry for calculating the radiation of an accelerated charged particle, following Rybicki and Lightman (1986)

This shows that particles are only accelerated perpendicular to the magnetic field. Larmor's formula for the emission of a singly accelerated charge  $q$  yields the emitted power

$$P = \frac{2q^2 \dot{\mathbf{v}}'^2}{3c^3}, \quad (11)$$

where the acceleration  $\dot{\mathbf{v}}'$  of the particle is evaluated in its rest frame. Using the transformations  $\dot{\mathbf{v}}'_{\parallel} = \gamma^3 \dot{\mathbf{v}}_{\parallel}$  and  $\dot{\mathbf{v}}'_{\perp} = \gamma^2 \dot{\mathbf{v}}_{\perp}$ , we obtain

$$P = \frac{2q^2}{3c^3} \gamma^4 (\dot{\mathbf{v}}_{\perp}^2 + \gamma^2 \dot{\mathbf{v}}_{\parallel}^2). \quad (12)$$

Since the acceleration only has a component perpendicular to the magnetic field, i.e.  $\dot{\mathbf{v}}_{\parallel} = 0$ , and  $\dot{\mathbf{v}}_{\perp} = \omega_B \mathbf{v}_{\perp}$ , the total emitted radiation is given by

$$P = \frac{2q^2}{3c^3} \gamma^2 \frac{B^2}{m^2 c^4} v_{\perp}^2. \quad (13)$$

This can be averaged over an isotropic distribution of velocities,  $\langle v_{\perp}^2 \rangle = v^2 \int \sin^2 \alpha d\Omega / 4\pi = 2v^2/3$ , which yields for the emitted power

$$P_{\text{sync}} = \frac{4}{3} \sigma_{\text{T}} c \beta^2 \gamma^2 u_B, \quad (14)$$

where the magnetic energy density is  $u_B = B^2/(8\pi)$  and the Thomson cross-section is  $\sigma_{\text{T}} = 8\pi r_0^2/3$ . For a specific pitch angle, which is the angle between the magnetic field and the velocity of the particle, the total emitted radiation is

$$P = \frac{2q^4 B^2 \gamma^2 \beta^2 \sin^2 \alpha}{3m^2 c^3}. \quad (15)$$

After these general considerations, we calculate the frequency dependence of the emitted radiation, i.e. the spectrum of synchrotron emission. Starting from the Liénard-Wichert potentials one can derive an expression for the electric field of a relativistically moving accelerated charge as follows

$$\mathbf{E}(\mathbf{r}, t) = \frac{q}{c} \left\{ \frac{\mathbf{n}}{\kappa^3 R} \times [(\mathbf{n} - \boldsymbol{\beta}) \times \dot{\boldsymbol{\beta}}] \right\}, \quad (16)$$

where the definition of the used vectors can be seen in Fig. 1 with  $\boldsymbol{\beta} = \mathbf{v}/c = \mathbf{r}_0/c$  and  $\kappa = 1 - \mathbf{n} \cdot \boldsymbol{\beta}$ . This enables us to derive the energy per unit frequency per unit solid angle as

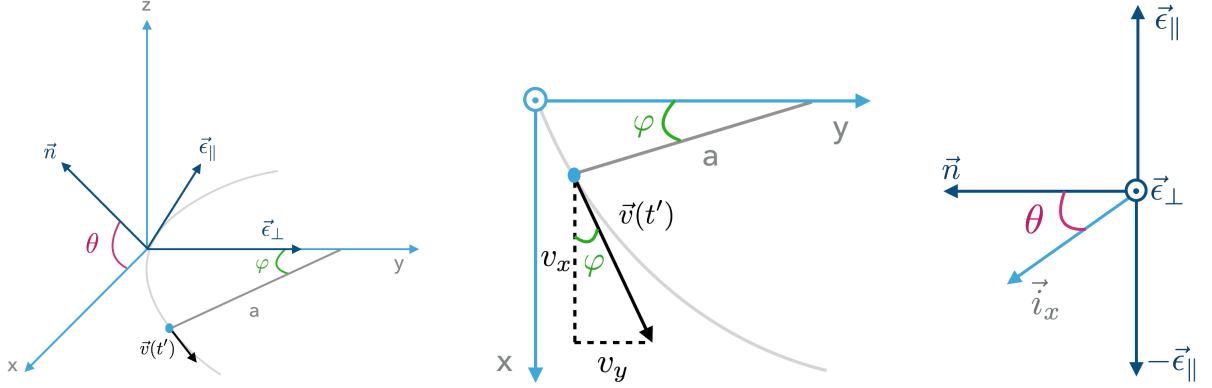


Figure 2: Graphical representation for calculating the synchrotron emission, following Rybicki and Lightman (1986)(left) and as seen from the  $z$ -direction (middle) and in the new coordinate system (right).

$$\frac{dW}{d\omega d\Omega} = \frac{c}{4\pi^2} \left| \int [R\mathbf{E}(t')] e^{i\omega t} dt \right|^2 = \frac{q^2}{4\pi^2 c} \left| \left[ \mathbf{n} \times \left\{ (\mathbf{n} - \boldsymbol{\beta}) \times \dot{\boldsymbol{\beta}} \right\} \kappa^{-3} \right] e^{i\omega t} dt \right|^2, \quad (17)$$

where the retarded time  $t' = t - R(t')/c$  is the time when the radiation was emitted, which is received at time  $t$  at a distance  $R$  of the observer. Assuming that the observer is far away from the origin and the observed particle, i.e.  $|\mathbf{r}_0| \ll |\mathbf{r}|$ , it follows that  $R(t') \approx |\mathbf{r}| - \mathbf{n} \cdot \mathbf{r}_0(t')$  and the variable of integration can be changed to

$$dt = dt' \left( 1 + \frac{dR(t')}{dt'} \frac{1}{c} \right) = dt' (1 - \mathbf{n} \cdot \boldsymbol{\beta}) = \kappa dt'.$$

Therefore, we have

$$\frac{dW}{d\omega d\Omega} = \frac{q^2}{4\pi^2 c} \left| \int_{-\infty}^{\infty} \left[ \mathbf{n} \times \left\{ (\mathbf{n} - \boldsymbol{\beta}) \times \dot{\boldsymbol{\beta}} \right\} \kappa^{-2} \right] e^{i\omega(t' - \mathbf{n} \cdot \mathbf{r}_0(t')/c)} dt' \right|^2. \quad (18)$$

The expression in squared brackets can be further simplified by evaluating  $\frac{d}{dt} [\kappa^{-1} (\mathbf{n} \times (\mathbf{n} \times \boldsymbol{\beta}))] = \mathbf{n} \times [(\mathbf{n} - \boldsymbol{\beta}) \times \dot{\boldsymbol{\beta}}] \kappa^{-2}$ . This makes it easy to perform an integration by parts, which yields

$$\begin{aligned} \frac{dW}{d\omega d\Omega} &= \frac{q^2}{4\pi^2 c} \left| \int_{-\infty}^{\infty} [\kappa^{-1} (\mathbf{n} \times (\mathbf{n} \times \boldsymbol{\beta}))] i\omega \kappa e^{i\omega(t' - \mathbf{n} \cdot \mathbf{r}_0(t')/c)} dt' \right|^2 \\ &= \frac{q^2 \omega^2}{4\pi^2 c} \left| \int_{-\infty}^{\infty} [(\mathbf{n} \times (\mathbf{n} \times \boldsymbol{\beta}))] e^{i\omega(t' - \mathbf{n} \cdot \mathbf{r}_0(t')/c)} dt' \right|^2. \end{aligned} \quad (19)$$

In the next step, the factor  $\mathbf{n} \times (\mathbf{n} \times \boldsymbol{\beta})$  needs to be further evaluated. Therefore, a new coordinate system is chosen that makes the calculation more convenient. At time  $t' = 0$  the origin of the coordinate system is placed on the particle, with the radius of its orbit at that time lying in the  $x$ - $y$ -plane. At time  $t'$  it forms an angle with the  $y$ -axis  $\varphi = vt'/a$ . The unit vector  $\mathbf{n}$ , which points towards the observer, forms the new coordinate system together with the unit vector  $\boldsymbol{\epsilon}_\perp$ , which is parallel to the  $y$ -axis, and a third unit vector  $\boldsymbol{\epsilon}_\parallel = \mathbf{n} \times \boldsymbol{\epsilon}_\perp$ . The  $x$ - and  $y$ -components of the velocity are easy to obtain from Fig. 2 and read  $\mathbf{v}_x = \mathbf{i}_x |\mathbf{v}_x| = \mathbf{i}_x |\mathbf{v}| \cos \varphi$  and  $\mathbf{v}_y = \mathbf{i}_y |\mathbf{v}_y| = \boldsymbol{\epsilon}_\perp |\mathbf{v}| \sin \varphi$  with  $\mathbf{i}_x$  and  $\mathbf{i}_y$  being the unit vectors along the  $x$ - and  $y$ -axis. According to the right panel of Fig. 2, the unit vector in  $x$ -direction can be expressed

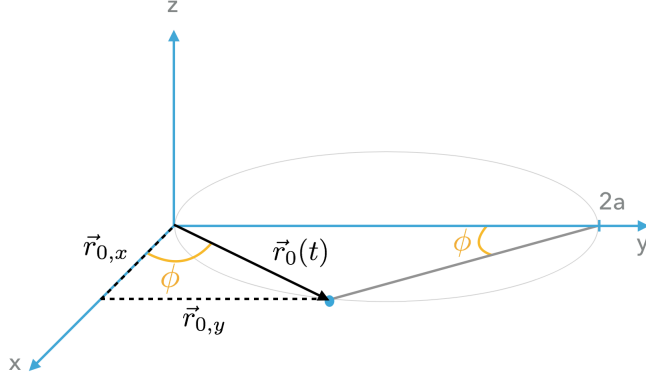


Figure 3: Geometry of the orbit of an accelerated charged particle.

in terms of the new coordinate system as  $\mathbf{i}_x = \mathbf{n} \cos \theta - \boldsymbol{\epsilon}_{\parallel} \sin \theta$  such that  $\mathbf{v}_x = |\mathbf{v}| \cos \varphi (\mathbf{n} \cos \theta - \boldsymbol{\epsilon}_{\parallel} \sin \theta)$ . Using this, the velocity vector can be written as

$$\mathbf{v} = \mathbf{v}_x + \mathbf{v}_y = |\mathbf{v}| (\boldsymbol{\epsilon}_{\perp} \sin \varphi + \mathbf{n} \cos \theta \cos \varphi - \boldsymbol{\epsilon}_{\parallel} \sin \theta \cos \varphi). \quad (20)$$

Taking the cross product of  $\mathbf{n}$  and  $\boldsymbol{\beta} = \mathbf{v}/c$  gives

$$\mathbf{n} \times \boldsymbol{\beta} = \frac{v}{c} (\boldsymbol{\epsilon}_{\parallel} \sin \varphi + \boldsymbol{\epsilon}_{\perp} \sin \theta \cos \varphi), \quad (21)$$

with  $v = |\mathbf{v}|$  and where we have made use of the relations  $\boldsymbol{\epsilon}_{\parallel} = \mathbf{n} \times \boldsymbol{\epsilon}_{\perp}$ ,  $\boldsymbol{\epsilon}_{\perp} = -\mathbf{n} \times \boldsymbol{\epsilon}_{\parallel}$  and  $\mathbf{n} \times \mathbf{n} = \mathbf{0}$ . By applying them again, we finally get for the first factor of equ. (19) the expression

$$\mathbf{n} \times (\mathbf{n} \times \boldsymbol{\beta}) = \frac{v}{c} (\boldsymbol{\epsilon}_{\parallel} \sin \theta \cos \varphi - \boldsymbol{\epsilon}_{\perp} \sin \varphi). \quad (22)$$

For the argument of the exponential function in the second factor of equ. (19) we need an expression for  $\mathbf{r}_0(t)$  in terms of the new coordinate system. As can be seen from Fig. 3, the  $x$ - and  $y$ -components of this vector are given by  $\mathbf{r}_{0,x} = \mathbf{i}_x |\mathbf{r}_0| \cos \phi$  and  $\mathbf{r}_{0,y} = \mathbf{i}_y |\mathbf{r}_0| \sin \phi$ , where, again,  $\mathbf{i}_y = \boldsymbol{\epsilon}_{\perp}$  and  $\mathbf{i}_x = \mathbf{n} \cos \theta - \boldsymbol{\epsilon}_{\parallel} \sin \theta$ . Furthermore, we also see from Fig. 3 that  $|\mathbf{r}_0| = 2a \sin \phi$ , so that we get

$$\mathbf{r}_0(t) = \mathbf{r}_{0,x} + \mathbf{r}_{0,y} = 2a \sin \phi (\mathbf{n} \cos \theta \cos \phi - \boldsymbol{\epsilon}_{\parallel} \sin \theta \cos \phi + \boldsymbol{\epsilon}_{\perp} \sin \phi). \quad (23)$$

This reduces to  $\mathbf{n} \cdot \mathbf{r}_0(t) = 2a \sin \phi \cos \theta \cos \phi$ , since  $\mathbf{n} \cdot \boldsymbol{\epsilon}_{\parallel} = \mathbf{n} \cdot \boldsymbol{\epsilon}_{\perp} = 0$ . After noticing from Fig. 3 that  $\phi = vt'/(2a)$ , we get for the argument of the second factor

$$t' - \frac{\mathbf{n} \cdot \mathbf{r}_0(t')}{c} = t' - \frac{2a}{c} \sin \left( \frac{vt'}{2a} \right) \cos \left( \frac{vt'}{2a} \right) \cos \theta. \quad (24)$$

Note that there is a typo in this equation in Longair (2011) in his equation (8.34). Since synchrotron radiation is strongly beamed, which means that it is emitted into a cone with half opening angle  $\sim 1/\gamma \ll 1$  and we can only see radiation for small values of  $\theta$ , which also corresponds to small values of  $\varphi = vt'/a$  and  $\phi = vt'/(2a)$ , as can be seen from Fig. 2, we can expand all expressions up to third order in  $\theta$ ,  $\phi$  and  $\varphi$ , that is

$$\begin{aligned} \sin x &\simeq x - \frac{x^3}{3!} + \dots \\ \cos x &\simeq 1 - \frac{x^2}{2!} + \dots \end{aligned} \quad (25)$$

We insert these expressions into equ. (24) to obtain

$$t' - \frac{\mathbf{n} \cdot \mathbf{r}_0(t')}{c} = t' \left(1 - \frac{v}{c}\right) + \frac{v}{c} \frac{\theta^2}{2} t' + \frac{v^3}{6ca^2} t'^3 \quad (26)$$

For highly relativistic particles, as  $v$  approaches  $c$ , we can use the approximation

$$1 - \frac{v}{c} = \frac{1 - \frac{v^2}{c^2}}{1 + \frac{v}{c}} \approx \frac{1}{2\gamma^2} \quad (27)$$

and set  $v = c$  elsewhere. Thus, we have

$$t' - \frac{\mathbf{n} \cdot \mathbf{r}_0(t')}{c} = \frac{1}{2\gamma^2} \left[ t'(1 + \gamma^2\theta^2) + \frac{c^3}{6a^2} t'^3 \right]. \quad (28)$$

The small angle approximation to first order leads in equ. (22) to the expression

$$\mathbf{n} \times (\mathbf{n} \times \boldsymbol{\beta}) \simeq -\frac{vt'}{a} \boldsymbol{\epsilon}_\perp + \theta \boldsymbol{\epsilon}_\parallel. \quad (29)$$

We now combine equ. (28) and (29) with equ. (19) to get the emitted spectrum in the  $\boldsymbol{\epsilon}_\perp$ - and  $\boldsymbol{\epsilon}_\parallel$ -direction to be

$$\frac{dW_\parallel}{d\omega d\Omega} = \frac{q^2 \omega^2 \theta^2}{4\pi^2 c} \left| \int_{-\infty}^{\infty} \exp \left\{ \frac{i\omega}{2\gamma^2} \left[ t'(1 + \gamma^2\theta^2) + \frac{c^2}{6a^2} t'^3 \right] \right\} dt' \right|^2, \quad (30)$$

$$\frac{dW_\perp}{d\omega d\Omega} = \frac{q^2 \omega^2}{4\pi^2 c} \left| \int_{-\infty}^{\infty} \frac{ct'}{a} \exp \left\{ \frac{i\omega}{2\gamma^2} \left[ t'(1 + \gamma^2\theta^2) + \frac{c^2}{6a^2} t'^3 \right] \right\} dt' \right|^2. \quad (31)$$

In order to perform the integration over  $t'$ , it is useful to substitute  $\theta_\gamma^2 = 1 + \gamma^2\theta^2$ ,  $y = \gamma ct'/a\theta_\gamma$  and  $\eta = \omega a \theta_\gamma^3 / 3c\gamma^3$  to get  $dt' = a\theta_\gamma dy / \gamma c$  and

$$\frac{dW}{d\omega d\Omega} = \frac{q^2 \omega^2 \theta^2}{4\pi^2 c} \left( \frac{a\theta_\gamma}{\gamma c} \right)^2 \left| \int_{-\infty}^{\infty} \exp \left[ \frac{3}{2} i\eta \left( y + \frac{1}{3} y^3 \right) \right] dy \right|^2, \quad (32)$$

$$\frac{dW_\perp}{d\omega d\Omega} = \frac{q^2 \omega^2 \theta_\gamma^2}{4\pi^2 c \gamma^2} \left( \frac{a\theta_\gamma}{\gamma c} \right)^2 \left| \int_{-\infty}^{\infty} y \exp \left[ \frac{3}{2} i\eta \left( y + \frac{1}{3} y^3 \right) \right] dt' \right|^2. \quad (33)$$

Using now the relation  $e^{ix} = \cos x + i \sin x$  and the fact that  $\sin x$  and  $x \cos x$  are odd functions, we are only left with two integrals that can be evaluated with formulas (10.4.22) fo (10.4.32) from Abramowitz and Stegun (1965),

$$\begin{aligned} \int_{-\infty}^{\infty} \cos \left[ \frac{3}{2} \eta \left( y + \frac{1}{3} y^3 \right) \right] dy &= \frac{2}{\sqrt{3}} K_{1/3}(\eta), \\ \int_{-\infty}^{\infty} y \sin \left[ \frac{3}{2} \eta \left( y + \frac{1}{3} y^3 \right) \right] dy &= \frac{2}{\sqrt{3}} K_{2/3}(\eta). \end{aligned} \quad (34)$$

This yields

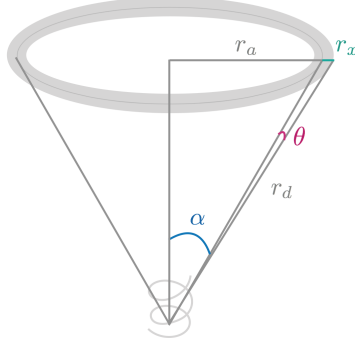


Figure 4: Schematic illustration of synchrotron emission, following Rybicki and Lightman (1986)

$$\begin{aligned}\frac{dW_{\parallel}}{d\omega d\Omega} &= \frac{q^2\omega^2\theta^2}{3\pi^2c} \left(\frac{a\theta\gamma}{\gamma c}\right)^2 K_{1/3}^2(\eta), \\ \frac{dW_{\perp}}{d\omega d\Omega} &= \frac{q^2\omega^2}{3\pi^2c} \left(\frac{a\theta^2\gamma}{\gamma^2c}\right)^2 K_{2/3}^2(\eta).\end{aligned}\quad (35)$$

Over one full period of the electron orbiting around the magnetic field, the solid angle of the emitted radiation can be approximated by  $d\Omega \approx 2\pi r_a dr_x/r_d^2 = 2\pi \sin\alpha d\theta$  (with  $\sin\alpha = r_a/r_d$  and  $d\theta = dr_x/r_d$ , see Fig. 4) since the radiation is confined to a very small angle  $\theta \sim 1/\gamma$  as already mentioned above. Therefore, the integration over solid angle yields

$$\begin{aligned}\frac{dW}{d\omega} &= \frac{2q^2\omega^2a^2 \sin\alpha}{3\pi c^3\gamma^2} \int \theta^2 \theta_{\gamma}^2 K_{1/3}^2(\eta) d\theta, \\ \frac{dW_{\perp}}{d\omega} &= \frac{2q^2\omega^2a^2 \sin\alpha}{3\pi c^3\gamma^4} \int \theta_{\gamma}^2 K_{2/3}^2(\eta) d\theta,\end{aligned}\quad (36)$$

where the limits can be taken to be from  $-\infty$  to  $\infty$  as the integrand is concentrated to small values of  $\theta$ . The following integrals have been obtained by Westfold (1959) and read

$$\begin{aligned}\int_{-\infty}^{\infty} \theta_{\gamma}^4 K_{2/3}^2\left(\frac{x}{2}\theta_{\gamma}^3\right) d\theta &= \frac{\pi}{\sqrt{3}\gamma x} \left[ \int_x^{\infty} K_{5/3}(z) dz + K_{2/3}(x) \right], \\ \int_{-\infty}^{\infty} \gamma^2 \theta^2 \theta_{\gamma}^2 K_{1/3}^2\left(\frac{x}{2}\theta_{\gamma}^3\right) d\theta &= \frac{\pi}{\sqrt{3}\gamma x} \left[ \int_x^{\infty} K_{5/3}(z) dz - K_{2/3}(x) \right],\end{aligned}\quad (37)$$

where  $x = \omega/\omega_c = 2\omega a/(3c\gamma^3)$ , the critical frequency is  $\omega_c = 3/2 \gamma^3 \omega_B \sin\alpha$  and the frequency of gyration is  $\omega_B = qB/(\gamma m_e c)$ . Using these relations in equ. (36) and defining  $F(x) = x \int_x^{\infty} K_{5/3}(x) dx$  and  $G(x) = x K_{2/3}(x)$  gives

$$\begin{aligned}\frac{dW_{\parallel}}{d\omega} &= \frac{\sqrt{3}q^2\gamma \sin\alpha}{2c} [F(x) - G(x)], \\ \frac{dW_{\perp}}{d\omega} &= \frac{\sqrt{3}q^2\gamma \sin\alpha}{2c} [F(x) + G(x)].\end{aligned}\quad (38)$$

This has to be divided by  $T = 2\pi/\omega_B = 2\pi\gamma m_e c/(qB)$  in order to account for the fact that we calculated the emission during a full period of the electron orbiting around the magnetic field. Then, the sum of the two components yields the total emissivity of the radiation

$$\begin{aligned}\frac{dW}{d\omega dt} &= \frac{1}{T} \left( \frac{dW_{\parallel}}{d\omega} + \frac{dW_{\perp}}{d\omega} \right) \\ &= \frac{\sqrt{3}q^3 B \sin \alpha}{2\pi m_e c^2} F(x),\end{aligned}\quad (39)$$

which is the emitted power per unit volume and unit frequency for a highly relativistic electron and is also often called  $P(\omega)$ .

The function  $F(x) = x \int_x^{\infty} K_{5/3}(\xi) d\xi$  contains the modified Bessel function of second kind of order  $5/3$ . This now has to be integrated over a given electron-distribution. For a given distribution of electrons  $N(\gamma)$ , we integrate this expression over the distribution of all electrons to get the total emission spectrum

$$P_{\text{tot}}(\omega) = \frac{\sqrt{3}e^3 B}{2\pi m_e c^2} \sin \alpha \int_0^{\infty} N(\gamma) F\left(\frac{\omega}{\omega_c}\right) d\gamma. \quad (40)$$

For a power-law distribution of electrons that is given by  $N(\gamma) = C\gamma^{-a}$ , the integral can be calculated analytically. Therefore, one changes the variable  $\gamma$  to  $x = \omega/\omega_c = 2mc\omega/(3\gamma^2 eB \sin \alpha)$  with  $d\gamma/dx = -1/2 [2mc\omega/(3x^3 eB \sin \alpha)]^{0.5}$  such that equ. (40) becomes

$$P_{\text{tot}}(\omega) = \frac{\sqrt{3}e^3 C B \sin \alpha}{4\pi m_e c^2} \left( \frac{2m_e c \omega}{3eB \sin \alpha} \right)^{-\frac{a-1}{2}} \int_0^{\infty} x^{\frac{a-3}{2}} F(x) dx. \quad (41)$$

Using the relation

$$\int_0^{\infty} x^{\mu} F(x) dx = \frac{2^{\mu+1}}{\mu+2} \Gamma\left(\frac{\mu}{2} + \frac{7}{3}\right) \Gamma\left(\frac{\mu}{2} + \frac{2}{3}\right) \quad (42)$$

we obtain for the emitted spectrum of a power law distribution of electrons for a fixed pitch angle  $\alpha$  the expression

$$P_{\text{tot}}(\omega) = \frac{\sqrt{3}e^3 C B \sin \alpha}{2\pi m_e c^2 (a+1)} \left( \frac{m_e c \omega}{3eB \sin \alpha} \right)^{-\frac{a-1}{2}} \Gamma\left(\frac{p}{4} + \frac{19}{12}\right) \Gamma\left(\frac{p}{4} - \frac{1}{12}\right). \quad (43)$$

This can be further evaluated for an isotropic distribution of pitch angles

$$\frac{1}{2} \int_0^{\pi} \sin^{(a+3)/2}(\alpha) d\alpha = \frac{\sqrt{\pi}}{2} \frac{\Gamma(\frac{p+5}{4})}{\Gamma(\frac{p+7}{4})} \quad (44)$$

to yield

$$P_{\text{tot}}(\omega) = \frac{dE}{dt d\omega dV} = \frac{\sqrt{3}\pi}{16\pi} \frac{C e^3}{m_e c^2} \frac{(a + \frac{7}{3}) \Gamma(\frac{3a+7}{12}) \Gamma(\frac{3a-1}{12}) \Gamma(\frac{a+5}{4})}{a+1 \Gamma(\frac{a+7}{4})} B \left( \frac{m_e c \omega}{3eB} \right)^{-\frac{a-1}{2}}. \quad (45)$$

Since we are not going to have a continuous distribution of electrons, but a binned spectrum, it is useful to derive the corresponding formulas. Starting from equ. (40) and inserting in the function  $F(x)$  and the definition for  $\omega_c$ , we obtain

$$P_{\text{tot}}(\omega) = \frac{e^2 \omega}{\sqrt{3}\pi c} \int_0^{\infty} \frac{1}{\gamma^2} N(\gamma) \int_{\omega/\omega_c}^{\infty} K_{5/3}(\xi) d\xi d\gamma. \quad (46)$$

Note that  $\omega/\omega_c = 2mc\omega/(3\gamma^2 eB \sin \alpha)$  is a function of  $\gamma$  and  $\alpha$ . If the given energy distribution of electrons  $N(\gamma_i) = A_i$  is a constant for each energy bin  $i$ , the limits of the first integral in equ. (46) are

the boundaries of each bin, respectively, and the total emission is then given by the sum over all integrals in the energy bins:

$$P_{\text{tot}}(\omega) = \frac{e^2\omega}{\sqrt{3}\pi c} \sum_i A_i \int_{\gamma_{a,i}}^{\gamma_{b,i}} \frac{1}{\gamma^2} \int_{\omega/\omega_c}^{\infty} K_{5/3}(\xi) d\xi d\gamma \quad (47)$$

This double integral is computationally expensive and has to be further simplified. Therefore, we define  $f'(\gamma) = \gamma^{-2}$  and  $g(\gamma) = \int_{\omega/\omega_c}^{\infty} K_{5/3}(\xi) d\xi$  to perform integration by parts

$$\int_{\gamma_{a,i}}^{\gamma_{b,i}} f'(\gamma)g(\gamma)d\gamma = \left[ -\frac{1}{\gamma}g \right]_{\gamma_{a,i}}^{\gamma_{b,i}} - \int_{\gamma_{a,i}}^{\gamma_{b,i}} f(\gamma)g'(\gamma)d\gamma. \quad (48)$$

For the calculation of  $g'(\gamma)$  the Leibniz integral rule can be applied, such that, with  $K_{5/3}(x) \rightarrow 0$  for  $x \rightarrow \infty$  one obtains

$$g'(\gamma) = -\frac{d}{d\gamma} \left( \frac{2mc\omega}{3\gamma^2 eB \sin \alpha} \right) K_{5/3} \left( \frac{2mc\omega}{3\gamma^2 eB \sin \alpha} \right) = \frac{4mc\omega}{3\gamma^3 eB \sin \alpha} K_{5/3} \left( \frac{2mc\omega}{3\gamma^2 eB \sin \alpha} \right).$$

Inserting this into equ. (48) and equ. (47) leads to a sum of 3 single integrals instead of a double integral, which makes it easier to calculate it numerically. The resulting expression is

$$\frac{dE}{dt d\omega dV} = \frac{e^2\omega}{\sqrt{3}\pi c} \sum_i A_i \left[ \frac{1}{\gamma_{a,i}} \int_{\frac{C^*}{\gamma_{a,i}^2 \sin \alpha}}^{\infty} K_{5/3}(\xi) d\xi - \frac{1}{\gamma_{b,i}} \int_{\frac{C^*}{\gamma_{b,i}^2 \sin \alpha}}^{\infty} K_{5/3}(\xi) d\xi \right] \quad (49)$$

$$+ \int_{\gamma_{a,i}}^{\gamma_{b,i}} \frac{2C^*}{\gamma^4 \sin \alpha} K_{5/3} \left( \frac{C^*}{\gamma^2 \sin \alpha} \right) d\gamma \quad (50)$$

with  $C^* = \omega 2mc / (3eB)$ .

Aharonian et al. (2010) (AKP10 in the following) found an even more convenient way to calculate  $F(x)$  in the emission spectrum, equ. (39), before integrating over an electron energy distribution and provide an analytical fitting function that does not contain any special functions and is therefore even faster to compute. Additionally they provide an approximation for the spectrum of an isotropic pitch angle distribution  $G(x) = 1/2 \int F(x/\sin \alpha) \sin^2 \alpha d\alpha$ . These are given by

$$\tilde{F}(x) \approx 2.15x^{1/3}(1 + 3.06x)^{1/6} \frac{1 + 0.884x^{2/3} + 0.471x^{4/3}}{1 + 1.64x^{2/3} + 0.974x^{4/3}} e^{-x}, \quad (51)$$

$$\tilde{G}(x) \approx \frac{1.808x^{1/3}}{\sqrt{1 + 3.4x^{2/3}}} \frac{1 + 2.21x^{2/3} + 0.347x^{4/3}}{1 + 1.353x^{2/3} + 0.217x^{4/3}} e^{-x}, \quad (52)$$

and are supposed to provide an accuracy better than 0.2 % over the entire range of  $x$ . Here, the function  $\tilde{F}(x)$  can be directly substituted instead of  $F(x)$  in equ. (39), whereas  $\tilde{G}(x)$  already includes an integration over an isotropic pitch angle distribution.

### 2.1.2 Inverse Compton Emission

When a photon is scattered inelastically by a charged particle, either the particle gains energy from the photon or vice versa, if the charged particle's energy is larger than that of the photon. The latter is called inverse Compton emission and describes the scattering process where a highly relativistic electron transfers some of its energy to a low-energy photon. In a galactic context, these photons that can be

up-scattered are originating from the interstellar radiation field, which consists mainly of infrared (IR) dust emission and ultra violet (UV) and optical stellar emission, as well as the CMB.

Considering an incoming photon with energy  $E = h\nu$  in the rest frame of an electron that gains energy in the scattering process, the energy  $E_1 = h\nu_1$  of the outgoing photon decreases according to

$$E_1 = \frac{E}{1 + \frac{E}{m_e c^2} (1 - \cos \theta)}, \quad (53)$$

where  $\theta$  is the angle between the incoming and the scattered photon's direction of motion. In the so called Thomson limit, where  $h\nu \ll mc^2$ , the scattering is nearly elastic, so that the photon hardly loses any energy in the rest frame of the electron. Thus, the scattering process is described by the classical Thomson scattering, where the cross-section is given by

$$\frac{d\sigma_T}{d\Omega} = \frac{1}{2} r_0^2 (1 + \cos^2 \theta), \quad (54)$$

which leads to a total cross-section of  $\sigma_T = 8/3\pi r_0^2$ , where  $r_0 = e^2/(m_e c^2)$  is the classical electron radius. As the photon energy becomes large, the recoil of the photon can not be neglected anymore and the cross section is reduced. This can be obtained from quantum electrodynamics and is expressed in the differential Klein-Nishina cross-section for unpolarized radiation as

$$\frac{d\sigma_{KN}}{d\Omega} = \frac{r_0^2}{2} \left( \frac{E_1}{E} \right)^2 \left( \frac{E}{E_1} + \frac{E_1}{E} - \sin^2 \theta \right) \quad (55)$$

which reduces again to the Thomson cross-section for  $E_1 = E$ .

To calculate the average energy gain in the case of inverse Compton scattering, where the electron has enough kinetic energy to transfer some of it to the incoming photon, we consider a Lorentz transformation from an observer's rest frame  $K$  to the electron's rest frame  $K'$ , in which the energy of the incoming photon  $E'$  and the out coming photon  $E'_1$  transform as

$$E' = E\gamma(1 - \beta \cos \theta), \quad (56)$$

$$E_1 = E'_1 \gamma (1 + \beta \cos \theta'_1), \quad (57)$$

where  $\theta'_1$  is the scattering angle of the outgoing photon relative to the incident electron, see Fig. (5). Therefore, with  $\theta$  and  $\theta'_1$  being typically of order  $\pi/2$  and in the Thomson limit with  $E'_1 \simeq E'$ , we obtain  $E_1 \simeq \gamma^2 E$ . As the Lorentz factor  $\gamma$  can be very large for highly relativistic electrons, the incoming photon can gain a lot of energy, e.g. for  $\gamma = 1000$ , a far-infrared (FIR) photon can be up-scattered into the X-ray regime. But still, the condition for Thomson scattering in the rest frame  $\gamma E \ll mc^2$  has to be fulfilled. Otherwise, the probability of the process is reduced and  $E'_1 < E$ , which makes the scattering process less effective.

To obtain the total emitted power by Compton scattering off a single electron, we have to integrate the spectral emissivity over the incident photon energy distribution  $n(E)$  to get

$$P_{\text{Comp}} = \frac{4}{3} \sigma_T c \beta^2 \gamma^2 u_{\text{ph}} \quad (58)$$

where the total energy density of photons is  $u_{\text{ph}} = \int E n(E) dE$ , that yields the total number of incident photons per unit time  $c\sigma_T u_{\text{ph}} / \langle E \rangle$  with the average incident photon energy  $\langle E \rangle$ , such that for  $\beta \simeq 1$  the mean energy of scattered photons is given by  $\langle E_1 \rangle = 4/3 \gamma^2 E$ . Comparing this with equ. (14), it is striking that  $P_{\text{sync}}/P_{\text{Comp}} = u_B/u_{\text{ph}}$ , from where it becomes clear that synchrotron emission can also be interpreted as scattering of electrons off virtual photons of the magnetic field.

The spectrum of the emission from inverse Compton scattering can be obtained by starting with a physical assumption concerning the involved angles, see Jones (1968) and Blumenthal and Gould (1970) for the following discussion. We consider a Lorentz transformation from the lab frame  $K$  to the electron

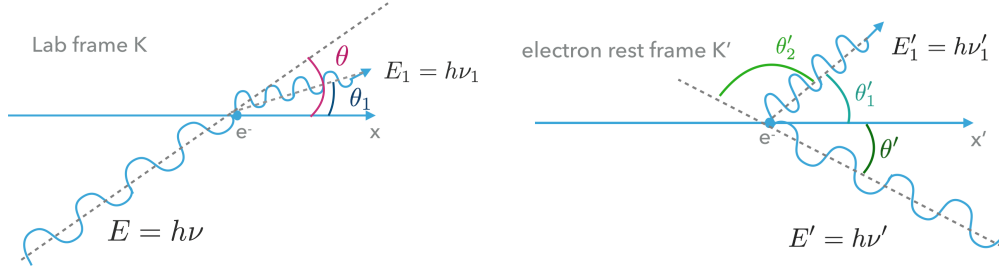


Figure 5: Inverse Compton emission as seen from the lab frame  $K$  (left panel) and the rest frame of the electron  $K'$  (right panel).

rest frame  $K'$  (see Fig. 5) to obtain the relation between the angle of the incoming photon as seen from the two different frames:

$$\tan \theta' = \frac{\sin \theta}{\gamma(\cos \theta - \beta)} \rightarrow -\frac{1}{\gamma} \cot\left(\frac{\theta}{2}\right), \quad (59)$$

where  $\gamma$  and  $\beta c = v$  are the Lorentz factor and the velocity of the electron in the lab frame, respectively. The last step is valid in the highly relativistic case, where  $\beta \rightarrow 1$ . From this it becomes clear that an in the lab frame isotropic radiation field is incident on the electron in its rest frame in a very narrow cone in the direction of the negative  $x'$  axis. Thus, in the following it is assumed that  $\theta' \rightarrow 0$ . From this, one can easily verify the order-of-magnitude estimate from above to get the maximum energy of a scattered photon. Inserting  $\beta \approx 1 - 1/2\gamma^{-2}$  into equ. (56) it follows directly that the photon energy in  $K'$  varies from  $E'_{\min} \approx E/2\gamma$  for  $\theta = 0$  to  $E'_{\max} \approx 2\gamma E$  for  $\theta = \pi$ . For the scattered photon we have from equ. (57) that  $E_{1,\max} \approx 2\gamma E'_1$  for  $\theta'_1 = 0$ . Hence, the case of Thomson scattering with  $E'_1 = E'$  we get the maximum energy for the scattered photon in a head-on collision of electron and photon

$$E_{1,\max} \approx 2\gamma E'_1 \approx 4\gamma^2 E. \quad (60)$$

In order to get the spectrum from inverse Compton scattering, we now consider the incoming photon field in the rest frame of the electron, from which we derive the scattered radiation field. First, the differential photon density in the lab frame is for an isotropic distribution given by  $dn = 1/2n(E)dE dx$  with  $x \equiv \cos \theta$ . Using the Lorentz invariance of  $dn/E$  and  $|dE'/dx| = \gamma\beta E \rightarrow \gamma E$  we obtain

$$dn'(E'; E) = n(E) \frac{E'}{2E^2\gamma} dE \quad (61)$$

for  $E/2\gamma < E' < 2\gamma E$  and 0 otherwise. The distribution of the scattered photons in  $K'$  is

$$\frac{dN_{\gamma,E}}{dt'dE'd\Omega'_1 dE'_1} = dn'(E'; E) c \frac{d\sigma}{d\Omega'_1 dE'_1}, \quad (62)$$

which yields the energy distribution of scattered photons in the lab frame,

$$\frac{dN_{\gamma,E}}{dt dE_1} = \iint_{(E', \Omega'_1)} \frac{dN_{\gamma,E}}{dt' dE' d\Omega'_1 dE'_1} \frac{dt' dE' d\Omega'_1 dE'_1}{dE_1}, \quad (63)$$

where the indices  $\gamma$  and  $E$  imply that this still has to be integrated over the electron and initial photon spectra to get the total emitted spectrum. But first, we have to decide in which case we are interested in - the Thomson limit, or the general case, which is described by the Klein-Nishina formalism.

In the Thomson limit, we have from equ. (54) that

$$\frac{d\sigma}{d\Omega'_1 dE'_1} \rightarrow \frac{1}{2} r_0^2 (1 + \cos^2 \theta'_1) \delta(E'_1 - E'). \quad (64)$$

After inserting this expression together with equ. (61) into equ. (62) and (63), it is convenient to use the substitution  $\eta'_1 = 1 - \beta \cos \theta'_2 \approx 1 - \cos \theta'_2$  since from equ. (57) we have  $E_1 = \gamma E'_1 [1 + \beta \cos(\pi - \theta'_2)] \approx \gamma E'_1 (1 - \cos \theta'_2) \approx \gamma E'_1 \eta'_1$ . This enables us to use  $dE'_1/dE_1 = 1/(\gamma \eta'_1)$  together with  $dt'/dt = 1/\gamma$  as well as  $d\Omega'_1 = 2\pi d\eta'_1$  to finally get the result

$$\frac{dN_{\gamma,E}}{dt dE_1} = \frac{2\pi r_0^2 c}{\gamma^2 E} f\left(\frac{E_1}{4E\gamma^2}\right) n(E) dE \quad (65)$$

with

$$f(x) = 2x \ln x + x + 1 - 2x^2. \quad (66)$$

I.e. the total number of photons of energy  $E_1$  produced per unit range of  $E_1$  per unit time that scatter off of an electron with energy  $\gamma mc^2$ . The function  $f(x)$  from Blumenthal and Gould (1970) decreases from  $f(0) = 1$  to  $f(1) = 0$ , as  $x = 1$  gives the maximum photon energy that can be produced in the scattering ( $E_1 \leq 4E\gamma^2$ ). As already mentioned before, equ. (65) now has to be integrated over the electron energy distribution, where the integration limits are  $\gamma_{\min} = \max[1/2(E_1/E)^{1/2}, \gamma_1]$  and  $\gamma_{\max} = \min[\gamma_2, 1/2(E_1/E)^{1/2}]$  which results from kinematic considerations and  $\gamma_{1/2}$  are the ends of the electron distribution. By assuming  $\gamma_1 \ll 1/2(E_1/E) \ll \gamma_2$ , the integration can be done from 0 to  $\infty$ .

For a power-law distribution of electrons, we obtain

$$\frac{dE}{dt dE_1 dV} = C_e \pi r_0^2 c 2^{a+3} \frac{a^2 + 4a + 11}{(a+3)^2(a+5)(a+1)} E_1^{-\frac{a-1}{2}} \int_0^\infty E^{(a-1)/2} n(E) dE. \quad (67)$$

Assuming that the incident radiation field can be approximated by a sum of black body distributions with weights  $f_i$  and temperatures  $T_i$

$$n(E) = \sum_i f_i \frac{E^2}{\pi^2 (\hbar c)^3 (\exp(E/k_B T_i) - 1)}, \quad (68)$$

the integral in equ. (67) can be evaluated in terms of the gamma function  $\Gamma$  and the Riemann Zeta function,  $\zeta$ , such that the result is the following:

$$\frac{dE}{dt d\nu_1 dV} = \frac{8\pi^2 r_0^2 C_e}{h^2 c^2} 2^{a+3} \frac{a^2 + 4a + 11}{(a+3)^2(a+5)(a+1)} \Gamma\left(\frac{a+5}{2}\right) \zeta\left(\frac{a+5}{2}\right) (h\nu_1)^{-\frac{a-1}{2}} \left[ \sum_i f_i (k_B T_i)^{\frac{a+5}{2}} \right]$$

where  $i$  denotes the CMB, IR or stellar radiation field. For the CMB, we have  $k_B T_{\text{CMB}} \approx 2.35 \times 10^{-4}$  eV. For the interstellar radiation field or IR dust emission, it is common practice to provide the corresponding photon energy density and the black-body temperature of the radiation spectrum. They are connected with the dilution factor  $f_i$  by the relation

$$u_{\text{ph}} = f_i a_{\text{rad}} T^4 \quad (69)$$

where the radiation constant  $a_{\text{rad}} = 4\sigma/c = 8\pi^5 k_B^4 / (15h^3 c^3) \approx 7.57 \times 10^{-15}$  erg cm<sup>-3</sup> K<sup>-4</sup>.

For arbitrary  $E' \approx \gamma E > mc^2$ , the Klein-Nishina cross-section has to be used instead of equ. (64). In terms of the variables used here, it reads

$$\frac{d\sigma}{d\Omega_1 dE'_1} = \frac{1}{2} r_0^2 \left(\frac{E'_1}{E'}\right)^2 \left(\frac{E'}{E'_1} + \frac{E'_1}{E'} - \sin \theta'_2\right) \delta\left(E'_1 - \frac{E'}{1 + \frac{E'}{m_e c^2} (1 - \cos \theta'_2)}\right) \quad (70)$$

and has to be inserted into equ. (62) and (63). The resulting scattered photon spectrum per electron, first obtained by Jones (1968), is given by

$$\frac{dN_{\gamma,E}}{dt dE_1} = 2\pi r_0^2 c \gamma^{-2} n(E) \frac{dE}{E} \left[ 2q \ln q + (1+2q)(1-q) + \frac{1}{2} \frac{(\Gamma_e q)^2}{1 + \Gamma_e q} (1-q) \right], \quad (71)$$

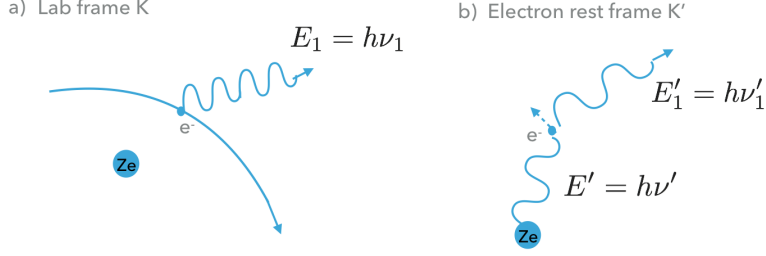


Figure 6: Graphical illustration of bremsstrahlung emission as seen from the lab frame  $K$  (left) and the electron rest frame  $K'$  (right).

where  $\Gamma_e = 4E\gamma/(m_e c^2)$ ,  $q = E_1^*/(\Gamma_e(1 - E_1^*))$  and  $E_1^* = E_1/(\gamma m_e c^2)$ . Here,  $\Gamma_e \ll 1$  would again lead to the result in the Thomson limit (see equ. 65), but now the formula can be used in any case and is only based on the assumption of highly relativistic electrons with  $\gamma \gg 1$ . Equ. (71) has to be again integrated over the radiation distribution at hand, i.e., equ. (68), as well as the electron energy distribution. Thus, we obtain for the total emission spectrum

$$\frac{dE_1}{dt d\nu_1} = 2\pi h E_1 r_0^2 c \int d\gamma \frac{N(\gamma)}{\gamma^2} \int \frac{dE}{E} n(E) f(q(E)). \quad (72)$$

After changing the variable of integration  $\gamma \rightarrow q(\gamma) = E_1^* m_e c^2 / (4E\gamma(1 - E_1^*))$ , this leads to

$$\frac{dE_1}{dt d\nu_1} = 2\pi h E_1 r_0^2 c \int d\gamma \frac{N(\gamma)}{\gamma^2} \int_{q_{\min}}^1 \frac{dq}{q} n(q) f(q) \quad (73)$$

The integration limits for  $q$  follow from the kinematic limitations for  $E_1^*$ , i.e.  $E/\gamma m_e c^2 \leq E_1^* \leq \Gamma_e/(1 + \Gamma_e)$ , such that  $q_{\min} = [4\gamma^2(1 - E/(\gamma m_e c^2))]^{-1} \leq q \leq 1$ . For a binned energy distribution of electrons, we get

$$\frac{dE_1}{dt d\nu_1} = 2\pi h E_1 r_0^2 c \sum_i A_i \int_{\gamma_{a,i}}^{\gamma_{b,i}} d\gamma \frac{1}{\gamma^2} \int_{q_{\min}}^1 \frac{dq}{q} f(q) \quad (74)$$

For a given black-body distribution, the second integral over  $q$  can be pre-evaluated for a certain range of  $\gamma$ -values. This speeds up the numerical integration over the binned electron energy distribution.

### 2.1.3 Relativistic Bremsstrahlung

A third process that occurs when an electron gets accelerated in the field of a nucleus is called bremsstrahlung or free-free-emission, since it can be seen as the transition between two unbound states. Even though a detailed discussion of the resulting radiation would require quantum electrodynamics, we can gain useful insights and derive the same functional behaviors for relativistic bremsstrahlung by the classical method of virtual quanta, which is also called the Weizsäcker-Williams method. In this approach, we consider a relativistic electron moving towards an ion with charge  $Ze$  that moves much slower in comparison. In the rest frame of the electron, which is located on the  $y$ -axis with a distance  $b$  to the origin, the ion moves towards the electron along the  $x$ -axis with velocity  $v$ . The electrostatic field of the ion appears to be a pulse of electromagnetic radiation to the electron, which can scatter off of it and thus emit radiation. Hence in this picture, the resulting bremsstrahlung emission after transforming back to the lab frame (or the rest frame of the ion) can be interpreted as Compton emission from the scattering of the virtual quanta from the ion's electrostatic field in the frame of the electron.

The process of bremsstrahlung emission is sketched in Fig. 6 as seen in the lab frame  $K$  (left) and in the electron rest frame  $K'$  (right). The basic relation in the Weizsäcker-Williams approach is thus given by

$$d\sigma_a = d\sigma_b dN, \quad (75)$$

where the indices a and b relate to the panels in Fig. 6. An expression for the differential number of incident photons  $dN$  can be found by considering the electromagnetic field of a uniformly moving charge, see e.g., Rybicki and Lightman (1986). In the case of a highly relativistic charge that moves with velocity  $v$ , Lorentz-factor  $\gamma$  and charge  $q$  in the direction of the  $x$ -axis with a distance of  $b$ , the electromagnetic field components are given by

$$\begin{aligned} E_x &= -\frac{qv\gamma t}{(\gamma^2 v^2 t^2 + b^2)^{3/2}} \\ E_y &= \frac{q\gamma b}{(\gamma^2 v^2 t^2 + b^2)^{3/2}} \\ E_z &= B_x = B_y = 0 \\ B_z &= \beta E_y. \end{aligned} \quad (76)$$

It can be shown, that the maximum of  $E_y^{\max} = q\gamma/b^2$  whereas  $E_x^{\max} \sim q/b^2$  which is the case when  $t \sim b/\gamma v$ . This means that the field appears to be a pulse of radiation that is concentrated in the plane transverse to its motion. The spectrum of this pulse of virtual quanta can be obtained by a Fourier transformation

$$\hat{E}(\omega) = \frac{q\gamma b}{2\pi} \int_{-\infty}^{\infty} (\gamma^2 v^2 t^2 + b^2)^{3/2} e^{i\omega t} dt. \quad (77)$$

Solving this integral in terms of the modified Bessel function of order one gives the result

$$\hat{E}(\omega) = \frac{q}{\pi v b} \frac{b\omega}{\gamma v} K_1\left(\frac{b\omega}{\gamma v}\right). \quad (78)$$

Thus the spectrum from the highly relativistic moving ion with charge  $q = Ze$  as seen from the electrons rest frame  $K'$  is given by

$$\frac{dW'}{dA'd\omega'} = c \left| \hat{E}(\omega) \right|^2 = \frac{(Ze)^2 c}{\pi^2 b'^2 v^2} \left( \frac{b'\omega'}{\gamma v} \right)^2 K_1^2\left(\frac{b'\omega'}{\gamma v}\right). \quad (79)$$

These virtual quanta are now scattered according to the corresponding cross-section, which is in the low frequency limit  $\hbar\omega \lesssim mc^2$  the Thomson cross-section, but for higher frequencies the Klein-Nishina cross-section. In the Thomson limit, the scattered radiation is thus

$$\frac{dW'}{d\omega'} = \sigma_T \frac{dW'}{dA'd\omega'}. \quad (80)$$

The Lorentz transformation back to the lab system yields

$$\frac{dW}{d\omega} = \frac{8Z^2 e^6}{3\pi b^2 m_e^2 c^3 v^2} \left( \frac{b\omega}{\gamma^2 v} \right)^2 K_1^2\left(\frac{b\omega}{\gamma v}\right) \quad (81)$$

First, the integration over the impact parameter results in the emitted power of a single electron per unit frequency, that in turn needs to be integrated over the distribution of electrons to obtain the resulting radiation spectrum

$$\frac{dW}{dt dV d\omega} = \int_{p_{min}}^{p_{max}} \left( \int_{b_{min}}^{\infty} 2\pi c n_i \frac{dE}{d\omega} b db \right) n(p) dp. \quad (82)$$

Following Zeković et al. (2013), they use a power-law distribution in momentum,  $n(p)dp = k_e p^{-a} dp$ , where the momentum is not normalized to  $m_e c$ . Therefore, we have to take into account that  $k_e =$

$C_e(mc)^{a-1}$ , where  $C_e$  is the normalization for a power-law distribution as we defined it in equ. (7). Hence, we obtain the expression

$$\frac{dW}{dt d\omega dV} = \frac{16Z^2 e^6}{3m^2 c^4} n_i k_e (m\hbar\omega)^{-\frac{a-1}{2}} \int_{x_{\min}}^{x_{\max}} \frac{1}{2} x^{\frac{a-3}{2}} \sqrt{1 + \frac{mc^2}{\hbar\omega}} x G(x) dx \quad (83)$$

$$G(x) = \int_x^{\infty} y K_1(y) dy = x K_0(x) K_1(x) - \frac{1}{2} x^2 (K_1^2(x) - K_2^2(x)) \quad (84)$$

where  $x = \omega b_{\min}/(\gamma^2 v) = \omega \hbar m/p^2$  and  $x_{\min/\max} = m\hbar\omega/p_{\max/\min}^2$ . For a binned electron spectrum, which is given by a constant value  $A_i$  in each interval  $[p_{i,a}, p_{i,b}]$ , this yields

$$\frac{dW}{dt d\omega dV} = \frac{16Z^2 e^6}{3m^2 c^4} (mc)^{-1} n_i \sum_i A_i \int_{p_{\min,i}}^{p_{\max,i}} \sqrt{1 + \frac{m^2 c^2}{p^2}} G(x(p)) dp. \quad (85)$$

The lower and upper limits of the integrals are  $p_{\max,i} = \min(p_{\min}, p_{i,b})$  and  $p_{\min,i} = \max(p_{\max}, p_{i,a})$ .

For deriving the corresponding expression in the general case including the Klein-Nishina regime, one can again use the scattering picture in the right panel of Fig. 5 and the corresponding kinematic and transformation relations

$$E_1 = E'_1 \gamma (1 - \cos \theta'_2), \quad (86)$$

$$E'_1 = \frac{E'}{1 + \frac{E'}{m_e c^2} (1 - \cos \theta'_2)}, \quad (87)$$

which can be combined to obtain

$$E' = \frac{E'_1}{1 - \frac{E'_1}{m_e c^2} (1 - \cos \theta'_2)} = \frac{E'_1}{1 - \frac{E_1}{\gamma m_e c^2}} = \frac{E_1}{\gamma (1 - \cos \theta'_2) (1 - \frac{E_1}{\gamma m_e c^2})} \quad (88)$$

From this one can read off the minimum and maximum values for the photon energy in the electron rest frame before scattering  $E'$  for a fixed  $E_1$  that is achieved in the lab frame after scattering,

$$E'_{\min} = E_1/2\gamma(1 - \frac{E_1}{\gamma m_e c^2}) \quad (89)$$

and

$$E'_{\max} = E'_{1\max} \sim \gamma m_e c^2, \quad (90)$$

where the latter derives from the estimate of  $\omega'_{\max} \sim \gamma c/b_{\min}$  and the minimum impact parameter  $b_{\min} \sim \hbar/m_e c$  that can be understood in terms of the uncertainty principle. Transforming the differential solid angle in the Klein-Nishina cross section formula (70) according to  $d\Omega'_1 = 2\pi d(1 - \cos \theta'_2) = 2\pi [E'\gamma(1 - E_1/\gamma m_e c^2)]^{-1} dE_1$  allows to write it as a function of  $E_1$  and  $E'$

$$\frac{d\sigma}{dE' dE_1} = \pi r_0^2 \frac{1}{\gamma E'} \left[ 1 - \frac{E_1}{\gamma m_e c^2} + \frac{1}{1 - \frac{E_1}{\gamma m_e c^2}} - \frac{2}{E'} \frac{E_1/\gamma}{1 - \frac{E_1}{\gamma m_e c^2}} + \frac{1}{E'^2} \left( \frac{E_1/\gamma}{1 - \frac{E_1}{\gamma m_e c^2}} \right)^2 \right]. \quad (91)$$

For comparison with the often used Bethe-Heitler cross section it is constructive to use a limiting approximation for the modified Bessel function of first order in equ. (78), which is  $K_1(x) \rightarrow 1/x$  for  $x \ll 1$ , that means  $b \ll \gamma v/\omega$ . From that we get the differential number of incident photons

$$dN = \frac{c}{\hbar\omega'} \left| \hat{E}(\omega') \right|^2 dA' d\omega' = \frac{c}{\hbar\omega'} \frac{q^2}{\pi^2 b'^2 c^2} 2\pi b' db' d\omega'. \quad (92)$$

For  $q = Ze$  and the fine structure constant  $\alpha = e^2/\hbar c$  this becomes with  $d\omega'/\omega = dE'/E'$

$$dN = \frac{2\alpha Z^2}{\pi} \frac{db'}{b'} \frac{dE'}{E'}. \quad (93)$$

Combining this together with equ. (91) and (75) and then integrating over  $E'$  and  $b'$  results in

$$\frac{d\sigma}{dE_1} = 4\alpha r_0^2 Z^2 \frac{1}{E_1} \left[ \frac{4}{3} \left( 1 - \frac{E_1}{\gamma m_e c^2} \right) + \left( \frac{E_1}{\gamma m_e c^2} \right)^2 \right] \int \frac{db'}{b'} \quad (94)$$

following Blumenthal and Gould (1970). The integration limits for  $b'$  are  $b'_{\min} \sim \hbar/m_e c$  and  $b'_{\max} \sim \gamma c/\omega'_{\min} = \hbar\gamma c/E'_{\min}$ , where  $E'_{\min}$  is given in equ. (89). Therefore, the integration over  $b'$  gives

$$\int_{\hbar/m_e c}^{\hbar\gamma c/E'_{\min}} \frac{db'}{b'} = \ln \left( \frac{\gamma m_e c^2}{E'_{\min}} \right) = \ln \left[ \frac{2\gamma^2 m_e c^2 (1 - \frac{E_1}{\gamma m_e c^2})}{E_1} \right]. \quad (95)$$

By identifying  $E_1 = \hbar\omega$ , the initial energy of the electron  $E_i = \gamma m_e c^2$  and the final energy of the electron after scattering  $E_f = E_i - \hbar\omega$ , it can be rewritten as

$$d\sigma = 4\alpha r_0^2 Z^2 \frac{d\omega}{\omega} \left( \frac{4}{3} \left( 1 - \frac{\hbar\omega}{E_i} \right) + \left( \frac{\hbar\omega}{E_i} \right)^2 \right) \ln \left( \frac{2E_i E_f}{m_e c^2 \hbar\omega} \right). \quad (96)$$

This can now be compared to the cross section derived by Bethe and Heitler (1934) in the Born approximation for non-screened (fully ionized) ions and for the extreme relativistic case

$$d\sigma = 4\alpha r_0^2 Z^2 \frac{d\omega}{\omega} \frac{1}{E_i^2} \left( E_i^2 + E_f^2 - \frac{2}{3} E_i E_f \right) \left( \ln \frac{2E_i E_f}{m_e c^2 \hbar\omega} - \frac{1}{2} \right). \quad (97)$$

This is essentially the same as equ. (96), since the argument of the logarithm is  $\gg 1$ . As pointed out by Haug (1997), if we consider mildly and highly relativistic electrons, we can combine the non-relativistic cross section obtained by Heitler (1954) with the extreme relativistic case that is expanded up to orders  $p_{i,f}^6$ . This yields the result

$$\begin{aligned} d\sigma = & \frac{2\alpha Z^2 r_0^2}{k p_i^2} \left\{ \frac{4}{3} \epsilon_i \epsilon_f + k^2 - \frac{7}{15} \frac{k^2}{\epsilon_i \epsilon_f} - \frac{11}{70} \frac{k^2 (p_i^2 + p_f^2)}{(\epsilon_i \epsilon_f)^4} \right\} \\ & \times \left\{ 2 \ln \frac{\epsilon_i \epsilon_f + p_i p_f - 1}{k} - \frac{p_i p_f}{\epsilon_i \epsilon_f} \times \right. \\ & \left. \times \left[ 1 + \frac{1}{\epsilon_i \epsilon_f} + \frac{7}{20} \frac{p_i^2 + p_f^2}{(\epsilon_i \epsilon_f)^3} + \left( \frac{9}{28} k^2 + \frac{263}{210} p_i^2 p_f^2 \right) \frac{1}{(\epsilon_i \epsilon_f)^3} \right] \right\}. \quad (98) \end{aligned}$$

Here,  $\epsilon_{i,f} = E_{i,f}/m_e c^2$ ,  $k = h\nu/m_e c^2$  and  $p_{i,f}$  is in units of  $m_e c$ . As this formula is given in the Born approximation, where the distortion of the electron's wave function near the Coulomb field of the nucleus is neglected, an additional factor was introduced by Elwert (1939) to account for this effect:

$$f_E = \frac{a_f}{a_i} \frac{1 - \exp(-2\pi a_i)}{1 - \exp(-2\pi a_f)} \quad (99)$$

where  $a_{i,f} = \alpha Z \epsilon_{i,f} / p_{i,f}$ .

In addition to electron-ion bremsstrahlung, we also have to take into account electron-electron bremsstrahlung. While at low incident electron energies the quadrupole emission from the electron-electron interaction can be neglected in comparison to the electron-nucleus dipole emission, it can make a significant contribution for higher energetic electrons and emitted photons, e.g. the relative contribution from e-e-bremsstrahlung to e-p-bremsstrahlung emission is  $\sim 25\%$  at photon energies around 400 keV (Haug 1975a).

The exact expression for the e-e-bremsstrahlung cross section was first derived by Haug (1975b), which is quite long and numerically difficult to use, but Baier et al. (1967) derived a good approximation for ultra-relativistic electrons, that is given in terms of  $\epsilon_1 = E_1/(m_e c^2)$  by

$$d\sigma_{ee} = (\sigma_1 + \sigma_2)A(\epsilon_1, \gamma)d\epsilon_1 \quad (100)$$

$$\sigma_1 = \frac{4r_0^2\alpha}{\epsilon_1} \left[ \frac{4}{3} \left(1 - \frac{\epsilon_1}{\gamma}\right) + \left(\frac{\epsilon_1}{\gamma}\right) \right] \left[ \ln \frac{2\gamma(\gamma - \epsilon_1)}{\epsilon_1} - \frac{1}{2} \right] \quad (101)$$

$$\sigma_2 = \frac{r_0^2\alpha}{3\epsilon_1} \begin{cases} 16(1 - \epsilon_1 + \epsilon_1^2) \ln \frac{\gamma}{\epsilon_1} - \frac{1}{\epsilon_1^2} + \frac{3}{\epsilon_1} - 4 + 4\epsilon_1 - 8\epsilon_1^2, & \epsilon_1 \leq \frac{1}{2} \\ -2(1 - 2\epsilon_1) \ln(1 - 2\epsilon_1) \left( \frac{1}{4\epsilon_1^3} - \frac{1}{2\epsilon_1^2} + \frac{3}{\epsilon_1} - 2 + 4\epsilon_1 \right), & \\ \frac{2}{\epsilon_1} \left[ \left(4 - \frac{1}{\epsilon_1} + \frac{1}{4\epsilon_1^2}\right) \ln 2\gamma - 2 + \frac{2}{\epsilon_1} - \frac{5}{8\epsilon_1^2} \right], & \epsilon_1 > \frac{1}{2}. \end{cases} \quad (102)$$

The factor  $A(\epsilon_1, \gamma)$  is a mildly-relativistic correction factor that was introduced by Baring et al. (1999) to be

$$A(\epsilon_1, \gamma) = 1 - \frac{8}{3} \frac{(\gamma - 1)^{1/5}}{\gamma + 1} \left( \frac{\epsilon_1}{\gamma} \right)^{1/3}.$$

According to them, the highly relativistic approximation combined with this factor yields an accuracy within 10% compared to the exact expression by Haug (1975b).

#### 2.1.4 Overview and Cross-Check

In order to get an overview of all the different non-thermal leptonic emission processes, we use a simple power law distribution of electrons to calculate the resulting radiation spectrum. At the same time, we compare the approach of a binned momentum spectrum to a continuous power-law distribution of electrons. The spectrum is chosen to range from  $p_e = 1$  to  $p_e = 10^6$  with a power law index  $a_e = 2.1$ . Furthermore, we adopt  $B = 100 \mu\text{G}$  and  $n_H = 1\text{cm}^{-3}$ . In Fig. 7 we show the resulting synchrotron (red), bremsstrahlung (blue) and IC emission (green) for a continuous power-law distribution (PL) in comparison to a binned spectrum. The IC emission is shown for IC scattering off of different photon fields, i.e., the CMB and two different dust components with black-body temperatures of  $T = 100\text{K}$  and  $T = 20\text{K}$ , with suitable dilution factors to obtain an energy density of  $\sim 1\text{eV cm}^{-3}$ , respectively. Since for the analytical derivation of the emissivity of synchrotron and IC emission the electron spectrum is assumed without a cut-off in momentum, it also does not show a cut-off in emission, in contrast to my approach of a binned spectrum including a cut-off. Using the extreme relativistic approximation for the bremsstrahlung cross section (equ. 97) seems to be in good agreement with the exact description by Haug (1997), hence we will adopt it in the following. Also the analytical approximation from equ. (51) and (52) by Aharonian, Kelner and Prosekin (2010) (AKP10) fits in both cases of an isotropic distribution of pitch angles and a fixed angle of  $\alpha = \pi/2$  the exact formalism.

## 2.2 Hadronic Interactions

The collision of CR protons with protons and other nuclei in the ambient interstellar medium lead to the production of several secondary particles that are being discussed in the following. These interactions constitute another source of non-thermal emission. In particular, inelastic proton-proton-collisions produce mainly pions, that lead to the production of secondary electrons or gamma-rays, depending on the charge of the pions:

$$p + p \longrightarrow \pi^\pm + X$$

$$p + p \longrightarrow \pi^0 + X$$

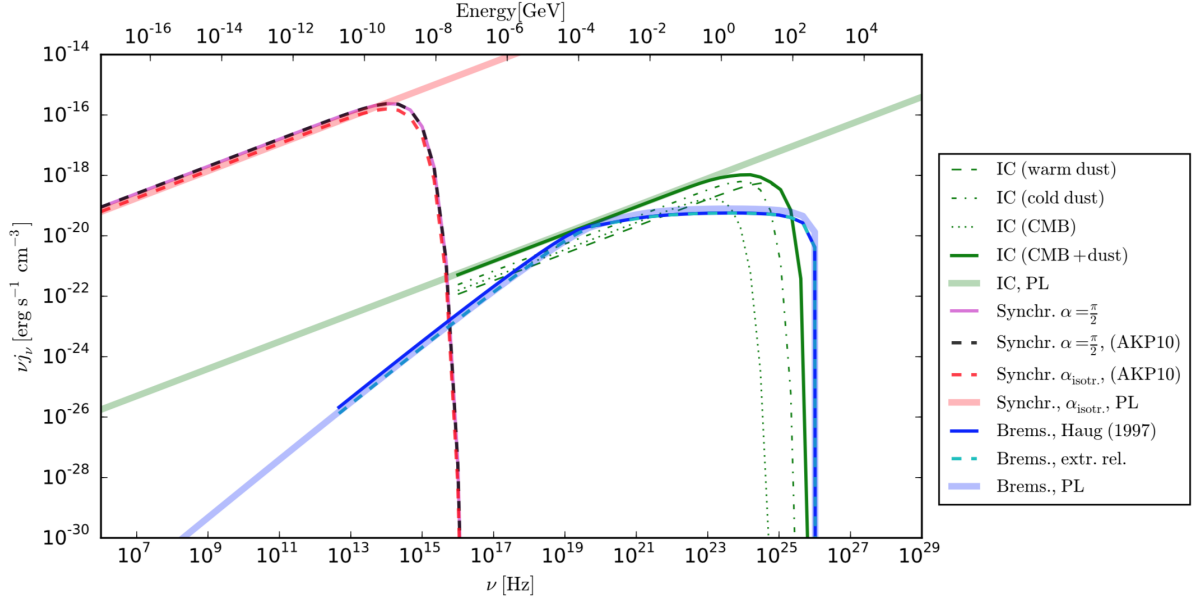


Figure 7: All leptonic radiation processes calculated with a binned electron spectrum compared to a continuous power law distribution (PL).

$$\pi^0 \longrightarrow 2\gamma$$

$$\pi^+ \longrightarrow \mu^+ + \nu_\mu$$

$$\pi^- \longrightarrow \mu^- + \bar{\nu}_\mu$$

The muons decay further into secondary electrons, that contribute to the leptonic radiation processes from primary electrons discussed above.

$$\mu^+ \longrightarrow e^+ + \nu_e + \bar{\nu}_\mu$$

$$\mu^- \longrightarrow e^- + \bar{\nu}_e + \nu_\mu$$

Another channel of secondary particle production is the process

$$p + p \longrightarrow K^\pm + X$$

$$K^+ \longrightarrow \mu^+ + \nu_\mu$$

$$K^- \longrightarrow \mu^- + \bar{\nu}_\mu$$

$$K^\pm \longrightarrow \pi^0 + \pi^\pm$$

This is another source of charged and neutral pions and therefore of gamma-rays and secondary electrons, that lead to leptonic radiation processes. The relative contribution of the two channels  $p + p \longrightarrow \pi^\pm + X$  and  $p + p \longrightarrow K^\pm + X$  depends on the proton energy and the Kaon-channel contribution reaches

from 8% at about 100 GeV to 19% at 1 TeV before it approaches a value of 27% for higher energies (Gaisser 1990).

Before the resulting production spectra of all relevant secondary particles are discussed, a few definitions are introduced in order to overview the different notations used in the literature, similarly to the formalism used in Moskalenko and Strong (1998).

The production spectrum  $dN_s/(dE_s dt dV)$ , or source function, of a secondary particle species  $s = \gamma, e^-, e^+$  that results from the decay of a pion (with the right charge) that has been produced in a proton-proton collision is given by

$$q_s(E_s) = cn_H \int_{E_p^{\min}}^{\infty} dE_p J_p(E_p) \int_{E_\pi^{\min}}^{E_\pi^{\max}} dE_\pi \frac{d\sigma(E_p, E_\pi)}{dE_\pi} f_{s,\pi}(E_s, E_\pi) \quad (103)$$

where  $J_p(E_p)$  is the energy distribution of incoming CR protons in units of  $\text{erg}^{-1} \text{cm}^{-3}$  and is connected to the often used notation of  $N_p(E_p)$  in units of  $\text{cm}^{-3}$  by

$$J_p(E_p) = N_p(\gamma_p) \frac{d\gamma_p}{dE_p} = N_p(\gamma_p)/m_p c^2. \quad (104)$$

We have to be careful about the definition of  $J_p(E_p)$  being used in the literature, since it sometimes refers to the proton energy flux per steradian  $c/(4\pi)J_p(E_p)$ , but in that case, the formulas for the corresponding source function include another factor of  $4\pi$  to account for the integration over solid angle and the speed of light  $c$  is omitted. The normalized energy distribution  $f_{s,\pi}(E_s, E_\pi)$  gives the probability of the production of a secondary particle  $s$  from a single pion energy  $E_\pi$ . Furthermore, the differential cross section for the production of a pion with energy  $E_\pi$  from the collision of a proton with energy  $E_p$  is denoted by  $d\sigma(E_p, E_\pi)/dE_\pi$  and can be parametrized in different ways as will be discussed in the following paragraphs. Also the limits of the integrals in equ. (103) will be analyzed later on.

In the literature, there are different parameterizations for the corresponding parts of equ. (103). In particular, a production spectrum of pions from a given proton distribution is often calculated first, before the integration over the pion energy is being performed. This so called pion source function is denoted by  $q_\pi$  or  $F_\pi$  and is given by

$$q_\pi(E_\pi) = F_\pi(E_\pi) = cn_H \int_{E_p^{\min}}^{\infty} dE_p J_p(E_p) \frac{d\sigma(E_p, E_\pi)}{dE_\pi}, \quad (105)$$

such that

$$q_s = \int_{E_\pi^{\min}}^{E_\pi^{\max}} dE_\pi q_\pi(E_\pi) f_\pi(E_s, E_\pi). \quad (106)$$

Another frequently used notation is to denote the second integral in equ. (103) as

$$\frac{d\sigma_s(E_s, E_p)}{dE_s} = \int_{E_\pi^{\min}}^{E_\pi^{\max}} dE_\pi \frac{d\sigma(E_p, E_\pi)}{dE_\pi} f_{s,\pi}(E_s, E_\pi) \quad (107)$$

which gives for the source function of the produced secondary particle

$$q_s(E_s) = cn_H \int_{E_p^{\min}}^{\infty} dE_p J_p(E_p) \frac{d\sigma_s(E_s, E_p)}{dE_s}. \quad (108)$$

### 2.2.1 Gamma-ray Emission from Neutral Pion Decay

As already mentioned above, another source of non-thermal emission from CRs is the interaction of CR protons with particles of the ambient ISM, where the creation of a neutral pion leads to the production of two gamma-ray photons. Since only neutral pions are involved in this channel (and no charged ones), the subscript 0 is being dropped and  $\pi$  represents only neutral pions in this section. Following Stecker (1971), Dermer (1986a) and Moskalenko and Strong (1998), the production spectrum of neutral pions produced from hadronic collisions is given by

$$q_\pi(T_\pi) = cn_H \int_{T_p^{\min}(E_\pi)}^{\infty} dT_p J_p(T_p) \frac{d\sigma(T_\pi, T_p)}{dT_\pi}. \quad (109)$$

To find the proton's threshold energy for pion production, the relativistic kinematics of the proton-proton-collision has to be considered. In the center-of-momentum system (CMS, the corresponding quantities are denoted with a prime), the energy of the proton has to be large enough to create the rest mass of the outgoing pion in the lab system (LS), that is

$$2\gamma'_p m_p c^2 = 2m_p c^2 + m_\pi c^2. \quad (110)$$

Rearranging this expression yields the threshold energy

$$\gamma'_p m_p c^2 = m_p c^2 \left( 1 + \frac{m_\pi}{2m_p} \right). \quad (111)$$

This needs to be transformed into the lab frame, where one of the protons is at rest, by performing a Lorentz-transformation

$$\begin{pmatrix} \gamma_p \\ \beta_p \gamma_p \end{pmatrix} = \begin{pmatrix} \gamma'_p & \beta'_p \gamma'_p \\ \beta'_p \gamma'_p & \gamma'_p \end{pmatrix} \begin{pmatrix} \gamma'_p \\ \beta'_p \gamma'_p \end{pmatrix}. \quad (112)$$

This yields  $\gamma_p = \gamma_p'^2 (1 + \beta_p'^2) = \gamma_p'^2 (1 + 1 - \gamma_p'^{-2}) = 2\gamma_p'^2 - 1 = 2(1 + m_\pi/(2m_p))^2 - 1 = 1.22 \text{ GeV}/m_p c^2$  or in terms of kinetic energy  $T_p^{\min}/m_p c^2 = \gamma_p^{\min} - 1$ , which corresponds to the lower limit of the integral in equ. (109).

To get the gamma-ray emission spectrum, we need to know the energy distribution of the produced pions during one collision. Following e.g., Stecker (1971), we consider first the decay of a particle with mass  $M$  into two particles  $m_a$  and  $m_b$ . Due to the invariant length of the four-momentum

$$\sum_{i=0}^3 (\mathbf{p}_{\text{LS}_i}^{(4)})^2 = \sum_{i=0}^3 (\mathbf{p}_{\text{CMS}_i}^{(4)})^2 \quad (113)$$

and the conservation of momentum in the CMS  $p'_a = -p'_b$ , we have the relation

$$\begin{aligned} E'^2 &= (E'_a + E'_b)^2 \\ &= (E_a + E_b)^2 - (p_a c + p_b c)^2 \\ &= m_a^2 c^4 + m_b^2 c^4 + 2E_a E_b - 2p_a p_b c^2 \end{aligned} \quad (114)$$

where the relativistic energy-momentum relation  $E^2 = m^2 c^4 + p^2 c^2$  has been used. Now we use the invariance of the inner product of the four-momentum and again  $p'_a = -p'_b$  to get

$$\begin{aligned} \left[ \mathbf{p}_a^{(4)} \cdot (\mathbf{p}_a^{(4)} + \mathbf{p}_b^{(4)}) \right]_{\text{LS}} &= \left[ \mathbf{p}_a^{(4)} \cdot (\mathbf{p}_a^{(4)} + \mathbf{p}_b^{(4)}) \right]_{\text{CMS}} \\ E_a(E_a + E_b) - p_a c(p_a c + p_b c) &= E'_a(E'_a + E'_b), \\ m_a^2 c^4 + E_a E_b - p_a p_b c^2 &= E'_a E'. \end{aligned} \quad (115)$$

This can be used in equ. (114) to obtain an expression for the CMS energy of the produced particles  $a$  and  $b$

$$E'_{a,b} = \frac{E'^2 + m_{a,b}^2 c^4 - m_{b,a}^2 c^4}{2E'} \quad (116)$$

that depends only on the masses, as can be seen when noticing that the total energy in the CMS is  $E' = Mc^2$ . Now we can use a Lorentz-transformation to the lab system where the energy of the decaying particle is  $E_M = \gamma Mc^2$ . Since only the projection of  $p'_{a,b}$  onto the boost axis, which is the direction of motion of the particle with mass  $M$ , forming an angle  $\theta'$  with the direction of motion of the outgoing particle, is transformed. Hence, we have

$$\begin{aligned} E_{a,b} &= \gamma(E'_{a,b} + p' c \beta \cos \theta') \\ &= \frac{E_M}{Mc^2} \left( \frac{M^2 + m_{a,b}^2 - m_{b,a}^2}{2Mc^2} c^4 + p'_{a,b} c \beta \cos \theta' \right). \end{aligned} \quad (117)$$

Introducing  $\eta = (M^2 + m_{a,b}^2 - m_{b,a}^2)/(2M^2)$  and  $\kappa = p'/(Mc)$  simplifies this to

$$E(\theta') = E_M(\eta + \kappa \beta \cos \theta'). \quad (118)$$

If we assume that the particle  $M$  decays isotropically, the normalized angular distribution function is  $f(\theta')d\theta' = d\Omega(\theta')/(4\pi) = 1/2 \sin \theta' d\theta'$ . This means, that the emission of a particle in the CMS is equally probable in all directions. From equ. (118) we get

$$\frac{dE(\theta')}{d\theta'} = -E_M \kappa \beta \sin \theta', \quad (119)$$

which we can then use to get the energy distribution function

$$f(E)dE = f(\theta') \left| \frac{d\theta'}{dE} \right| dE = \frac{1}{2\kappa\beta E_M} dE. \quad (120)$$

This is a constant function normalized to unity and ranges from  $E_{\min} = E_M(\eta - \kappa\beta)$  to  $E_{\max} = E_M(\eta + \kappa\beta)$  as can be checked by performing an integration from  $E_{\min}$  to  $E_{\max}$ .

We can now apply this formalism to the case of a neutral pion decaying into 2 gamma-ray photons,  $\pi^0 \rightarrow 2\gamma$ . The daughter particles have no rest mass, i.e.  $\eta = 1/2$  and  $p'_{a,b}c = E'_{a,b} = \frac{1}{2}Mc^2$ , such that  $\kappa = 1/2$ . This simplifies equ. (118), so that the parent particle is now the pion and the daughter particles are the two gamma-ray photons:

$$E_\gamma(\theta') = \frac{E_\pi}{2}(1 + \beta_\pi \cos \theta'), \quad (121)$$

and consequently, the Green's function for neutral pion decay is

$$f_{\gamma,\pi}(E_\gamma|E_\pi) = \frac{1}{\beta E_\pi} = \frac{1}{\sqrt{1 - \frac{m_\pi c^2}{E_\pi^2}} E_\pi} = \frac{1}{\sqrt{E_\pi^2 - m_\pi^2 c^4}}. \quad (122)$$

From this expression we can calculate the resulting gamma-ray spectrum with

$$q_\gamma(E_\gamma) = 2 \int_{E_{\pi,\min}}^{E_{\pi,\max}} dE_\pi \frac{q_\pi(E_\pi)}{\sqrt{E_\pi^2 - (m_\pi c^2)^2}}, \quad (123)$$

where the factor of 2 accounts for the decay of one neutral pion into two gamma-rays. The limits of the integration  $E_{\pi,\min/\max}(E_\gamma)$  are the minimum/maximum energies that are needed to produce a photon of energy  $E_\gamma$ . For highly relativistic particles, i.e.,  $\beta \rightarrow 1$ , we can further simplify equ. (121) using the general relation of the cosine,  $\cos^2(x) = 1/2(1 + \cos(2x))$ , to get

$$E_\gamma(\theta') = E_\pi \cos^2(\theta'/2). \quad (124)$$

Since  $\min(\cos^2 x) = 0$ , we can easily see that

$$E_{\pi_{max}}(E_\gamma) = \frac{E_\gamma}{\cos^2(\theta'/2)} \rightarrow \infty. \quad (125)$$

The minimum energy for the production of a photon with energy  $E_\gamma$  can be deduced from considering the extreme case, where the photons are emitted in the direction of motion, i.e.  $\theta' = 0$  or  $\pi/2$ . Energy conservation gives  $E_{\pi, \min} = E_{\gamma_{\theta'=0}} + E_{\gamma_{\theta'=\pi/2}}$ , where  $E_{\gamma_{\theta'=0}} = \frac{1}{2}E_\pi(1 + \beta_\pi)$  and  $E_{\gamma_{\theta'=\pi/2}} = \frac{1}{2}E_\pi(1 - \beta_\pi)$ . The invariant mass is obtained by multiplying both expressions together, which yields

$$(E_{\gamma_{\theta'=0}})(E_{\gamma_{\theta'=\pi/2}}) = \frac{1}{4}E_\pi^2(1 - \beta_\pi^2) = \frac{1}{4} \frac{m_\pi^2 c^4}{1 - \beta_\pi^2} (1 - \beta_\pi^2) = \frac{1}{4} m_\pi^2 c^4 \quad (126)$$

so that we are able to express  $E_{\gamma_{\theta'=\pi/2}}$  in terms of  $E_{\gamma_{\theta'=0}}$  and thus get

$$E_{\pi_{\min}} = E_{\gamma_{\theta'=0}} + \frac{m_\pi^2 c^4}{4E_{\gamma_{\theta'=0}}}. \quad (127)$$

This expression yields the energy needed to produce the maximal possible energy a photon  $E_\gamma$  can carry away. Thus, it is the lower limit of the integration over the pion energies.

To proceed, we need the differential cross-section of pion production in hadronic collisions to compute  $F(E_\pi)$  (see equ. 109). Moskalkenko and Strong (1998) put together different models at low and high energies to get a full description of secondary particle production. Their approach is discussed in the following. It is based on a method developed by Dermer (1986b), that uses two different models in the low- and high-energy regimes.

From comparison with experimental data of p-p-collisions, Dermer (1986b) writes the differential cross section as

$$\frac{d\sigma(T_\pi, T_p)}{dT_\pi} = \langle \zeta \sigma_\pi(T_p) \rangle \frac{dN(T_\pi, T_p)}{dT_\pi} \quad (128)$$

with the inclusive cross section of neutral pion production  $\langle \zeta \sigma_\pi(T_p) \rangle$ , that takes into account all corresponding channels and is being fitted to the experimental data as

$$\langle \zeta \sigma_\pi(T_p) \rangle [\text{mbarn}] = \begin{cases} 0.032\eta^2 + 0.040\eta^6 + 0.047\eta^8, & p_p^{thr} \leq p_p \leq 0.96, \\ 32.6(p_p - 0.8)^{3.21}, & 0.96 \leq p_p \leq 1.27, \\ 5.4(p_p - 0.8)^{0.81}, & 1.27 \leq p_p \leq 8.0, \\ 32.0 \ln(p_p) + 48.5p_p^{-0.5} - 59.5, & 8.0 \leq p_p, \end{cases} \quad (129)$$

where  $p_p$  has to be given in units of GeV/c. As pointed out in Dermer (1986a), at proton energies near the threshold, i.e., below kinetic proton energies of  $T_p < 3$  GeV, the model of Stecker (1970) agreed well with the experimental data at that time. The production of neutral pions is here explained by the decay of the  $\Delta_{3/2}$  isobar that is excited during the p-p-collision. The mass distribution of the outgoing isobars, that carry momentum either directly forward or directly backward in the CMS, is given by the normalized Breit-Wigner distribution

$$B(m_\Delta) = \Gamma \left[ \tan^{-1} \left( \frac{\sqrt{s} - m_p c^2 - m_\Delta^0}{\Gamma} \right) - \tan^{-1} \left( \frac{m_p c^2 - m_\pi c^2 - m_\Delta^0}{\Gamma} \right) \right] \cdot [(m_\Delta - m_\Delta^0)^2 + \Gamma^2]^{-1}. \quad (130)$$

Assuming that the isobar decays isotropically into a proton and a neutral pion, the distribution of the

pions in the lab system is

$$f_\pi(T_\pi, T_p, m_\Delta) = \frac{1}{4m_\pi\gamma'_\pi\beta'_\pi} \left\{ \frac{1}{\gamma_\Delta^+\beta_\Delta^+} H[\gamma_\pi; a^+, \gamma_\Delta^+\gamma'_\pi(1 + \beta_\Delta^+\beta'_\pi)] + \frac{1}{\gamma_\Delta^-\beta_\Delta^-} H[\gamma_\pi; a^-, \gamma_\Delta^-\gamma'_\pi(1 + \beta_\Delta^-\beta'_\pi)] \right\}, \quad (131)$$

where  $H[x; a, b] = 1$  if  $a \leq x \leq b$  and  $= 0$  otherwise,  $a^\pm = \gamma_\Delta^\pm\gamma'_\pi(1 - \beta_\Delta^\pm\beta'_\pi)$  with the Lorentz factors of the forward and backward moving isobars in the lab system  $\gamma_\Delta^\pm = \gamma_c\gamma_\Delta^*(1 \pm \beta_c\beta_\Delta^*)$ , the Lorentz factor of the isobar in the CMS is  $\gamma_\Delta^* = (s + m_\Delta^2c^4 - m_p^2c^4)/2\sqrt{s}m_\Delta c^2$  as well as the pion Lorentz factor in the rest frame of the  $\Delta$ -isobar is  $\gamma'_\pi = (m_\Delta^2 + m_\pi^2 - m_p^2)/2\sqrt{s}m_\Delta m_\pi$  and the Lorentz factor of the CMS in the lab system is  $\gamma_c = \sqrt{s}/2m_p c^2$ . The variable  $s$  denotes here the square of the total energy in the CMS, such that  $\sqrt{s} = [2m_p c^2(E_p + m_p c^2)]^{1/2}$ .

Using equ. (130) and (131) one can obtain the distribution of pions in this model by integrating over  $m_\Delta$

$$\frac{dN(T_\pi, T_p)}{dT_\pi} = \int_{m_p c^2 + m_\pi c^2}^{\sqrt{s} - m_p c^2} dm_\Delta \cdot B(m_\Delta) \cdot f_\pi(T_\pi, T_p, m_\Delta). \quad (132)$$

Above 7 GeV, Dermer (1986b) proposes the model presented in Stephens and Badhwar (1981), which is based on scaling arguments, to be the best fit to the experimental data at that time. It makes use of the Lorentz invariant cross section  $E_\pi d^3\sigma/dp_\pi^3$  for pion production in p-p-collisions that can be inferred from experimental data at  $E_p \geq 13.5$  GeV to calculate the differential cross section for the production of a neutral pion of energy  $E_\pi$  from a proton with energy  $E_p$  as

$$\frac{d\sigma(E_\pi, E_p)}{dE_\pi} = 2\pi p_\pi \int_{\cos\theta_{\max}}^1 d\cos\theta \left( E_\pi \frac{d^3\sigma}{dp_\pi^3} \right) \quad (133)$$

where, provided  $-1 \leq \cos\theta_{\max} \leq 1$ ,

$$\cos\theta_{\max} = \frac{1}{\beta_c\gamma_c p_\pi} \left( \gamma_c E_\pi - \frac{s - m_X^2 c^4 + m_\pi^2 c^4}{2\sqrt{s}} \right). \quad (134)$$

They also showed that a general fit to the accelerator data of the invariant cross section can be written as

$$E_\pi \frac{d^3\sigma}{dp_\pi^3} = A f(E_p) (1 - \tilde{x})^q \exp[-B p_\perp / (1 + 4m_p^2 c^4 / s)] \quad (135)$$

where  $\tilde{x} = \sqrt{x_\parallel^{*2} + (4/s)(p_\perp^2 c^2 + m_\pi^2 c^4)}$ ,  $x_\parallel^*$  is the ratio of the parallel component of the pion momentum in the CMS, that is  $p_\parallel^* = p_\pi^* \cos\theta^*$ , to the maximum pion momentum

$$p_{\max}^* = \frac{\left[ (s - m_X^2 c^4 - m_\pi^2 c^4)^2 - 4m_\pi^2 m_X^2 c^8 \right]^{0.5}}{2m_\pi c^2 \sqrt{s}}$$

and

$$q = (C_1 - C_2 p_\perp + C_3 p_\perp^2) / \sqrt{1 + 4m_p^2 c^4 / s}.$$

The function  $f(E_p) = (1 + 23E_p^{-2.6})(1 - 4m_p^2 c^4 / s)^r$  and the constants in equ. (135) are fitted to the experimental data to  $A = 140, B = 5.43, C_1 = 6.1, C_2 = 3.3$  and  $C_3 = 0.6$ . The transverse pion momentum  $p_\perp = p \sin\theta$  is an invariant under the transformation from the lab frame to the CMS, but for

the transformation of the parallel component one needs the relation  $\tan \theta^* = \sin \theta / [\gamma_c (\cos \theta - \beta_c E_\pi / p_\pi c)]$

Between 3 and 7 GeV, a linear interpolation between the isobaric model and the scaling model is used by Dermer (1986a) and thus also in Moskalenko and Strong (1998), who published a numerical code for Galactic Cosmic Ray Propagation (GALPROP), where they model CR transport and also their emission products, including gamma-ray emission from neutral pion decay.

Besides the approach in GALPROP described above, Pfrommer and Enßlin (2004) derived an analytical expression for the gamma-ray source function. They aimed for connecting the high energy limits for the gamma-ray source function to the detailed physics near the threshold of neutral pion production that have been modeled with the COSMOCR code (Miniati 2001), that is based on the isobaric model explained above and also takes into account the contribution of kaon decay modes to the neutral pion production. The resulting analytical formula is given by

$$q_\gamma \simeq \sigma_{pp} c n_N \xi^{2-a_\gamma} C_p \frac{4}{3a_\gamma} \left( \frac{m_\pi}{m_p} \right)^{-a_\gamma} \left[ \left( \frac{2E_\gamma}{m_\pi c^2} \right)^{\delta_\gamma} + \left( \frac{2E_\gamma}{m_\pi c^2} \right)^{-\delta_\gamma} \right] \quad (136)$$

where it is assumed that the proton momentum distribution is normalized to  $m_p c$ . The asymptotic slope of the gamma-ray spectrum  $a_\gamma$  is the same as the spectral index of the proton population in the scaling model, that has also been adopted by Dermer (1986b). Furthermore, the parameter  $\delta_\gamma$  and the total effective cross section  $\sigma_{pp}$  have been modeled by Pfrommer and Enßlin (2004) as

$$\delta_\gamma = 0.14a_\gamma^{-1.6} + 0.44 \quad (137)$$

and

$$\sigma_{pp} = 32 \times (0.96 + \exp(4.4 - 2.4a_\gamma)) \text{ mbarn}. \quad (138)$$

Additionally, there exist nowadays several codes of simulations of pp-interactions that combine experimental data from particle accelerators with phenomenological models of pp-interactions, such as Pythia, SIBYLL, QGSJET and Geant4. Nevertheless, it is still useful to have analytical expressions that fit their simulations within a few percent accuracy to reduce the calculation time as well as to get a better understanding of the underlying physical processes and the impact of specific spectral features of cosmic rays on the resulting radiation. Therefore, there have been made several parametrisations based on simulation codes to describe the cross sections for secondary particle production in pp-collisions that are valid in different energy regimes.

As pointed out in Yang et al. (2018), it is specifically important to know the cross section near the kinematic threshold to be able to determine the pion decay bump accurately. Thus, they focused on proton energies below 10 GeV and used the hadronic interaction model from the Geant4 Toolkit to parametrize the differential cross section for pion production as

$$\frac{d\sigma_\pi}{dx} = \sigma_\pi \times f(x, T_p) \quad (139)$$

where  $x = T_\pi / T_\pi^{\max}$  and  $\sigma_\pi$  is the total cross section of pion production, for charged and neutral pions respectively. They give a parametrization for the normalized pion energy distribution  $f(x, T_p)$  and use for the total cross section  $\sigma_\pi$  the existing experimental data for  $T_p \leq 2 \text{ GeV}$ . For larger energies,  $T_p > 2 \text{ GeV}$ , the cross section can be expressed as

$$\sigma_\pi = \sigma_{pp}^{\text{inel}} \langle n_\pi \rangle. \quad (140)$$

Here, the pion average yield is parametrized as  $\langle n_\pi \rangle = 0.78(w - 2)^{3/4} w^{-1/4} - 1/2 + \varepsilon$  with  $w = \sqrt{s} / m_p c^2$  and  $\varepsilon = 0$  for  $\pi^-$ ,  $1/3$  for  $\pi^0$  and  $2/3$  for  $\pi^+$  (where we need the charged pions in the next chapter). This is done by using experimental data from Golokhvastov (2001). The resulting curves of the total cross sections are shown in Fig. 8, where the red dashed lines show the parametrisations used in Yang et al. (2018) and the points are the experimental data that they refer to. The black dashed lines show the corresponding parametrisations given by Dermer (1986b), where the formulae for neutral pion production are given in equ. (129), the channels involving charged pions are discussed in the next chapter. For  $\sigma_{\pi^0}$ , Yang et al. (2018) use the formulas provided by Kafexhiu et al. (2014) in the energy range below 2 GeV.

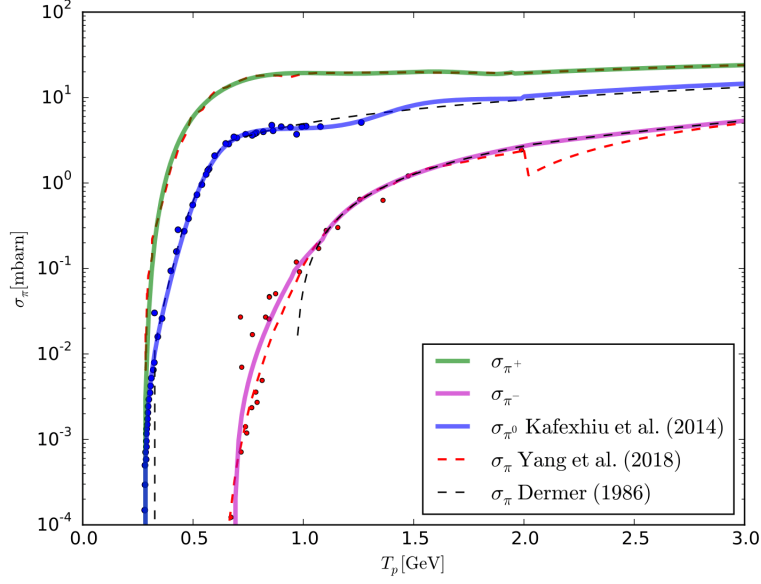


Figure 8: Total cross sections of  $\pi^0$  and  $\pi^\pm$  production. Data points are taken from the compilation in Yang et al. (2018) and the solid lines represent the parametrisations that are going to be used in my code later on.

We show this model as the solid blue line, which takes into account all neutral pion production channels, i.e.  $pp \rightarrow pp\pi^0$ ,  $pp \rightarrow pp2\pi^0$  as well as  $pp \rightarrow p\pi^+\pi^0$  and  $pp \rightarrow D\pi^+\pi^0$ . Above 2 GeV, the inelastic cross section in equ. (140) is used also from Kafexhiu et al. (2014), who give the following expression

$$\sigma_{pp}^{\text{inel}}(T_p) = \left[ 30.7 - 0.96 \log\left(\frac{T_p}{T_p^{\text{th}}}\right) + 0.18 \log^2\left(\frac{T_p}{T_p^{\text{th}}}\right) \right] \times \left[ 1 - \left(\frac{T_p}{T_p^{\text{th}}}\right)^{1.9} \right]^3 \text{ mbarn} \quad (141)$$

with the threshold proton kinetic energy  $T_p^{\text{th}} = 2m_{\pi^0}c^2 + m_{\pi^0}^2c^4/2m_p c^2 \approx 0.2797$  GeV.

Since equ. (139) is only given for proton kinetic energies  $T_p < 10$  GeV, another parametrisation needs to be used at higher energies. On the one hand, Kelner et al. (2006) provide analytical expressions of energy spectra of secondary particles from proton-proton collisions with  $T_p > 100$  GeV, which are frequently being used in the literature. Besides secondary  $\pi$ -mesons, electrons and neutrinos, they also provide a parametrisation for the resulting gamma-ray emission from neutral pion decay as a function of proton and photon energies, which implies the number of photons in the interval  $(x, x + dx)$  per collision

$$F_\gamma(x, E_p) = B_\gamma \frac{\ln x}{x} \left( \frac{1 - x^{\beta_\gamma}}{1 + k_\gamma x^{\beta_\gamma} (1 - x^{\beta_\gamma})} \right)^4 \times \left[ \frac{1}{\ln x} - \frac{4\beta_\gamma x^{\beta_\gamma}}{1 - x^{\beta_\gamma}} - \frac{4k_\gamma \beta_\gamma x^{\beta_\gamma} (1 - 2x^{\beta_\gamma})}{1 + k_\gamma x^{\beta_\gamma} (1 - x^{\beta_\gamma})} \right] \quad (142)$$

with  $x = E_\gamma/E_p$  and the fitted parameters  $B_\gamma = 1.30 + 0.14L + 0.011L^2$ ,  $\beta_\gamma = (1.79 + 0.11L + 0.008L^2)^{-1}$  and  $k_\gamma = (0.801 + 0.049L + 0.014L^2)^{-1}$ , where  $L = \ln(E_p/1 \text{ TeV})$ . It needs to be convolved with the proton energy distribution  $J_p(E_p)$  and the inelastic cross section of pp-interactions to get the gamma-ray production rate in the energy interval  $(E_\gamma, E_\gamma + dE_\gamma)$  to be

$$q_\gamma(E_\gamma) = cn_H \int_{E_\gamma}^{\infty} \sigma_{\text{inel}}(E_p) J_p(E_p) F_\gamma \left( \frac{E_\gamma}{E_p}, E_p \right) \frac{dE_p}{E_p}. \quad (143)$$

Note that for the proton energy distribution one needs to use equ. (104) in order to get the gamma-ray source function in the right units. They fit the numerical data in the SYBILL code to get the inelastic part of the total cross section of pp-interactions as  $\sigma_{\text{inel}}(E_p)/\text{mb} = 34.3 + 1.88L + 0.25L^2$  and multiply this by a factor of  $(1 - (E_{\text{th}}/E_p)^4)^2$  to better fit experimental data in the low energy regime. For low proton kinetic energies ( $T_p < 100\text{GeV}$ ) they suggest a  $\delta$ -functional approach for the production rate of pions to be able to calculate the gamma-ray spectrum also below their analytical expressions that are only valid in the high energy regime. They adopt for the production rate of pions the approximation

$$\tilde{F}_\pi(E_\pi, E_p) = \tilde{n} \delta \left( E_\pi - \frac{\kappa}{\tilde{n}} E_{\text{kin}} \right) \quad (144)$$

where  $\tilde{n} = \int \tilde{F}_\pi dE_\pi$  being the number of produced pions and  $\kappa$  is the fraction of kinetic energy of the proton transferred to gamma rays. This can be used to obtain a simple expression for the pion source function

$$F_\pi(E_\pi) = \tilde{n} \frac{cn_H}{K_\pi} \sigma_{\text{inel}} \left( m_p c^2 + \frac{E_\pi}{K_\pi} \right) J_p \left( m_p c^2 + \frac{E_\pi}{K_\pi} \right) \quad (145)$$

that can in turn be inserted into equ. (123) to calculate the corresponding gamma-ray emission. The parameter  $K_\pi = \kappa/\tilde{n} = 0.17$  agrees well with numerical Monte Carlo simulations as demonstrated in Aharonian and Atoyan (2000).

On the other hand, more recently, Kafexhiu et al. (2014) published a parametrisation of the differential gamma-ray cross section for a wide energy range of proton energies by combining experimental data below 2 GeV and the publicly available codes at higher energies. They give their results in form of a differential cross section for gamma-ray production

$$\frac{d\sigma_\gamma(T_p, E_\gamma)}{dE_\gamma} = A_{\text{max}}(T_p) F(T_p, E_\gamma) \quad (146)$$

which can be used in equ. (108) with  $s = \gamma$  to obtain the gamma-ray source function  $q_\gamma$ . They fit  $A_{\text{max}}(T_p) = \max(d\sigma_\gamma/dE_\gamma)$  separately from  $F(T_p, E_\gamma)$  since the maximum value only depends on the proton energy  $T_p$ . It is a function of the total  $\pi^0$ -production cross section  $\sigma_\pi(E_p)$ , for which they also produce their own fits. In the high-energy regime, they divide the cross section into the inelastic part and the pion multiplicity, see equ. (140), and use for  $\sigma_{\text{inel}}^{\text{pp}}$  equ. (141). This fits new experimental data from Beringer et al. (2012) in the very high energy regime around  $T_p = 10^7$  GeV better than e.g., the one used by Kelner et al. (2006). They furthermore provide their own fit to the average pion multiplicity  $\langle n_{\pi^0} \rangle$ , that agrees well with the description used by Yang et al. (2018), which refers to data from Golokhvastov (2001).

Furthermore, Kafexhiu et al. (2014) compare their new results to the ones by Kamae et al. (2006), who take into account the diffractive interaction of proton-proton collisions additional to the non-diffractive description by Blattnig et al. (2000) and Stephens and Badhwar (1981), and use the Pythia code for higher proton energies. Similarly to the approach by Stephens and Badhwar (1981) in equ. (135), Blattnig et al. (2000) also fit the invariant  $\pi^0$  production differential cross section to experimental data in order to calculate a gamma-ray spectrum from that. It turns out that the model by Kamae et al. (2006) does not fit the new approach by Kafexhiu et al. (2014) and violates the symmetry of the gamma-ray spectrum with respect to  $E_\gamma = m_\pi c^2/2$ .

In my approach, I use the parametrisation by Yang et al. (2018) for  $T_p < 10$  GeV and the model by Kafexhiu et al. (2014) at larger energies, which is shown by the black solid line in Fig. 9. It agrees well with the model by Dermer (1986b) near the threshold of pion production, i.e., around  $m_{\pi^0} c^2/2 \approx 67.5$  MeV, whereas the latter seems to over-predict the gamma-ray source function at higher energies. The delta-function approximation by Kelner et al. (2006) for low proton energies can be recognized by the sharp peak. The analytical approximation by Pfrommer and Enklin (2004) from equ. (136) agrees well with the

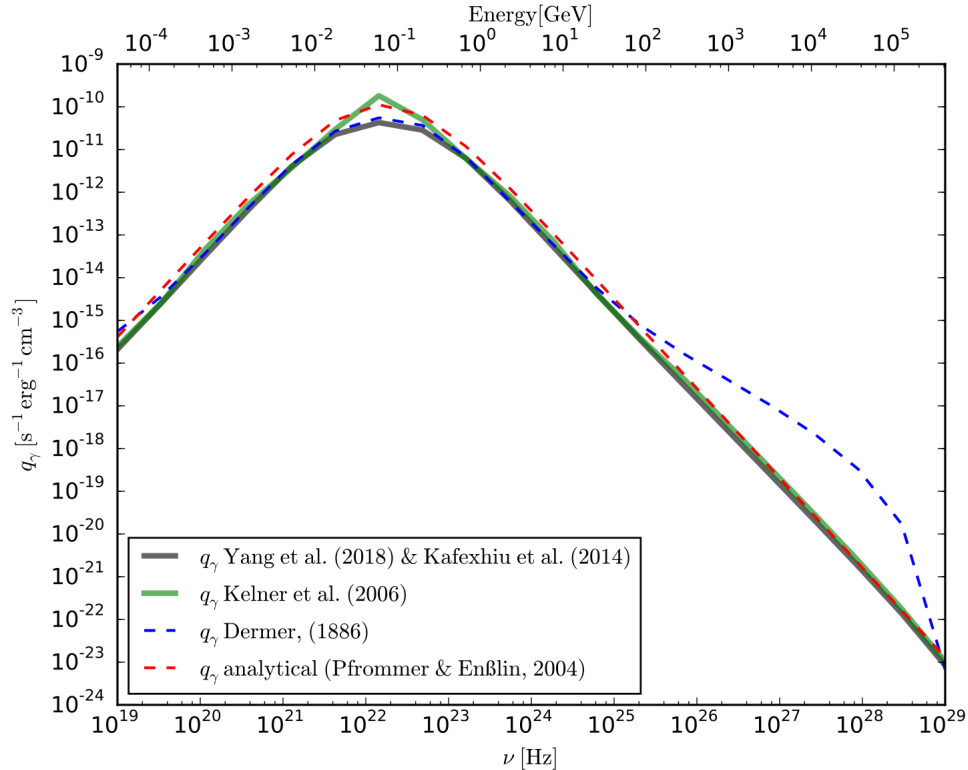


Figure 9: Comparison of different models for the gamma-ray source function.

more exact parametrization, except directly at the threshold energy, that corresponds to the peak of the gamma-ray source function, where it over-predicts the resulting emission.

So far, the ambient gas was assumed to consist of protons only. The effect of relativistic protons interacting with nuclei heavier than hydrogen was recently studied by Yang et al. (2018), who also gave the parametrization for the pion production cross section in equ. (139). Whereas at high energies these interactions can be described by a sequence of binary nucleon-nucleon collisions according to the Glauber’s multiple scattering theory (Glauber, 1955), there are two additional processes that occur at lower, sub-relativistic energies, for which still no self-consistent theory exists. On the one hand, intra-nuclear collisions can lead to the production of pions below the kinematic threshold, which is called sub-threshold pion production. On the other hand, so called direct photons are emitted, probably due to neutron-proton-Bremsstrahlung during the early stage of the nuclear interaction. The cross sections for these processes have been parametrized by Kafexhiu (2016). Yang et al. (2018) used them to analyze the contribution from heavy nuclei to the gamma-ray emission from hadronic interactions from Galactic CRs with the interstellar gas and found a very similar spectral shape when including heavy nuclei compared to only considering pp-interactions, but found an overall higher emissivity by a nuclear enhancement factor of  $a_{\text{nucl}} = 1.8$ . Therefore, for a chemical composition of CR protons and ISM similar to our Galaxy and a similar spectral shape of CRs, the multiplication of the gamma-ray emission spectrum by a nuclear enhancement factor seems to account for all contributions from heavy nuclei quite well.

### 2.2.2 Secondary Electrons and Positrons

As explained in Section 2.2.1, hadronic collisions lead to the production of charged pions that decay further into muons and consequently into electrons and positrons, depending on the charge of the created pion. First, a simple formula for the electron source function shall be derived, as it is useful to compare

it to the exact results later on. Following Stecker (1971) and Mannheim and Schlickeiser (1994) and assuming isospin symmetry, which means that the multiplicity of neutral pions is half that of charged pions,  $\xi_{\pi^0} = \xi_{\pi^\pm}/2$ , one can derive the pion source function from a simple delta approximation for the production of pions

$$\frac{d\sigma(E_\pi, E_p)}{dE_\pi} = \xi(E_p)\sigma_{pp}^\pi(E_p)\delta(E_\pi - \langle E_\pi \rangle)\theta(E_p - E_{th}) \quad (147)$$

to be

$$q_{\pi^\pm}(E_{\pi^\pm}) = \frac{2}{3}cn_H \int dE_p N_p(E_p) \frac{d\sigma(E_\pi, E_p)}{dE_\pi} \quad (148)$$

for a proton energy distribution  $N_p(E_p)$ . At high energies, one can furthermore assume a constant pion multiplicity  $\xi = 2$  as well as a mean pion energy  $\langle E_\pi \rangle(E_p) \simeq K_p T_p / \xi \simeq T_p / (2\xi)$ , where the inelasticity  $K_p$  was assumed to be roughly 1/2. In the high-energy limit, the proton power-law distribution in momentum is also a power-law distribution in energy, since  $\gamma_p = E_p / (m_p c^2) = \sqrt{1 + p_p^2 / (m_p c)^2} \approx p_p / (m_p c)$  for  $p_p / m_p c \gg 1$  and furthermore,  $T_p / (m_p c^2) = \gamma_p - 1 \approx \gamma_p$ . If the energy distribution is given by a power-law with spectral index  $a_p$  and normalization factor  $C_p$ , we obtain the expression

$$\begin{aligned} q_{\pi^\pm} &= \frac{4}{3} \xi^{2-a_p} cn_H C_p \sigma_{pp}^\pi(a_p) (2E_\pi)^{-a_p} \\ &= \frac{16}{3} cn_H C_p \sigma_{pp}^\pi(a_p) (4E_\pi)^{-a_p}. \end{aligned} \quad (149)$$

Note that the pion energy needs to be given in units of  $m_p c^2$  here, since we have been assuming a proton power-law distribution in  $\gamma_p$ . In this approximation, the effective inelastic cross section  $\sigma_{pp}^\pi$  was modeled by Pfrommer and Enßlin (2004), see equ. (138), which also accounts for kaon decay modes.

Transforming the distribution of pions into a distribution of electrons/positrons

$$q_{\pi^\pm} dE_{\pi^\pm} = q_{e^\pm} dE_{e^\pm} \quad (150)$$

and estimating the mean energy of the produced electrons or positrons from the decay channel  $\pi^\pm \rightarrow e^\pm + 3\nu$  to be  $\langle E_{e^\pm} \rangle = \langle E_{\pi^\pm} \rangle / 4$  leads to

$$q_{e^\pm}(E_{e^\pm}) = q_{\pi^\pm} [E_{\pi^\pm}(E_e)] \frac{dE_{\pi^\pm}}{dE_{e^\pm}} = 4q_{\pi^\pm}(4E_{e^\pm}). \quad (151)$$

Combining this with equ. (149) gives

$$q_{e^\pm}(E_{e^\pm}) = \frac{64}{3} cn_H C_p \sigma_{pp}^\pi(a_p) (16E_{e^\pm})^{-a_p}. \quad (152)$$

The resulting electron energy distribution can be inferred from the fact that the source function is a production rate that is acting on a characteristic timescale of pp-interactions

$$\tau_{pp} = (nc\sigma_{pp})^{-1}. \quad (153)$$

Therefore, we have for instance in the case of a spectral index of  $a_p = 2.1$  that the electron distribution is a factor of  $64/3 \times 16^{-2.1} \approx 0.063$ , which is approximately 1/16, smaller than the initial proton energy distribution.

Similarly to the previous section for the production rate of gamma-rays from neutral pion decay, there exist also several parameterizations for a more exact description of the differential cross section of charged pion production, of the total cross-section as a function of proton energy as well as directly of the production rate of secondary electrons and positrons.

In the low energy range near the pion production threshold,  $T_p < 10$  GeV, again Yang et al. (2018) give the most recent description for the differential pion production cross section (equ. 139). The total cross sections they use for the charged pion production are shown in Fig. 8 with red dashed lines respectively.

In the case of negative pions, one can clearly see the discontinuity at  $T_p = 2 \text{ GeV}$ , where they change from a fit to the data for  $T_p < 2 \text{ GeV}$  to a description using the pion average yield by Golokhvastov (2001) and the total inelastic cross section from Kafexhiu et al. (2014) (see equ. 140 and text below). The black dashed line shows the approach by Dermer (1986b), that only starts at  $T_p = 0.95 \text{ GeV}$  for  $\sigma_{\pi^-}$  and an interpolation to lower energies would lead to an underestimation of the cross section compared to the experimental data. Since Yang et al. (2018) do not give an expression for their fit to the data points below  $2 \text{ GeV}$ , I fitted the data points up to  $T_p \leq 1.1 \text{ GeV}$  and used the parametrization by Dermer (1986b) for higher proton energies, which leads to the magenta solid line in Fig. 8. For the cross section of positive pion production, I fitted the curve from Fig. 4 in Yang et al. (2018), that is a sum of all channels leading to the production of positive pions. In this case, it smoothly connects to the description of the cross section for  $T_p > 2 \text{ GeV}$  from equ. (140).

In order to obtain a resulting production rate of electrons and positrons with equ. (108), we first need the normalized electron/positron decay energy distribution  $f_{\pi^\pm}(E_{\pi^\pm}, E_{e^\pm})$  to calculate  $d\sigma_{e^\pm}(E_{e^\pm}, E_p)/dE_{e^\pm}$  from equ. (107). This has been derived by Dermer (1986b), assuming a mono-energetic, unpolarized, isotropic distribution of pions with Lorentz factor  $\gamma_\pi$ , in whose rest frame muons with a Lorentz factor of  $\gamma_\mu = (m_\mu^2 + m_\pi^2)/2m_\pi m_\mu$  and  $\beta_\mu \approx 0.2714$  are created. Defining the functions

$$\begin{aligned} g_1(y) &= \frac{8\gamma_\mu^5}{\beta_\pi \gamma_\pi m_\mu} \left[ (3 - u\beta_\mu^2) (1 - \beta_\mu^2) \frac{y^2}{2} - \frac{4}{9} (3 + \beta_\mu^2 - 4u\beta_\mu^2) y^3 \right], \\ g_2(y) &= (6\beta_\mu \gamma_\mu \beta_\pi \gamma_\pi m_\mu)^{-1} \left[ (5 + u) \ln y - \frac{6(u + 2u\beta_\mu + 3) y^2}{(1 + \beta_\mu)^2} + \frac{16(u + 3u\beta_\mu + 2) y^3}{3(1 + \beta_\mu)^3} \right] \end{aligned} \quad (154)$$

with  $u \equiv \xi/\beta_\mu$ , where  $\xi = 1$  for the production of electrons and  $-1$  for positrons, yields

$$f_{\pi^\pm}(E_{\pi^\pm}, E_{e^\pm}) = \begin{cases} g_1(y_2) - g_1(y_1), & y_1 < y_2 < y_-, \\ g_2(y_2) - g_2(y_-) + g_1(y_-) - g_1(y_1), & y_1 < y_- < y_2 < y_+, \\ g_+(y_2) - g_2(y_-) + g_1(y_-) - g_1(y_1), & y_1 < y_- < y_+ < y_2, \\ g_2(y_2) - g_2(y_1), & y_- < y_1 < y_2 < y_+, \\ g_2(y_+) - g_2(y_1), & y_- < y_1 < y_+ < y_2, \\ 0, & y_+ < y_2. \end{cases} \quad (155)$$

Here,  $y_1 \equiv E_e/\gamma_\pi \gamma_\mu m_\mu c^2 (1 + \beta_\pi)$ ,  $y_2 \equiv E_e/\gamma_\pi \gamma_\mu m_\mu c^2 (1 - \beta_\pi)$ ,  $y_- = (1 - \beta_\mu)/2$  and  $y_+ = (1 + \beta_\mu)/2$ . The limits in the integral of equ. (107) are  $E_\pi^{\max} = \infty$  and  $E_\pi^{\min} = m_\pi c^2$  if  $E_e < E_e^{\max} = 1/2 m_\mu c^2 (1 + \beta_\mu) \gamma_\mu \approx 69.9 \text{ MeV}$  and  $E_\pi^{\min} = 1/2 m_\pi c^2 (E_e/E_e^{\max} + E_e^{\max}/E_e)$  if  $E_e > E_e^{\max}$ . Thus, equ. (155) together with the differential cross section in equ. (139), using the corresponding formulas for charged pions, the electron/positron source function is from equ. (108) and (107) given by

$$q_{e^\pm}(E_{e^\pm}) = cn_H \int_{E_p^{\min}}^{\infty} dE_p J_p(E_p) \int_{E_\pi^{\min}}^{E_\pi^{\max}} dE_\pi \frac{d\sigma(E_p, E_\pi)}{dE_\pi} f_{s,\pi}(E_s, E_\pi). \quad (156)$$

In the high-energy range of protons,  $T_p > 100 \text{ GeV}$ , Kelner et al. (2006) also provide an analytical parametrization for the production rate of secondary electrons from the SYBILL code. It is given in terms of a function  $F_e(x, E_p)$  that describes the number of produced electrons per collision in the interval  $(x, x + dx)$  with  $x = E_e/E_p$  and reads as

$$F_e(x, E_p) = B_e \frac{(1 + k_e (\ln x)^2)^3}{x(1 + 0.3/x^{\beta_e})} (-\ln(x))^5 \quad (157)$$

with  $B_e = (69.5 + 2.65L + 0.3L^2)^{-1}$ ,  $\beta_e = (0.201 + 0.062L + 0.00042L^2)^{-0.25}$  and  $k_e = (0.279 + 0.141L + 0.0172L^2)/(0.3 + (2.3 + L)^2)$ , where  $L = \ln(E_p/\text{TeV})$ . Plugging this into equ. (143) instead of  $F_\gamma$  leads to

the production rate of electrons

$$q_e(E_e) = cn_H \int_{E_e}^{\infty} \sigma_{\text{inel}}(E_p) J_p(E_p) F_e \left( \frac{E_e}{E_p}, E_p \right) \frac{dE_p}{E_p}. \quad (158)$$

Here,  $J_p(E_p)$  relates to  $N_p(E_p)$  as pointed out in equ. (104). In my code, I am adopting the model by Yang et al. (2018) for the low energy range  $T_p < 10$  GeV, the description by Kelner et al. (2006) for  $T_p > 100$  GeV and a linear interpolation in between.

To transform the resulting production rate, which has units  $[1/\text{erg}/\text{cm}^3/\text{s}]$ , into a spectrum of secondary electrons  $N_e(\gamma_e)$ , the characteristic timescale for inelastic pp-collisions  $\tau_{\text{pp}} \simeq (cn\sigma_{\text{pp}}^{\text{inel}})^{-1}$  can be used to obtain

$$N_e(\gamma_e) = \tau_{\text{pp}} q_e(E_e) dE_e / d\gamma_e = \tau_{\text{pp}} q_e(E_e) m_e c^2. \quad (159)$$

### 3 From the Simulation of a Galaxy to its Multi-frequency Spectrum

Using the adaptive moving-mesh code AREPO (Springel 2010; Pakmor et al. 2016), Pfrommer et al. (2017b) performed simulations of isolated galactic disks. These are embedded in dark-matter halos with masses ranging from  $M_{200} = 10^{10}$  to  $10^{12} M_{\odot}$  and thus covering the typical halo sizes from dwarf galaxies to Milky Way-like galaxies. Following Pfrommer et al. (2017a), CRs are being injected instantaneously in the surroundings of core-collapse supernovae, such that the energy injection at each time step is modeled by  $\Delta E_{\text{CR}} = \xi_{\text{SN}} \epsilon_{\text{SN}} \dot{m}_* \Delta t$ , where the CRs are assumed to receive a fraction of  $\xi_{\text{SN}} = 0.1$  of the released kinetic energy of a supernova explosion. Here,  $\dot{m}_*$  is the star formation rate of the mesh cell and  $\epsilon_{\text{SN}} = 10^{49} \text{erg } M_{\odot}^{-1}$  accounts for one supernova explosion for every  $100 M_{\odot}$ , which can be obtained by assuming a Kroupa initial mass function (Kroupa 2001). Subsequently, CRs are advected with the gas and adiabatic changes in the CR energy as well as non-adiabatic changes are taken into account. The latter include the two main collisional loss processes of CR protons propagating through the ISM, i.e., losses due to Coulomb interactions of protons with a plasma and hadronic losses, where protons lose their energy by the interactions with the thermal ISM as discussed in Section 2.2. As a result of continuous injection and losses, an equilibrium spectrum is obtained, following Enßlin et al. (2007). The corresponding energy density of the CRs is given as  $\epsilon_{\text{CR}}$  for every cell and is the starting point for the flow chart in Fig. 10. Since the balance between injection and losses is only taken into account for CR protons, the injected electron energy spectrum, which we derive from the proton spectrum using the proton to electron ratio  $K_{\text{ep}}$  from equ. (9), has to be developed further, as discussed in the following.

#### 3.1 Steady-State Equation

As the injected CR particles move through the ISM, they can be scattered by irregularities in the magnetic field such that their motion can be described by a diffusion process, characterized by a coefficient  $D$ . Furthermore, they undergo several energy loss processes, e.g., radiation losses that have been discussed in Section 2, where at the same time new particles can be injected. To obtain the CR electron's equilibrium spectrum, which is a result of the competition between all loss and gain processes, a partial differential equation for the energy spectrum at each point in the ISM can be derived by an elementary approach, following Longair (2011). We start with an energy spectrum of particles  $N(E)dE$  which are subject to an energy loss process that can be described by the corresponding energy loss rate as

$$b(E) = -\frac{dE}{dt}.$$

We consider the change in the particle distribution during a time interval  $\Delta t$ , where at the beginning at time  $t$  the number of particles is  $N(E)\Delta E$  in a unit volume in the energy range  $E$  to  $E + \Delta E$ . In this interval are different particles after some time  $t + \Delta t$ , which before had energies in the range  $E' + \Delta E'$

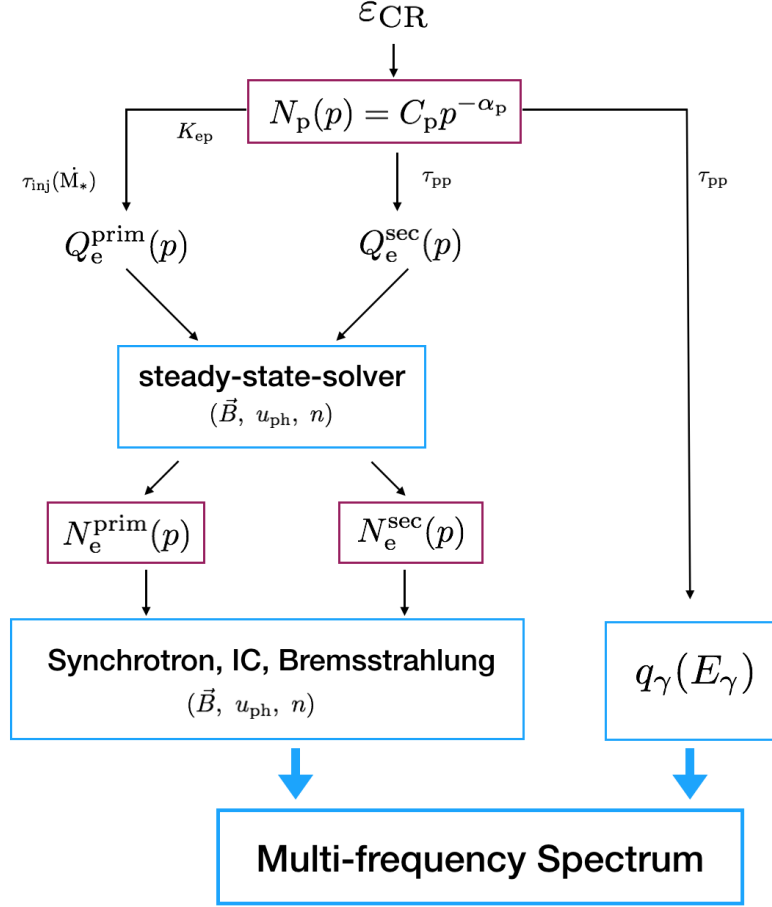


Figure 10: Flow-chart for the calculation of a multi-frequency spectrum, starting from a CR energy density  $\varepsilon_{\text{CR}}$ , that gives the normalization of the CR proton spectrum. Assuming a power law index  $a_p$  and an electron-to-proton ratio  $K_{\text{ep}}$  yields together with a characteristic timescale of injection (equ. 168) the injection spectrum of primary electrons. The proton spectrum also yields the production spectrum of secondary electrons and positrons, that experience the same cooling processes as the primary electron spectrum. These are accounted for by solving the diffusion loss equation in the steady-state approximation (167) taking into account all occurring energy loss processes. From the resulting cooled leptonic spectra the non-thermal emission processes are computed, which yield together with the gamma-ray emission from neutral pion decay, directly obtained from the proton spectrum, the multi-frequency emission spectrum.

at time  $t$ . They can get into the interval  $E + \Delta E$  during time  $\Delta t$  only by either gaining or losing energy, i.e.

$$E' = E + b(E)\Delta t \quad (160)$$

and

$$E' + \Delta E' = (E + \Delta E) + b(E + \Delta E)\Delta t. \quad (161)$$

The changed particle distribution is thus given by

$$N(E, t)\Delta E + \Delta N(E)\Delta E = N[E + b(E)\Delta t, t] \Delta E'. \quad (162)$$

A Taylor expansion of the last term for small  $b(E)\Delta t$  yields  $N[E + b(E)\Delta t, t] = N(E) + (dN/dE)b(E)\Delta t$ .

We can now perform another Taylor expansion for small values of  $\Delta E$ , which leads to  $b(E + \Delta E) = b(E) + (db/dE)\Delta E$ . Using this in equ. (161) and subtracting the result by (160) gives  $\Delta E' = \Delta E + (db/dE)\Delta E\Delta t$ . This can be combined with the other Taylor expansion in equ. (162) and yields the expression

$$\Delta N(E)\Delta E = \frac{dN(E)}{dE}b(E)\Delta E\Delta t + N(E)\frac{db(E)}{dE}\Delta E\Delta t, \quad (163)$$

that can be rewritten as

$$\frac{dN(E)}{dt} = \frac{d}{dE} [N(E)b(E)]. \quad (164)$$

Additionally, two other processes should be taken into account: When new particles get injected, a source term  $Q(E, t)$  appears on the right side. Furthermore, the number of particles in the volume can change due to diffusion with a scalar diffusion coefficient  $D$  or due to escape from the system, characterized by a lifetime  $\tau_{\text{life}}$ . Therefore, the general form of the diffusion-loss equation reads

$$\frac{dN(E)}{dt} = \frac{d}{dE} [N(E)b(E)] + \frac{N(E)}{\tau_{\text{life}}} + Q(E, t) + D\nabla^2 N(E). \quad (165)$$

This represents the time evolution of an energy spectrum of particles in a unit volume. Since in our case we are interested in a steady state solution, the left hand side of equ. (165) is assumed to be negligible. Furthermore, in this study, we do not take into account spatial diffusion, such that the last term in equ. (165) vanishes as well. The remaining steady-state diffusion loss equation can be solved by means of the Green's function:

$$G(E, E') = \frac{1}{b(E)} \exp\left(-\int_{E'}^E dy \frac{1}{\tau_{\text{life}}(y)b(y)}\right). \quad (166)$$

This is used in order to obtain from an injected source function of CRs,  $Q(E')$ , the resulting steady-state distribution,  $N(E)$ , after all cooling processes  $b(E)$  by performing the integral over the initial energy  $E'$ , which reads

$$N(E) = \int_E^{E_{\text{max}}} dE' Q(E') G(E, E'). \quad (167)$$

The upper limit  $E_{\text{max}}$  is given by the cut-off energy of the injected energy distribution. It is crucial to notice that the injected spectrum  $Q(E)$  is an injection rate, i.e., the numbers of particles being injected per unit energy and per unit time interval. Therefore, the characteristic timescale for the injection of electrons has to be considered. In the case of our simulations, electrons are instantaneously injected at remnants of core-collapse supernovae and are therefore directly connected to star formation. Consequently, the timescale of injection can be approximated by connecting the star formation rate  $\dot{M}_*$  with the gas mass  $M_{\text{gas}}$  of each cell, which yields

$$\tau_{\text{inj}} = \left(\frac{\dot{M}_*}{M_{\text{gas}}}\right)^{-1}. \quad (168)$$

### 3.2 Energy Loss Processes and Timescales

We now specify the different contributions to the energy loss rate  $b(E)$ , which we need for the calculation of the steady-state distribution of electrons from solving equ. (165). The following expressions for the different kinds of energy loss rates are given in units of  $\text{s}^{-1}$ , since the energies are measured in units of  $m_e c^2$ . A large amount of energy is lost due to the radiation processes explained above. First, for synchrotron radiation, we have from equ. (15) the energy loss rate

$$b_{\text{sync}}(E) = \frac{2q^4 B^2 \gamma^2 \beta^2 \sin^2 \alpha}{3m_e^2 c^3} = \frac{2}{3} r_0^2 c B^2 \gamma^2 \beta^2 \sin \alpha \quad (169)$$

for a specific pitch angle  $\alpha$ , whereas averaging over all angles leads to equ. (14).

Second, the electrons lose energy through inverse Compton scattering, which can in the simple case of Thomson scattering be described by equ. (58). In the general case, one needs to perform the integration

$$b_{\text{IC}}(E) = \int dE_1 E_1 \int dE \frac{dN_{\gamma,E}}{dt dE_1 dE}, \quad (170)$$

where for  $dN_{\gamma,E}/(dt dE_1)$ , in general, the expression in equ. (71) has to be used. For practical purposes, we are here using the Thomson-limit, i.e.

$$b_{\text{IC}}(E) = \frac{32}{9} \pi r_0^2 c \beta^2 \gamma^2 u_{\text{ph}}. \quad (171)$$

The photon energy density  $u_{\text{ph}}$  is a sum of the CMB and the radiation field of stars, which is not directly provided by the simulations and has to be derived from the given properties. First, we fix a SFR threshold  $\text{SFR}_{\text{thr}} = 10^{-8} M_{\odot}$  in order to define cells with a higher SFR to be actively star forming. Assuming that the emission of young stars is reradiated in the FIR due to the absorption by dust, the SFR can then be transformed into a corresponding FIR luminosity by adopting the relation obtained by Kennicutt (1998):

$$\frac{\text{SFR}}{M_{\odot} \text{ yr}^{-1}} = \epsilon 4.5 \times 10^{-44} \frac{L_{\text{FIR}}}{\text{erg s}^{-1}} = \epsilon 1.7 \times 10^{-10} \frac{L_{\text{FIR}}}{L_{\odot}}. \quad (172)$$

The parameter  $\epsilon = 0.79$  follows from adopting a Chabrier (2003) IMF, see Crain et al. (2010). Hence, we have the relation

$$\frac{L_{\text{FIR}}}{L_{\odot}} = 7.4 \times 10^9 \frac{\text{SFR}}{M_{\odot} \text{ yr}^{-1}}. \quad (173)$$

Since the FIR luminosity refers to the integrated luminosity in the wavelength range  $\lambda = 8 - 1000 \mu\text{m}$ , the corresponding Planck distribution yields a typical temperature of  $\sim 100 \text{ K}$ . The resulting photon energy density of a cell is then derived by summing up the flux arriving at each cell at a distance  $R_i$  from all actively star forming cells  $i$ , i.e.

$$u_{\text{ph}} = \sum_i \frac{L_{\text{FIR}}}{2\pi R_i^2 c}. \quad (174)$$

If the considered cell itself is a actively star forming one, the distance  $R_i$  is simply derived from the cell's volume,  $R_i = 3/(4\pi)V_i^{1/3}$ .

Third, bremsstrahlung losses have to be calculated similarly by

$$b_{\text{brems}}(E) = \int d\omega \hbar\omega \frac{dN}{dt d\omega}, \quad (175)$$

with  $dN/dt d\omega = c \sum n_s d\sigma_s/d\omega$ , where  $n_s$  and  $d\sigma_s/d\omega$  are the number density and differential cross-section of a species  $s$  respectively. In the case of a fully ionized medium, we only have protons and electrons, and the corresponding differential cross-sections are given in equ. (96), for electron-proton Bremsstrahlung, and equ. (100), for electron-electron Bremsstrahlung. Following Blumenthal and Gould (1970), this yields in the case of highly relativistic electrons for a fully ionized medium the expression

$$b_{\text{brems}}(E) = 4\alpha r_0^2 c n_{\text{H}} \beta \gamma \left[ \ln(2E) - \frac{1}{3} \right]. \quad (176)$$

Besides the energy loss processes that lead to the emission of photons, Coulomb interactions with the ambient medium have to be taken into account. They affect mainly the low-energy part of the electron spectrum. The expression for the energy loss rate has been derived by Gould (1972) and reads

$$b_{\text{Coul}} = \frac{3\sigma_T n_e c}{2\beta} \left[ \ln \left( \frac{m_e c^2 \beta \sqrt{\gamma - 1}}{\hbar \omega_{\text{pl}}} \right) - \ln(2) \left( \frac{\beta^2}{2} + \frac{1}{\gamma} \right) + \frac{1}{2} + \left( \frac{\gamma - 1}{4\gamma} \right)^2 \right] \quad (177)$$

with the plasma-frequency  $\omega_{\text{pl}} = \sqrt{4\pi e^2 n_e / m_e}$ .

All the discussed energy loss processes for CR electrons occur on characteristic timescales, with

$$\tau_{\text{loss}} = -\frac{E}{b(E)}. \quad (178)$$

These allow us to determine the importance of each energy loss process for a certain energy range. Furthermore, we have to specify the characteristic timescale of escape losses. We follow Lacki et al. (2010), who model the CR lifetime as

$$\tau_{\text{life}}^{-1} = \tau_{\text{diff}}^{-1} + \tau_{\text{wind}}^{-1}, \quad (179)$$

where the diffusion timescale is approximated by

$$\tau_{\text{diff}}(E) = 26 \text{Myr} \left( \frac{E}{3 \text{GeV}} \right)^{-1/2} \quad (180)$$

and the timescale for losses due to galactic winds by

$$\tau_{\text{wind}} \approx 300 \text{kyr}. \quad (181)$$

Since these timescales are in most cases longer than the corresponding timescales of other energy losses, they do not significantly contribute to the cooling process. This can be deduced from Fig. 11, which shows two examples of cells with different properties as described in the caption. In one case, the density is a factor of  $\sim 200$  higher, hence the energy loss timescale for Coulomb cooling happens faster by the same factor and thus, the timescale is lower by a factor of  $\sim 200$ . Similarly, since  $\tau_{\text{IC}} \propto u_{\text{ph}}^{-1}$ , an increased photon energy density of two orders of magnitude in the left panel compared to the right panel leads to a lowering of the energy loss timescale for IC scattering by  $\sim 10^2$ . For the synchrotron losses, we have  $b_{\text{synchr}} \propto B^2$ , hence for the corresponding energy loss timescale, we obtain a factor of  $(622/26)^{-2} \approx 23^{-2} \approx 2 \times 10^{-3}$  smaller in comparison to IC cooling. Only in the case of a low magnetic field combined with a low gas density and photon energy density, the CR lifetime can be lower than the cooling timescales of radiation processes and Coulomb cooling, and even there it only dominates in a limited energy range that covers  $\sim 2$  orders of magnitude. Hence, the resulting equilibrium distribution of electrons is in most cases not significantly changed by diffusive losses and galactic winds. To estimate the qualitative changes of the energy loss processes of an injected power law distribution of electrons, we write down the steady-state approximation of equ. (165), neglecting spatial diffusion and escape losses, i.e.,  $\tau_{\text{life}} \rightarrow \infty$ , yielding

$$\frac{d}{dE} [N(E)b(E)] = -Q(E, t). \quad (182)$$

Hence, we obtain for an injected spectrum  $Q(E) \propto E^{-a}$  an equilibrium spectrum with a new spectral index  $N(E) \propto E^{-p}$ . It is given by  $p = a + 1$  in the case where an energy loss process with  $b(E) \propto E^2$  dominates, hence, the spectrum gets steeper. On the other hand, if energy losses are predominant that depend only weakly on energy, with  $b(E) \propto \ln E$ , the spectral index is flattened to first order as  $p = a - 1$ . For  $b(E) \propto E$ , the spectral index remains unchanged.

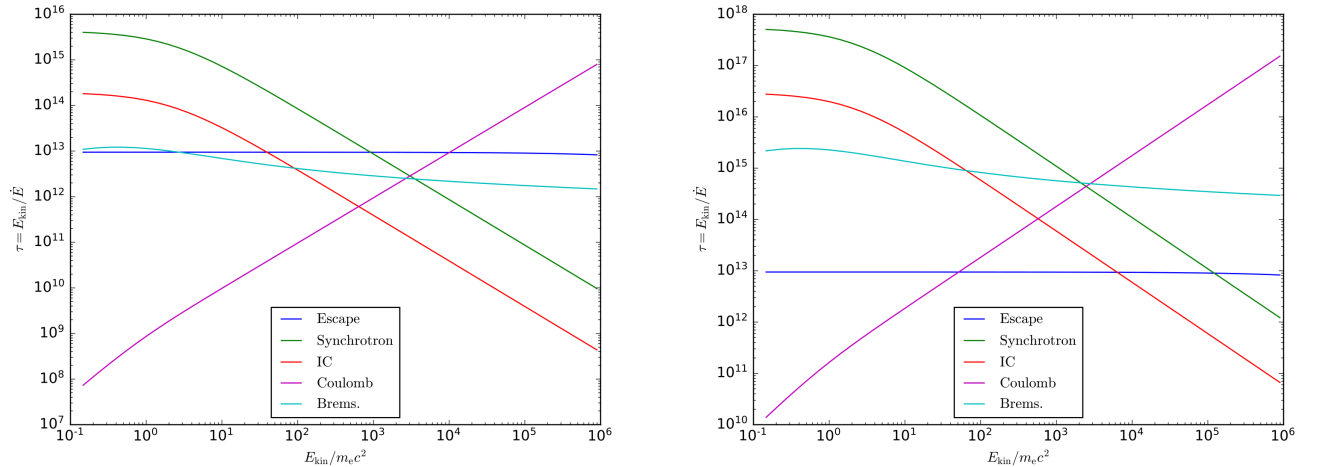


Figure 11: Energy loss timescales for two examples of cells with different properties in order to compare the importance of the cooling processes. In left panel, we have  $B = 622 \mu\text{G}$ ,  $n_e = 606 \text{ cm}^{-3}$  and  $u_{\text{ph}} = 10^{-7.1} \text{ erg cm}^{-3}$ , whereas in the right panel  $B = 26 \mu\text{G}$ ,  $n_e = 3 \text{ cm}^{-3}$  and  $u_{\text{ph}} = 10^{-9.2} \text{ erg cm}^{-3}$ .

### 3.3 Steady-State Spectra and Multi-Frequency Emission from Simulated Galaxies

We now apply the procedure explained in the previous section to a selected sample of four simulated galaxies. In order to get insight into the temporal evolution of galactic properties, we chose two different snapshots of the simulations. Since the SFR of the simulated galaxies peaks at around 0.1 to 0.2 Gyr, before it declines exponentially, we chose the snapshots at  $t = 0.1 \text{ Gyr}$  and  $1 \text{ Gyr}$  in order to compare a starburst to a quiescent phase. Furthermore, we are also interested in comparing the properties of a dwarf galaxy to a Milky-Way like galaxy and hence analyze the two different times for a galaxy with a halo mass of  $M_{200} = 10^{10} M_{\odot}$  as well as another one with  $M_{200} = 10^{12} M_{\odot}$ . Thus, we have four different simulations to undergo the procedure depicted in the flow-chart in Fig. 10, where we aim to calculate the CR electron equilibrium spectra and the resulting non-thermal multi-frequency emission. As we will point out later on, there is an important caveat here to keep in mind. Whereas the CR energy density increases quickly as the first stars are forming and after 0.1 Gyr it is in equilibrium with the thermal energy density, the magnetic field energy density grows slower, particularly in smaller galaxies (Pfrommer et al. 2017a). Hence, the magnetic dynamo has not saturated yet in the dwarf-galaxy in both chosen evolutionary stages and in the Milky-Way like galaxy in its starburst phase at  $t = 0.1 \text{ Gyr}$ . Moreover, to limit the calculation time, in this study the simulations with  $\sim 10^6$  initial gas cells within the virial radius have been used, therefore the results are only preliminary and have to be improved in the future, where we plan to apply the procedure to simulations with 10 times more cells and hence a significantly better resolution. Furthermore, the following input parameters have been fixed to perform a first test of the code and will be further examined in upcoming studies as well.

We adopt for the CR proton distribution a power-law for 64 momentum bins ranging from  $p_p/(m_p c) = 10^{-0.3}$  to  $10^6$  with a spectral index  $a_p = 2.1$  and a low-momentum cut-off  $q = 0.5$ , as well as an electron-to-proton ratio of  $K_{\text{ep}} = 10^{-3}$ . From the CR energy density  $\epsilon_{\text{CR}}$  we can thus deduce the initial electron energy distribution. Taking into account the distribution of CRs in Fig. 13, we select cells with  $\epsilon_{\text{CR}} > 10^{-14} \text{ erg cm}^{-3}$  and define them to be actively star-forming, if  $\text{SFR} > 10^{-8} M_{\odot} \text{ yr}^{-1}$ . The determination of the photon radiation field from the SFR (see equ. 174) is robust to changes of the chosen SFR threshold. Using the given magnetic field, gas density and the calculated photon energy density, we compute the steady-state spectrum of the primary electron population in each cell from equ. (167). On the other hand, from the CR proton spectrum, we obtain the spectrum of secondary electrons and positrons, which also

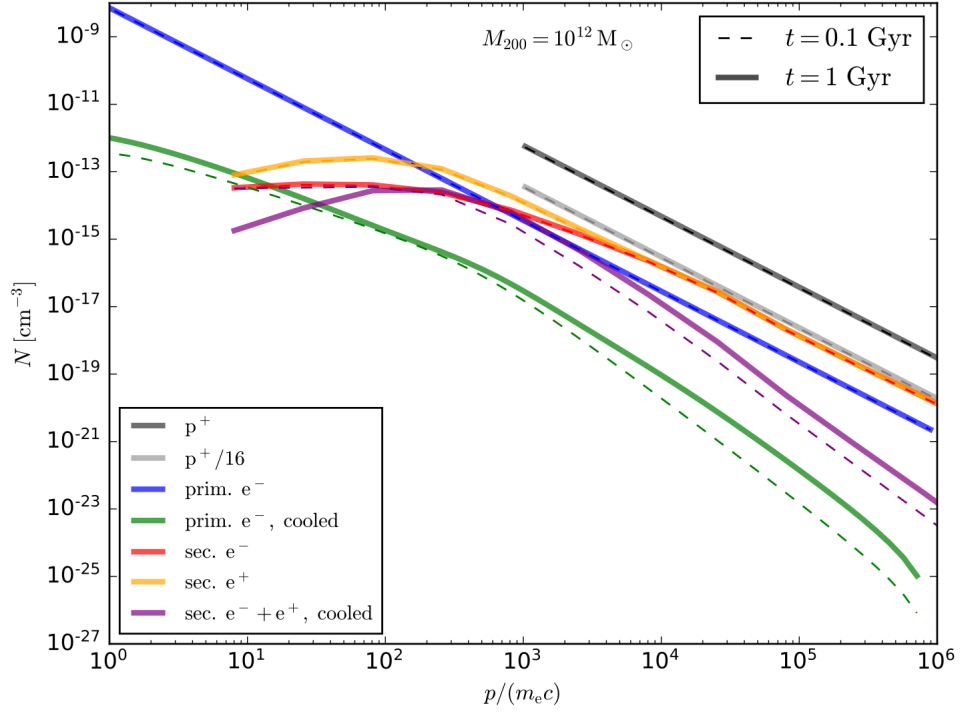
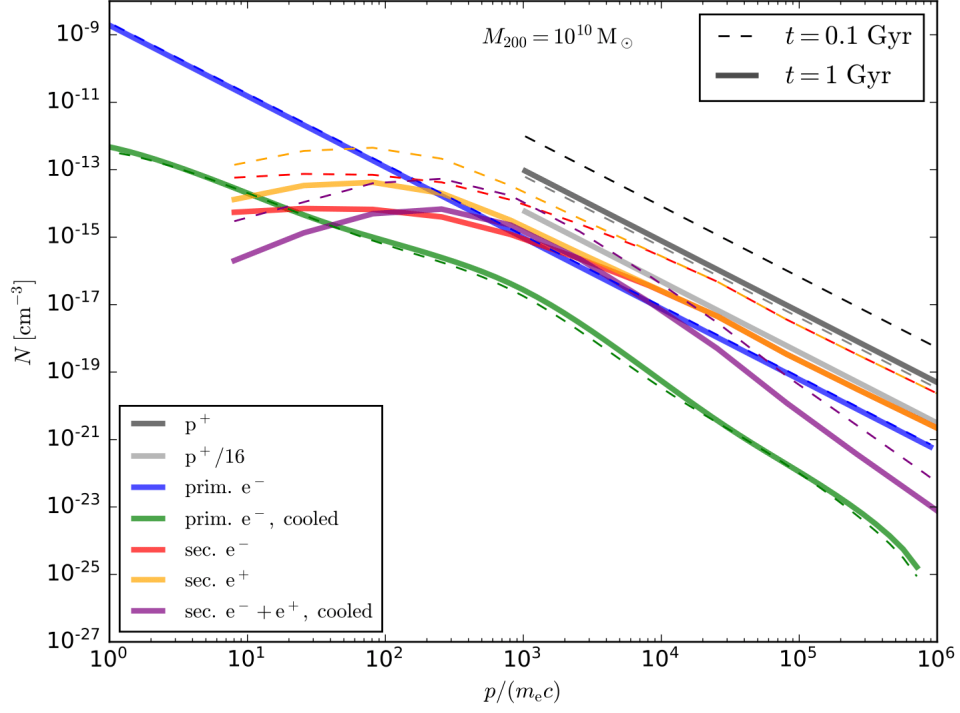


Figure 12: Total CR primary and secondary leptonic distributions before cooling and the steady-state spectra after cooling for two different halo masses. Additionally, the proton spectrum is shown, which coincides with the secondary electron spectrum if it is multiplied by 1/16, as estimated by equ. (152).

undergo the same cooling processes as the primary electrons. The summed up distributions of primary electrons as well as of secondary electrons and positrons for the two types of galaxies at different epochs of their evolution is shown in Fig. 12, before and after cooling, respectively. We can clearly identify the change of the spectral slope as we expect it from the discussion of the energy loss processes of electrons and their corresponding timescales in Section 3.2. Above Lorentz factors of  $\sim 10^3$ , the IC losses dominate the cooling of the electrons, since the timescale  $\tau_{\text{IC}}$  is the shortest in this regime (see Fig. 11). The dependence of the energy loss timescale on energy,  $b_{\text{IC}} \propto E^2$ , leads in the steady-state approximation (see equ. 182) to a spectral index which is steeper by 1 compared to the injected electron spectrum. For small electron momenta, the Coulomb losses, that only weakly depend on energy, are the predominant cooling process. Hence, the spectral index is increases by 1, flattening the spectrum in this regime.

The simple approximation of the secondary electron source function from a power-law distribution of protons is shown in Fig. 12, where the total proton spectrum has been divided by 16, which follows from equ. (152) with  $a_p = 2.1$ . This reproduces very well the exact calculation of the secondary electron/positron spectrum in a wide energy range. It only deviates in the low energy regime, where the more complex physical processes at the threshold of pion production have to be taken into account. Furthermore, we can clearly identify the excess of secondary positrons in comparison to secondary electrons near the threshold of pion production, which we expect from the difference in the cross-sections at low proton energies (see Fig. 8), since the isospin symmetry does not hold here.

The obtained steady-state spectra of primary electrons and secondary electrons/positrons as well as the proton spectrum are used as an input to my code to calculate the non-thermal radiation processes. Hence, we obtain a spatially resolved multi-frequency emission spectrum for our simulated galaxies that ranges from radio wavelengths, starting from  $10^6$  Hz, to the very-high gamma-ray regime, up to  $\sim 400$  TeV. We compute the emission of the primary electrons separately from the secondary leptons, in order to compare the different contributions to the overall spectrum and luminosities.

## 4 Results and Discussion

From the steady-state spectra of the primary and secondary electrons and positrons, we obtain the multi-frequency emission of the simulated galaxies: The emission maps of the leptonic radiation processes are shown in Fig. 15, 16, 18 and 20 for the different halo masses at the two time steps, respectively, separating primary from secondary emission. Furthermore, we show the maps of gamma-ray emission from hadronic interactions in Fig. 21. The maps show the emission projected along the line of sight, in a face-on and an edge-on view, respectively, by calculating  $S(\mathbf{n}) = \int \nu j_\nu(r, \mathbf{n}) dr$  for a unit vector  $\mathbf{n}$  perpendicular to the line of sight. For the synchrotron emission, the emission is shown at  $\nu = 1.4$  GHz and we take into account, that only the perpendicular component of the magnetic field contributes to this process. Hence, we calculate the pitch angle for each cell and the corresponding synchrotron emission as viewed by an observer face-on and edge-on. For all other processes, that occur mainly in the gamma-ray regime, the emission is shown at  $\nu = 10$  GeV/h. In Fig. 22, the emissivities of all cells have been integrated over the total volume to show the overall emission spectrum for each galaxy. The contribution of the primary component of each leptonic radiation process does not contribute significantly to the total emission, since it is around 2 orders of magnitudes below the corresponding secondary component. This can be already expected from Fig. 12, where we compare the cooled secondary momentum distributions with the primary ones. We notice, that any conclusion about the comparison of primary to secondary emission is only preliminary. We are limited in our calculation of the steady-state spectra of primary electrons to the cells where  $\text{SFR} \neq 0$ , since we neglect spatial diffusion and advection of CRs here and use equ. (168) for the typical timescale of the injection rate. This will be further improved in the future (Winner et al, in prep.).

Furthermore, the total emission spectra show the temporal evolution of the non-thermal emission. The radio spectra, arising from synchrotron emission (left panels in Fig. 22) show a strong increase over time from  $t = 0.1$  to  $t = 1$  Gyr. This is due to the growth of the magnetic field, whose exact impact on the synchrotron emission is discussed in more detail later on in this section. In contrast to that, the total emission spectra in the X-ray to gamma-ray regime (right panels in Fig. 22) hardly change over time.

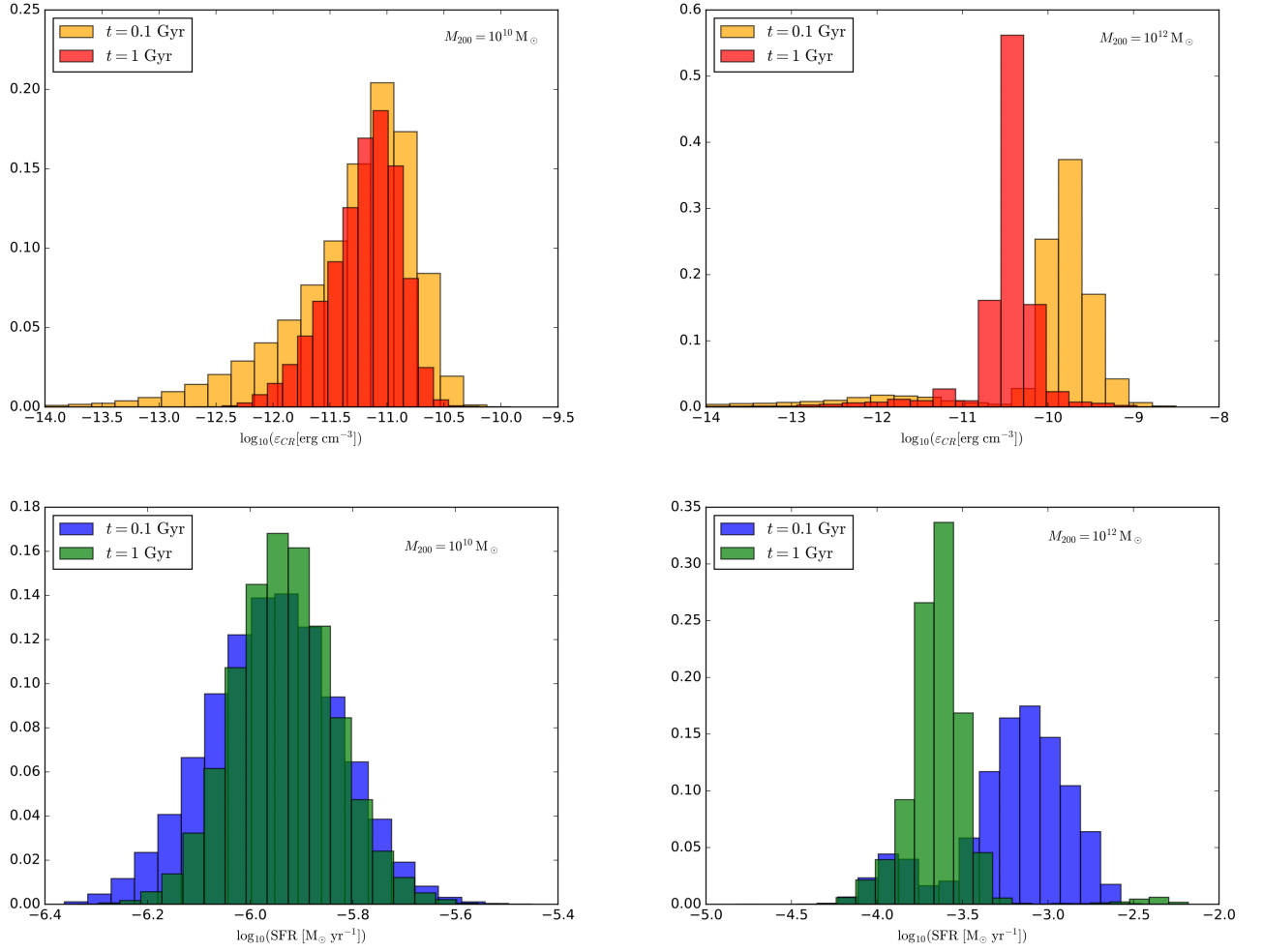


Figure 13: Normalized histograms of the CR energy density  $\varepsilon_{\text{CR}}$  (upper panels) and the SFR (lower panels) of the mesh cells for the four analyzed galaxies with different halo masses at different time steps.

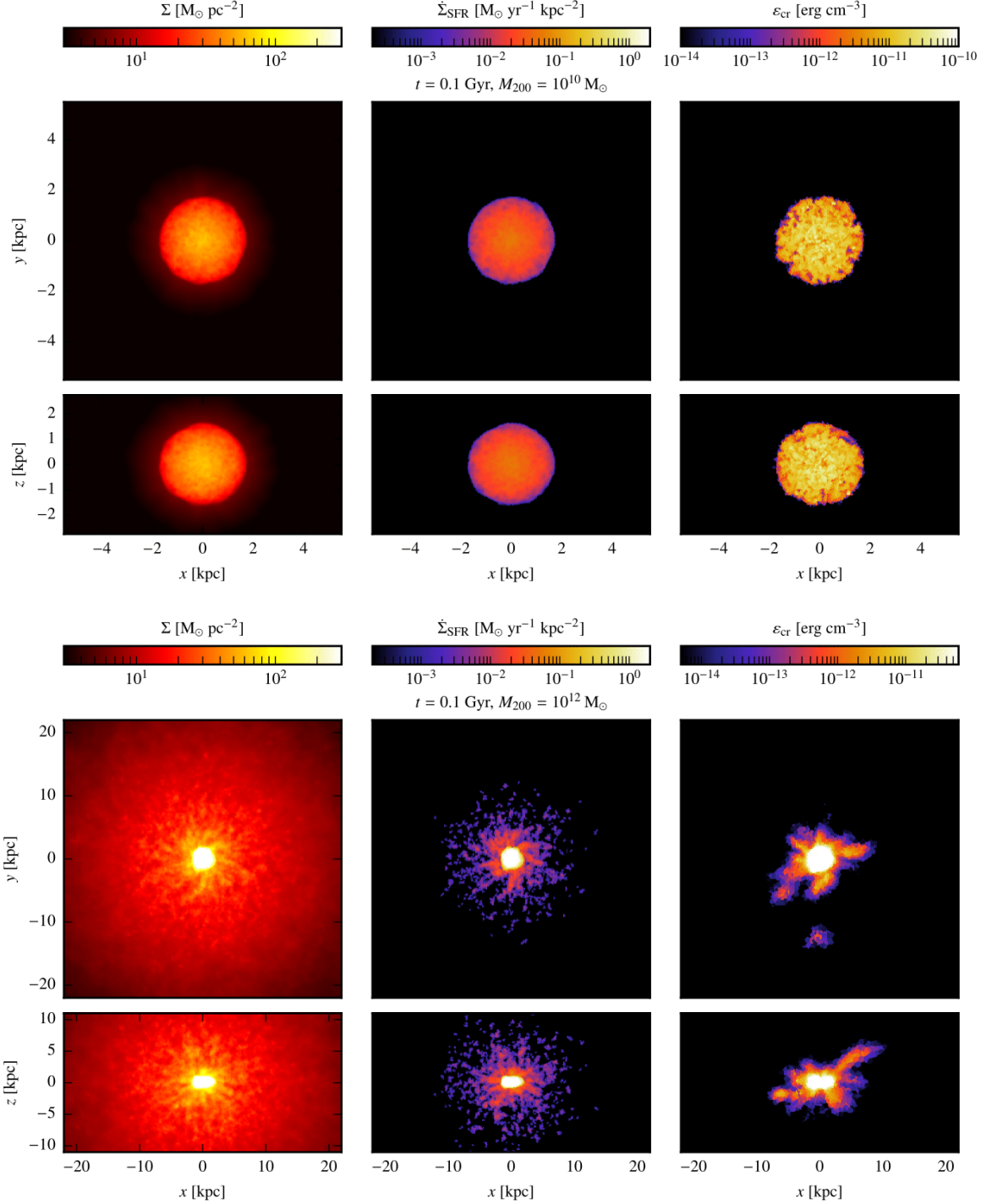


Figure 14: Properties of the simulated galaxies with  $M_{200} = 10^{10} M_{\odot}$  (upper panels) and  $M_{200} = 10^{12} M_{\odot}$  (lower panels), both at time  $t = 0.1$  Gyr: We show the projected gas surface density  $\Sigma$  and star formation rate surface density  $\dot{\Sigma}_{\text{SFR}}$ , as well as a slice of the CR energy density  $\epsilon_{\text{CR}}$ .

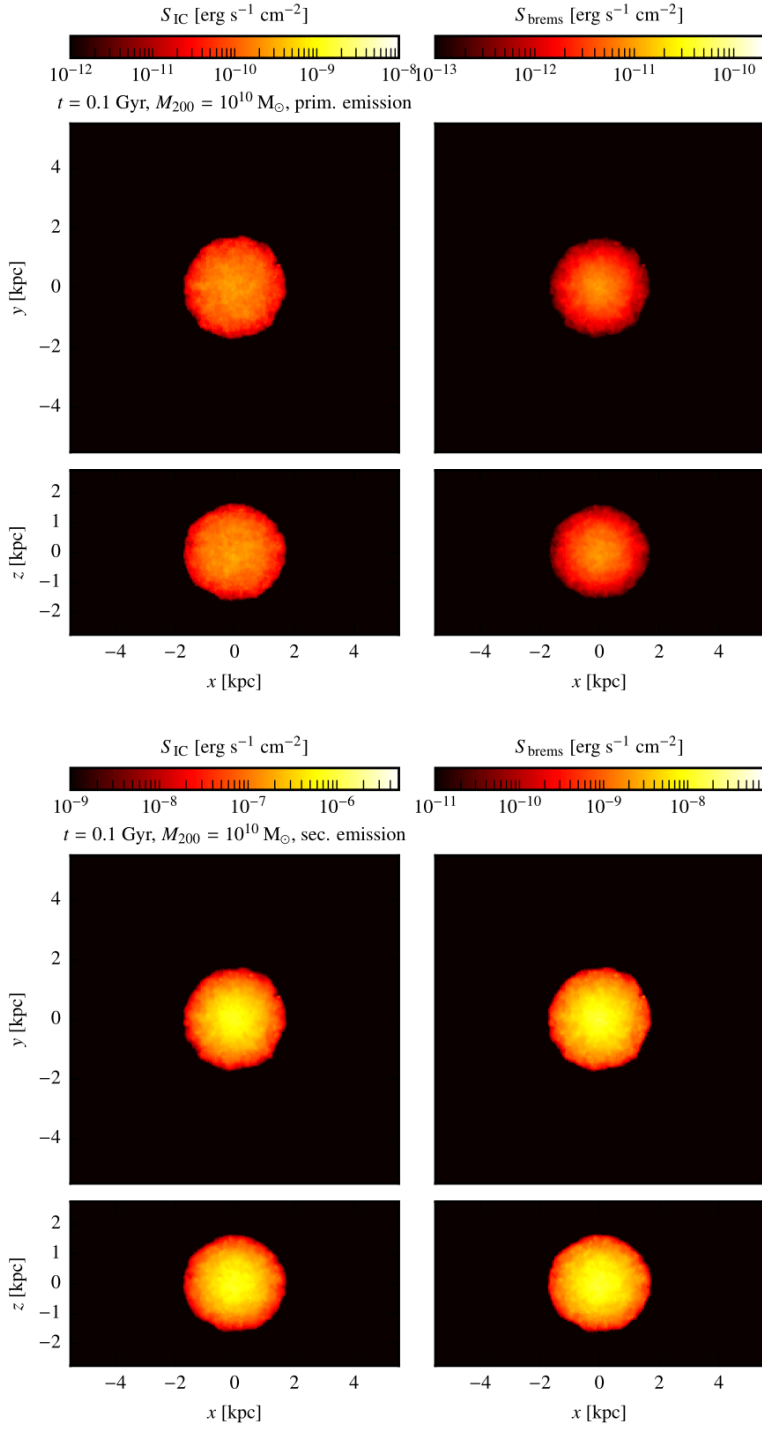


Figure 15: Non-thermal emission from the galaxy with  $M_{200} = 10^{10} M_{\odot}$  at  $t = 0.1 \text{ Gyr}$ , resulting from primary electrons (upper panels) and secondary electrons and positrons (lower panels): The IC (left panels) and bremsstrahlung emission (right panels) are shown at  $h\nu \approx 10 \text{ GeV}$ , respectively. The maps are projected along the line of sight and show a face-on view (upper part of each figure) and an edge-on view (lower part).

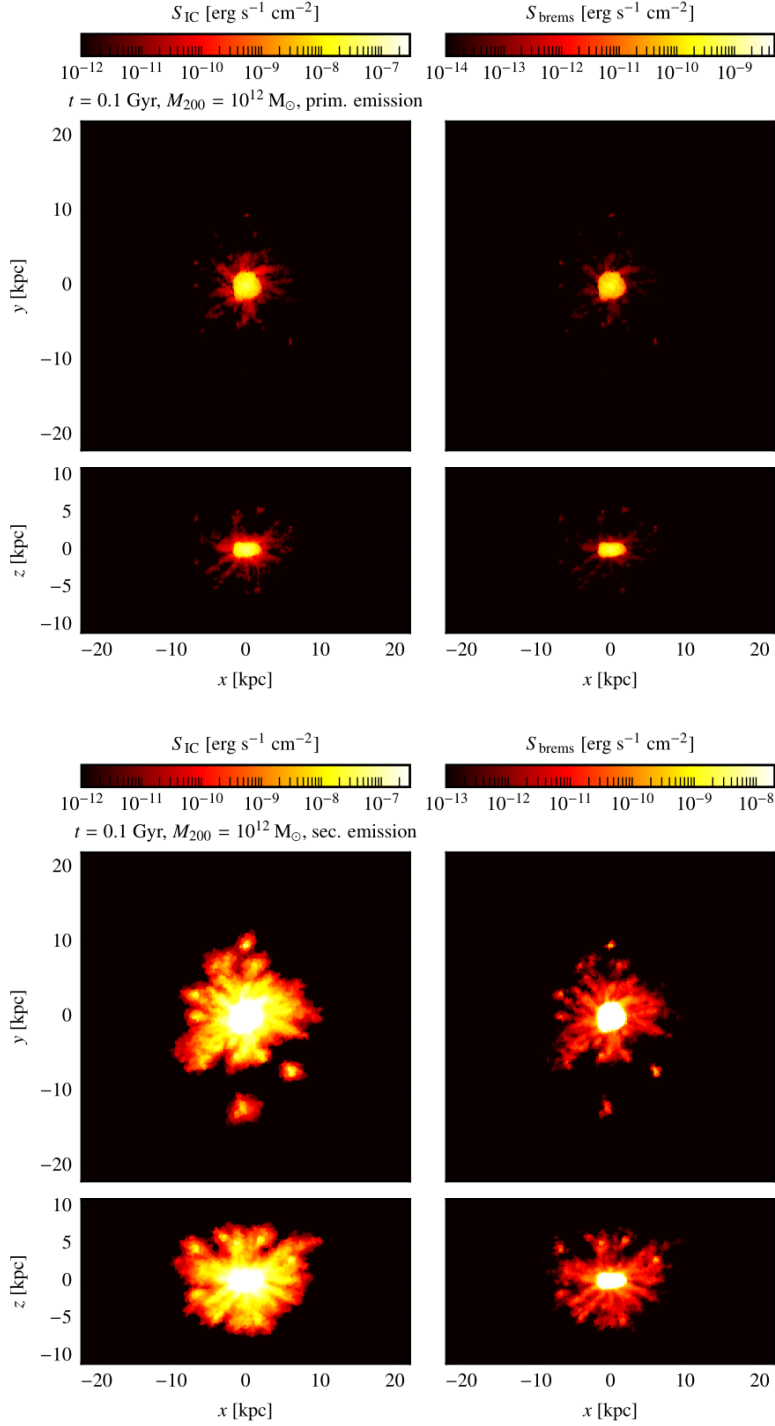


Figure 16: We show the same radiation processes as described in Fig. 15, but for  $M_{200} = 10^{12} M_{\odot}$  at  $t = 0.1$  Gyr.

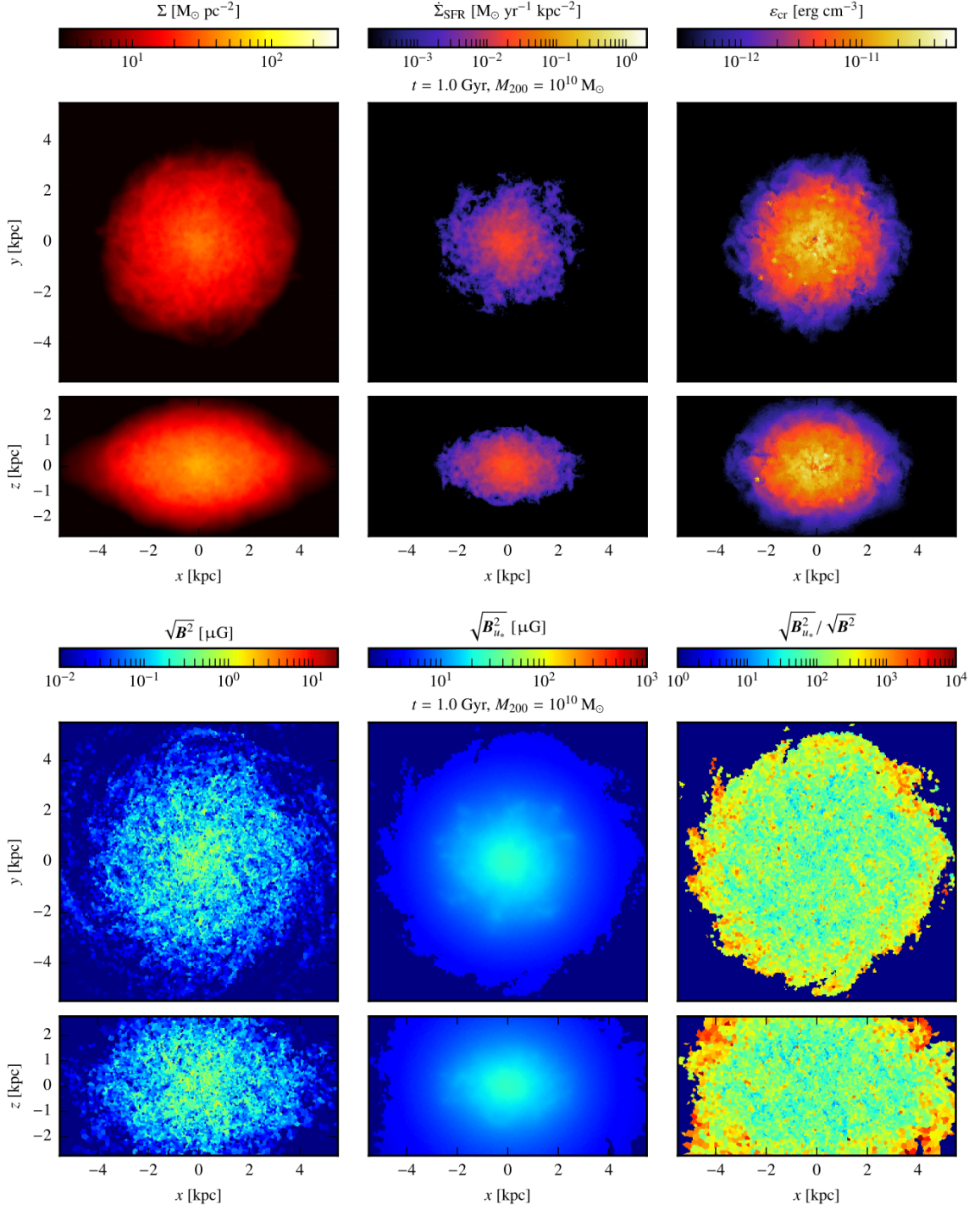


Figure 17: Properties of the simulated galaxy with  $M_{200} = 10^{10} M_{\odot}$  at time  $t = 1 \text{ Gyr}$ : We show the projected gas surface density  $\Sigma$  and star formation rate surface density  $\dot{\Sigma}_{\text{SFR}}$ , a slice of the CR energy density  $\varepsilon_{\text{CR}}$ , the magnetic field, the effective magnetic field for the stellar radiation energy density  $B_{u*}^2 = 8\pi u_*$  and their ratio.

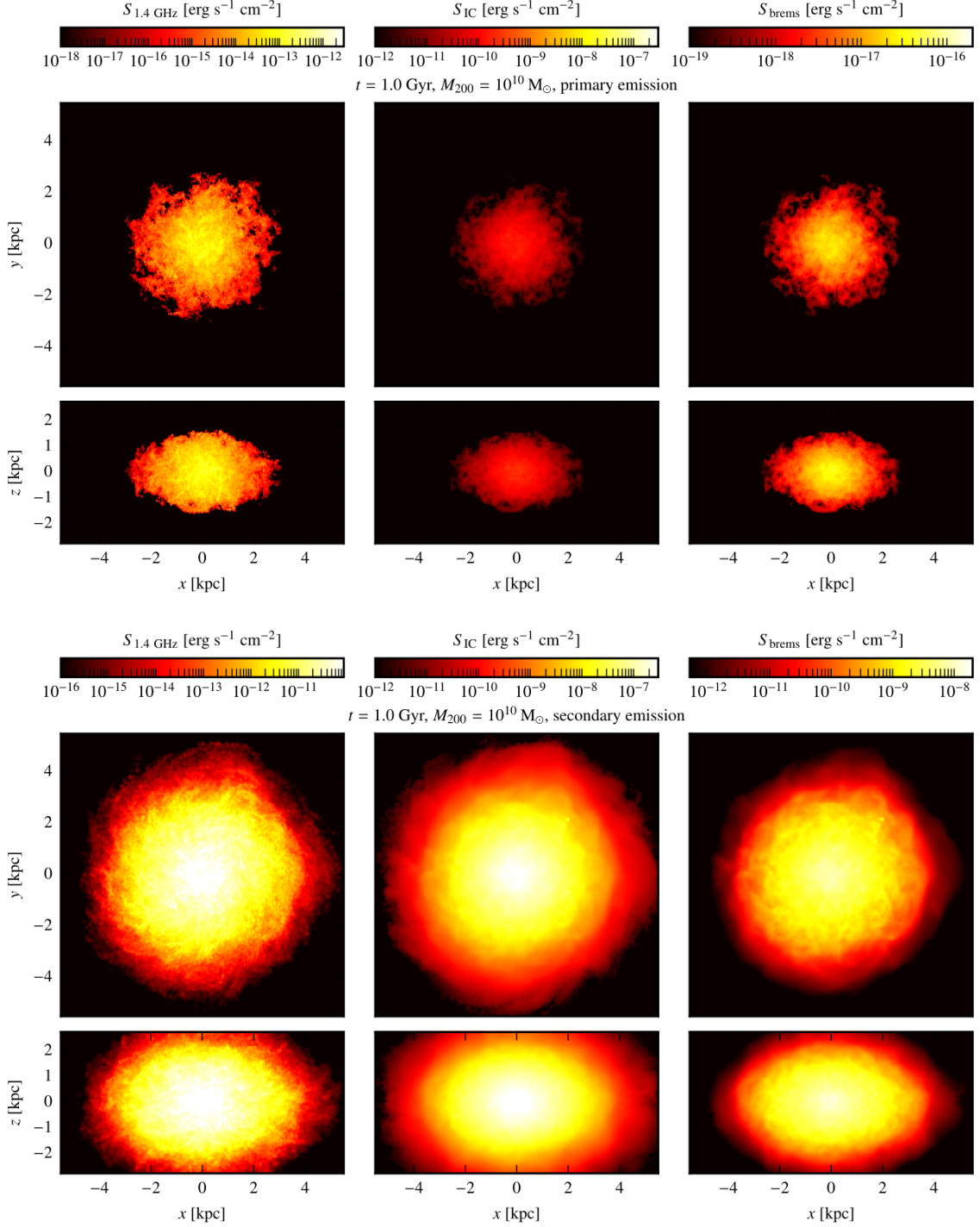


Figure 18: Non-thermal emission from the galaxy with  $M_{200} = 10^{10} M_{\odot}$  at  $t = 1 \text{ Gyr}$ , resulting from primary electrons (upper panels) and secondary electrons and positrons (lower panels): The Synchrotron emission (left panels) is shown at a frequency  $\nu = 1.4 \text{ GHz}$ , whereas the IC (middle panels) and bremsstrahlung emission (right panels) are shown at  $h\nu \approx 10 \text{ GeV}$ , respectively. The maps are projected along the line of sight and show a face-on view (upper part of each figure) and an edge-on view (lower part)

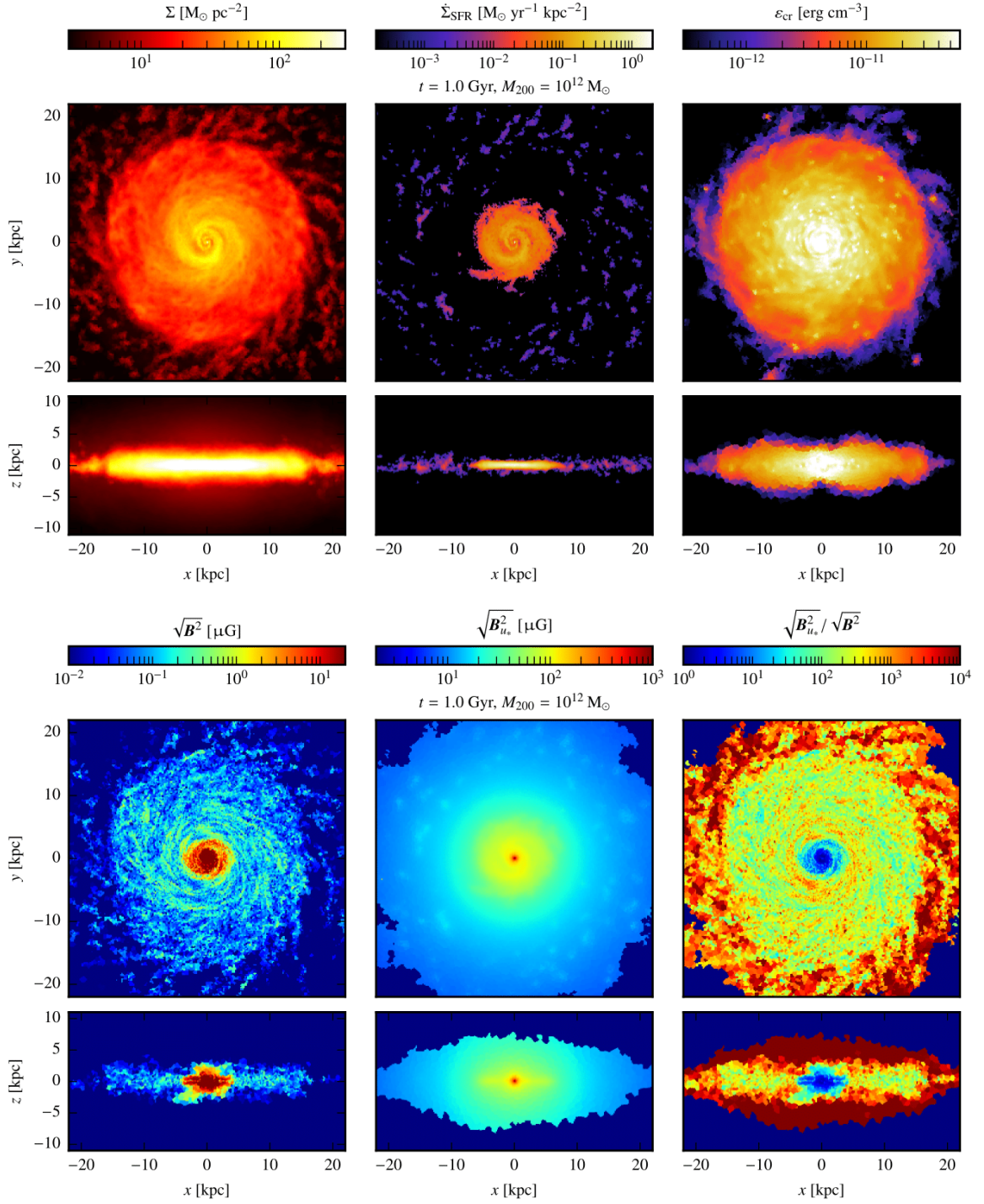


Figure 19: Same as Fig. 17, but for a galaxy with  $M_{200} = 10^{12} M_{\odot}$  at time  $t = 1$  Gyr.

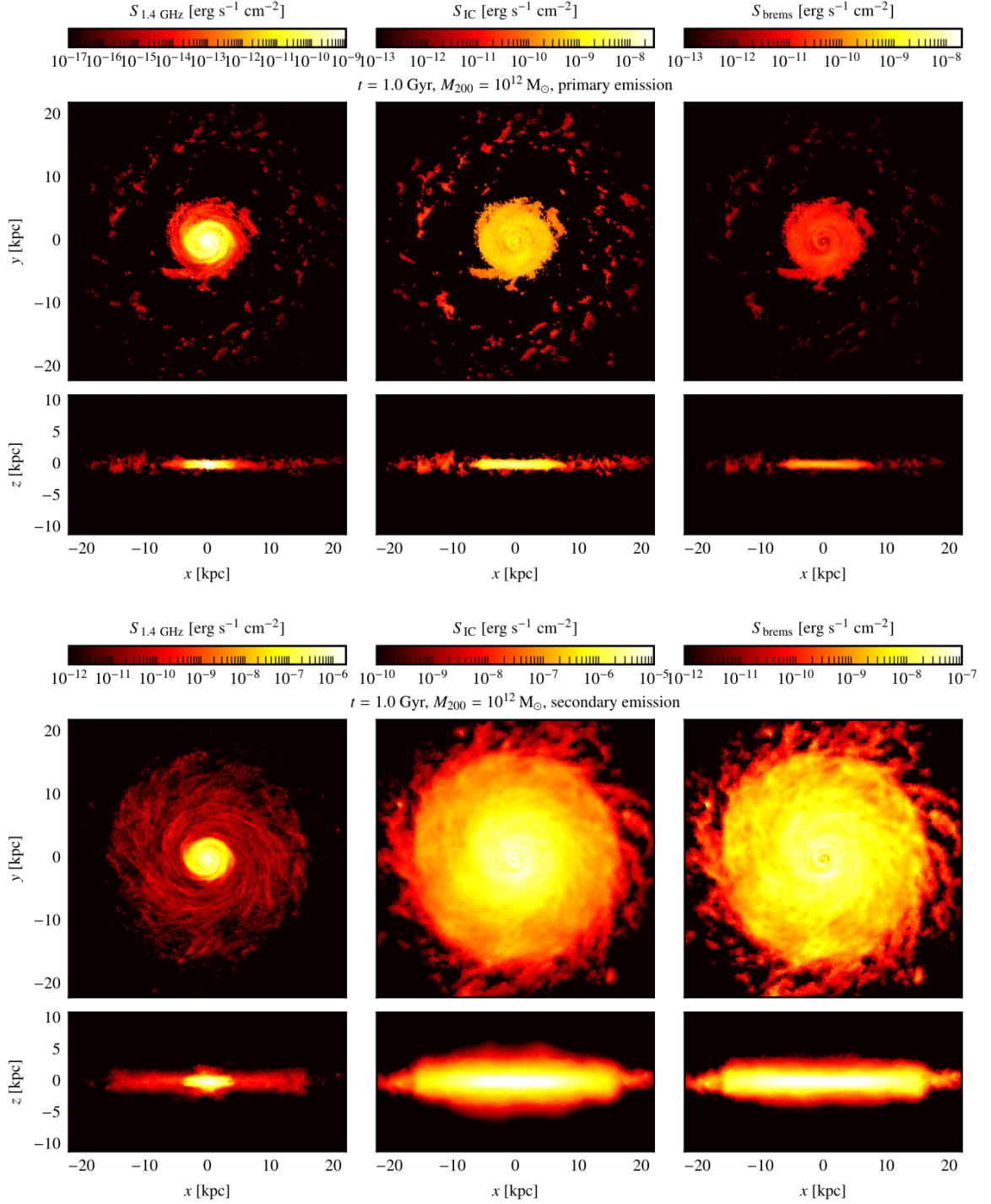


Figure 20: We show the same radiation processes as described in Fig. 18, but for  $M_{200} = 10^{12} M_{\odot}$  at  $t = 1$  Gyr.

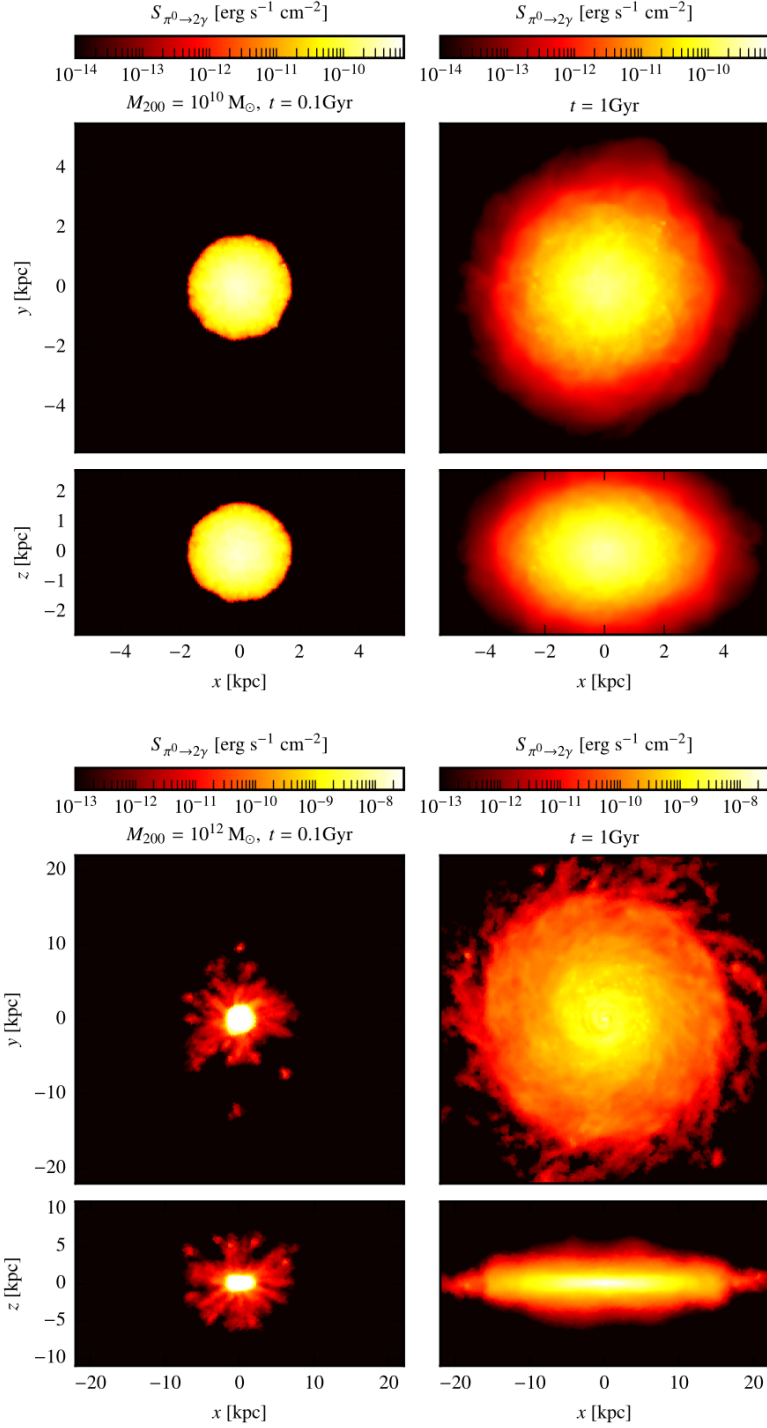


Figure 21: Gamma-ray emission maps from neutral pion decay for all four galaxy simulations at  $h\nu = 10$  GeV.

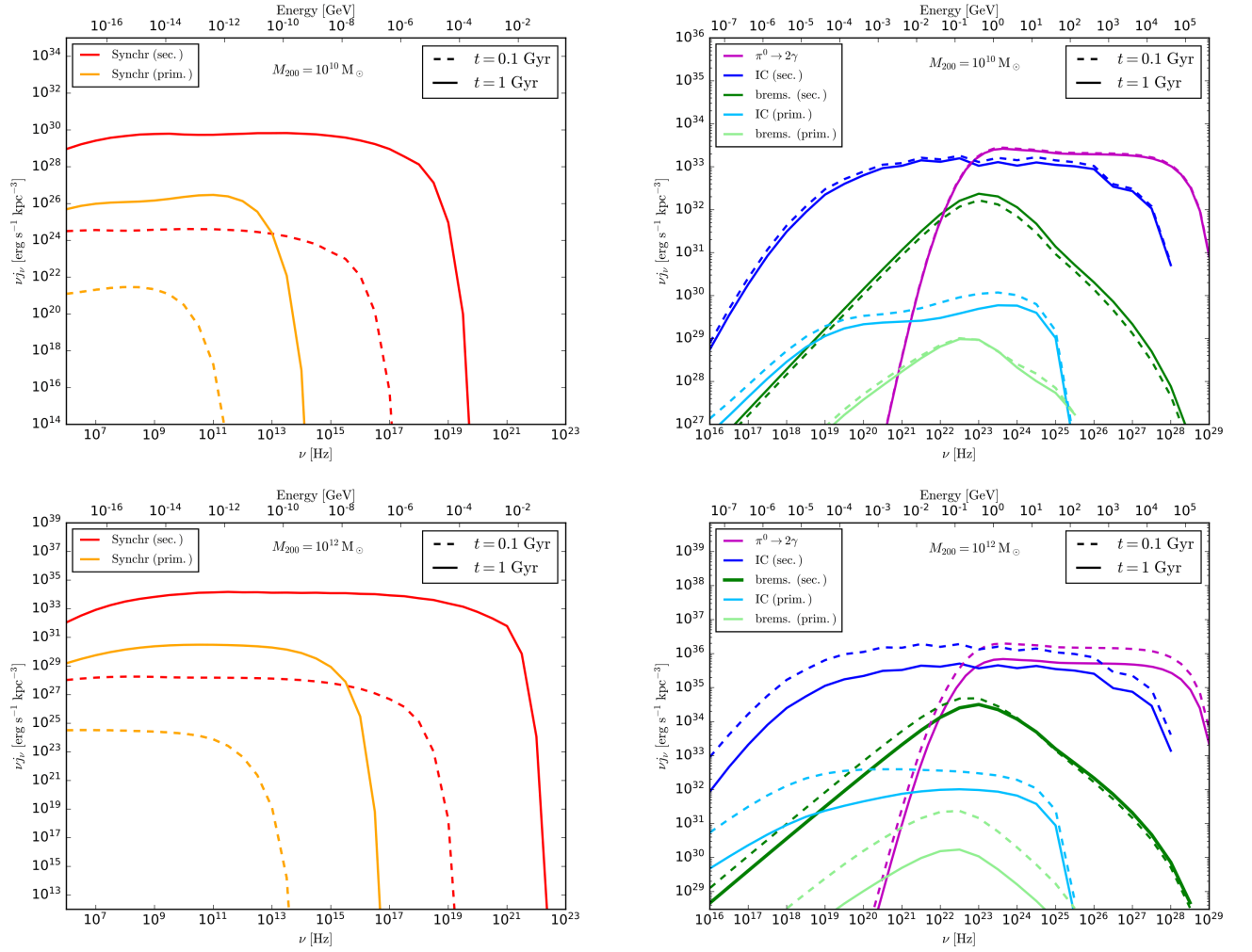


Figure 22: Total emission spectra integrated over the total volume of the galaxies in the radio (left panels) and the gamma-ray regime (right panels) for the dwarf galaxy (upper panels) and the Milky-Way like galaxy (lower panels). The spectra of the galaxies embedded in a halo of masses  $M_{200} = 10^{10} M_{\odot}$  and  $10^{12} M_{\odot}$  are shown in the upper and lower two panels, respectively. The spectrum is shown at  $t = 0.1$  Gyr (dashed lines) and  $t = 1$  Gyr (solid lines).

Solely the bremsstrahlung, gamma-ray emission from neutral pion decay and IC emission is decreased by factors of 2-10 in the case of the Milky Way-like galaxy. This is ascribed in the first to cases to the decrease in the mean density of the galaxy as it evolves over time. The IC emission is determined by the stellar radiation field and thus the decreasing IC flux is a consequence of the decreasing star-formation. We can already predict from the overall spectra that the IC emission will make a significant contribution to the gamma-ray luminosities, that we determine in the following.

We now reconcile our results with an analytical approach introduced by Pfrommer et al. (2017b) and further compare the calculated emission from the different types of galaxies to an observationally motivated relation between gamma-ray luminosity and star-formation rate. The latter can be further transformed into an FIR luminosity with equ. (173), since the UV radiation from young massive stars in star-forming galaxies is assumed to be absorbed by dust and reradiated in the FIR. Eventually, core-collapse SN explosions at the end of the life of a massive star lead to the acceleration of CRs. The hadronic interactions of CR protons and the interactions of CR electrons with the ambient medium and radiation fields lead to gamma-ray emission via neutral-pion decay as well as IC and Bremsstrahlung emission as explained above. Therefore, the gamma-ray radiation needs to be connected to the SFR and thus the FIR luminosity of a star-forming galaxy. Ackermann et al. (2012) and Rojas-Bravo and Araya (2016) recently observed the gamma-ray emission of star-forming galaxies with the Fermi telescope and found a tight linear correlation with the FIR luminosity, which Rojas-Bravo and Araya (2016) fit with the following expression:

$$\log\left(\frac{L_{0.1-100\text{ GeV}}}{\text{erg s}^{-1}}\right) = (1.12 \pm 0.08) \log\left(\frac{L_{8-1000\mu\text{m}}}{L_{\odot}}\right) + (27.9 \pm 0.8). \quad (183)$$

This relation is also reproduced by Pfrommer et al. (2017b), who performed the galaxy-formation simulations that have been used in this work. They used an analytical approach introduced by Pfrommer et al. (2008) to calculate the equilibrium spectrum of secondary electrons from a given CR proton energy distribution with a power-law spectral index of  $a$ . They include cooling by IC from CMB photons and synchrotron cooling and yield the expression

$$N_e(p) = \frac{16^{2-a_e} \sigma_{\text{pp}} n_{\text{N}} C_{\text{p}} m_e c^2}{(a_e - 2) \sigma_{\text{T}} (\varepsilon_B + \varepsilon_{\text{ph}})} \left(\frac{m_{\text{p}}}{m_e}\right)^{a_e-2} p^{-a_e}$$

where the slope of the electron spectrum is steeper as the injected proton spectrum by 1, i.e.,  $a_e = a_p + 1$ , due to synchrotron and IC cooling. The magnetic energy density is denoted by  $\varepsilon_B = B^2/(8\pi)$  and the photon energy density is  $\varepsilon_{\text{ph}}$ . Based on that, they derive analytical expressions for the non-thermal radiation processes. Most importantly, the dependencies of the synchrotron and IC emissivities on the magnetic field and the photon energy density are

$$j_{\text{synchr}} \propto \frac{B^{(a_e+1)/2}}{\varepsilon_B + \varepsilon_{\text{ph}}}$$

and

$$j_{\text{IC}} \propto \frac{1}{\varepsilon_B + \varepsilon_{\text{ph}}},$$

which is illustrated in their Fig. (3). This implies, that for low magnetic field energy densities  $\varepsilon_B \ll \varepsilon_{\text{ph}}$ , we have for a spectral index of  $a = 2.1$  and thus  $a_e = 3.1$ , that

$$j_{\text{synchr}} \propto B^{2.05}$$

and

$$j_{\text{IC}} \approx \text{const.}$$

On the other hand, we have for the case of a large magnetic field  $\varepsilon_B \gg \varepsilon_{\text{ph}}$ , that the emissivities scale as

$$j_{\text{synchr}} \propto B^{0.05} \approx \text{const.}$$

and

$$j_{\text{IC}} \propto B^{-2}.$$

Unlike Pfrommer et al. (2017b), I include as seed photons for IC scattering in addition to CMB photons also the photon radiation field from the stellar component, reradiated in the FIR, i.e.,  $\varepsilon_{\text{ph}} = u_{\text{CMB}} + u_*$ , see equ. (174). Consequently, much higher magnetic fields are needed, in order to reach the regime where the synchrotron cooling dominates the IC and overcomes the IC emissivity. This is rarely the case in the simulations analyzed here. In Fig. 17 and 19 the ratio of the magnetic field to the effective magnetic field of the stellar radiation field, where  $B_{u_*}^2 = 8\pi u_*$ , is shown in the lower right panel, respectively. We only have  $B \sim B_{u_*}$  at the time step  $t = 1$  Gyr in the very central region of the Milky-Way like galaxy and marginally occurring in the dwarf galaxy, otherwise  $B_{u_*} \gg B$ . This means that we are mostly in the case where IC cooling dominates synchrotron cooling and the addition of the stellar radiation field as seed photons for IC scattering has a significant effect on the cooling of the electron spectrum. Hence, we can verify the increase in the synchrotron emission over time depicted in the left panels of Fig. (22). The magnetic fields of the galactic discs embedded in the low- and high-mass halos are amplified by a factor of  $2.8 \times 10^2$  and  $3.6 \times 10^2$ , respectively (see Table 1). Since we are mainly in the regime, where  $B_{u_*} \gg B$  and thus  $j_{\text{synchr}} \propto B^{2.05}$ , we obtain an increase in the synchrotron emissivities by a factor of  $(2.8 \times 10^2)^{2.05} \approx 10^5$  and  $(3.6 \times 10^2)^{2.05} \approx 2 \times 10^5$  respectively, which agrees well with the obtained total spectra.

Nevertheless, there is a crucial point to notice here. First, galactic magnetic fields are believed to be amplified during their assembly phase due to the dynamo effect. Since the growth phase of the magnetic field happens at high redshift, it is not relevant for present day galaxies, which are already in the saturated regime. This was shown by Bernet et al. (2008), who found that the magnetic field strengths of galaxies at a redshift of  $z \approx 1.3$  are comparable to those observed in the local Universe. Thus, low-redshift galaxies that we observe today are in the phase where the dynamo has already saturated. As pointed out in Pfrommer et al. (2017a), the magnetic field strength in the simulation grows exponentially during the initial phase. Additionally, they show (see their right panel in Fig. 4), that the time for the magnetic field dynamo to saturate increases with smaller halo masses. Whereas the magnetic field of the Milky Way-like galaxy reaches this state already after 0.3 Gyr, it takes the dwarf galaxy at least a factor of 10 longer (Pfrommer et al, 2018 in prep.). Consequently, at the evolutionary state of the simulated galaxies that we analyze here, we have not reached this saturated regime yet, except for the Milky-Way like galaxy at  $t = 1$  Gyr. But in that case, the saturated state still might have only been reached in the central region and not yet in the outer parts of the galactic disc, since the dynamo saturates inside out. This will be improved by using the higher resolution simulations with  $\sim 10^7$  initial cells, that have been used by Pfrommer et al. (2017b), instead of  $\sim 10^6$ . Comparing their maps for the magnetic field of the Milky-Way like galaxy suggests that the low resolution dynamo saturates slower, such that the magnetic field strength is diminished in the case of less simulated cells. In fact, the total magnetic fields differ by a factor of 2 to 10. Consequently, by analyzing the galaxies at later times and with higher resolution, there might be more regions with  $B \gtrsim B_{u_*}$ . There, the synchrotron cooling becomes more important again, depending on the photon radiation field. Hence, including the stellar radiation field will be a next step to improve the description of the cooling processes, which in turn significantly influence the non-thermal leptonic emission.

Despite the fact that we do not use the same simulations, we want to compare the results obtained here with the analytical approach from Pfrommer et al. (2017a). Thus, we apply their formalism to the exact same simulations used here and compare the results. From the source function of the radiation processes, the total luminosity, in  $\text{erg s}^{-1}$ , in a certain energy range is obtained by integration over the total volume of the galaxy:

$$L_i(E_1, E_2) = \int_V \int_{E_1}^{E_2} q_i(E) E dE d^3x. \quad (184)$$

The index  $i$  corresponds to the radiation processes that we are analyzing. For the calculation of the gamma-ray luminosity in the Fermi-band, we have  $E_1 = 0.1$  GeV and  $E_2 = 100$  GeV. In this energy

range, the dominating radiation processes are IC emission and gamma-ray emission from neutral pion decay (see Fig. 22). Furthermore, the radio luminosity, typically in units of  $\text{erg s}^{-1} \text{Hz}^{-1}$ , is defined as

$$L_{1.4\text{GHz}} = \int_V j_{1.4\text{GHz}} d^3x.$$

We calculate the gamma-ray luminosity in the Fermi-band and use the total SFR of the galaxies to obtain the corresponding FIR luminosity with equ. (173). These two quantities are correlated in Fig. (23), which has been taken from Pfrommer et al. (2017b). It shows their results from the simulated galaxies with  $\sim 10^7$  cells, including different models of CR transport (light and dark blue symbols). They are consistent with the observations with the Fermi-LAT (Rojas-Bravo and Araya 2016), that include detections (filled symbols) and upper limits (open red symbols) for star-forming galaxies with and without AGN, respectively. In particular, the detections without AGNs (black filled circles) follow the best fit (orange line). Over-plotted are the gamma-ray and FIR luminosities of my galaxy sample (magenta and purple symbols), obtained from the calculation of the gamma-ray emission with my code. This is a sum of the IC emission and the gamma-ray emission from neutral pion decay.

For comparison with the simple analytical model for the gamma-ray source function by Pfrommer et al. (2017b), the black open symbols represent the gamma-ray luminosities, which have been obtained by applying their formalism to the exact same simulations I used, hence with the less simulated cells. Their approach includes the analytical approximation of the gamma-ray source function from neutral pion decay obtained by Pfrommer and Enßlin (2004), see equ. (136). For consistency, also the IC emission due to the CMB has been added, even though this does not make a significant contribution. The lower gamma-ray yield of the dwarf galaxy at  $t = 0.1$  Gyr compared to the best fit relation obtained by Pfrommer et al. (2017b) is likely due to the lower numerical resolution of the simulations, that we apply their and my formalism to.

My approach uses a more exact description of the hadronic interactions of CR protons with the ambient ISM, which deviates from the analytical model especially at low energies near the threshold of neutral pion production (see Fig. 9), where the analytical approximation over-predicts the emission. Hence, my approach yields a decreased gamma-ray luminosity. Note, that this effect is diminished, since the contribution of hadronic interactions from higher metallicity CRs additionally to interactions from protons with the ISM have been included here, in contrast to Pfrommer et al. (2017b), who only accounted for heavier nuclei in the ISM and not in the CRs themselves. As discussed in section 2.2.1, a nuclear enhancement factor of 1.8 accounts for both effects for Milky Way-like abundances (Yang et al. 2018). The number density of target nucleons in the ISM is defined as  $n_N = n_H + 4n_{\text{He}}$ , with the number density of hydrogen  $n_H = X_H \rho / m_p$ , the helium density  $n_{\text{He}} = ((1 - X_H)/4) \rho / m_p$  and the mass fraction of hydrogen  $X_H = 0.76$ . This yields  $n_N = \rho / m_p$ . Hence, when we use  $n_N$  as the target density of nucleons, we only need another factor of  $1.8X_H = 1.37$  to account for the interactions of heavier nuclei, such as the sub-threshold pion production. Consistently, this is very close to the value one obtains from dividing 1.8 by 1.3, where the latter is frequently used in the literature to account for heavier target nucleons in the ISM, but not in the CR composition.

Another difference in our model compared to the analytical approach is the contribution of IC emission to the total gamma-ray luminosity. In Pfrommer et al. (2017b), the gamma-ray luminosity from neutral pion decay dominates over the IC luminosity by a factor of  $\sim 5.7$  and was hence neglected in the analysis. In fact, applying their formalism to the simulations used here, we obtain ratios of  $L_{\pi^0 \rightarrow 2\gamma} / L_{\text{IC}} = 7.3$  to 9.9, whereas my method yields around 3 times lower values, from 1.9 to 2.4 (see Table 1). Consequently, we also account for the IC luminosity in our calculation of the total gamma-ray luminosity, since it is not negligible anymore.

Another observationally discovered linear relation is the FIR-radio correlation (see e.g. van der Kruit 1971, 1973; Condon 1992; Bell 2003). Since the FIR luminosity is correlated with the SFR of a galaxy, it should also be linked to the continuum radio emission of star-forming galaxies, which can be explained as synchrotron emission from CR electrons. If the radio emission was a perfect tracer for SF, star-forming galaxies would have to be electron calorimeters, which means that the electrons lose most of their energy by emitting radiation before they leave the galaxy, first proposed by Voelk (1989). The observations yield

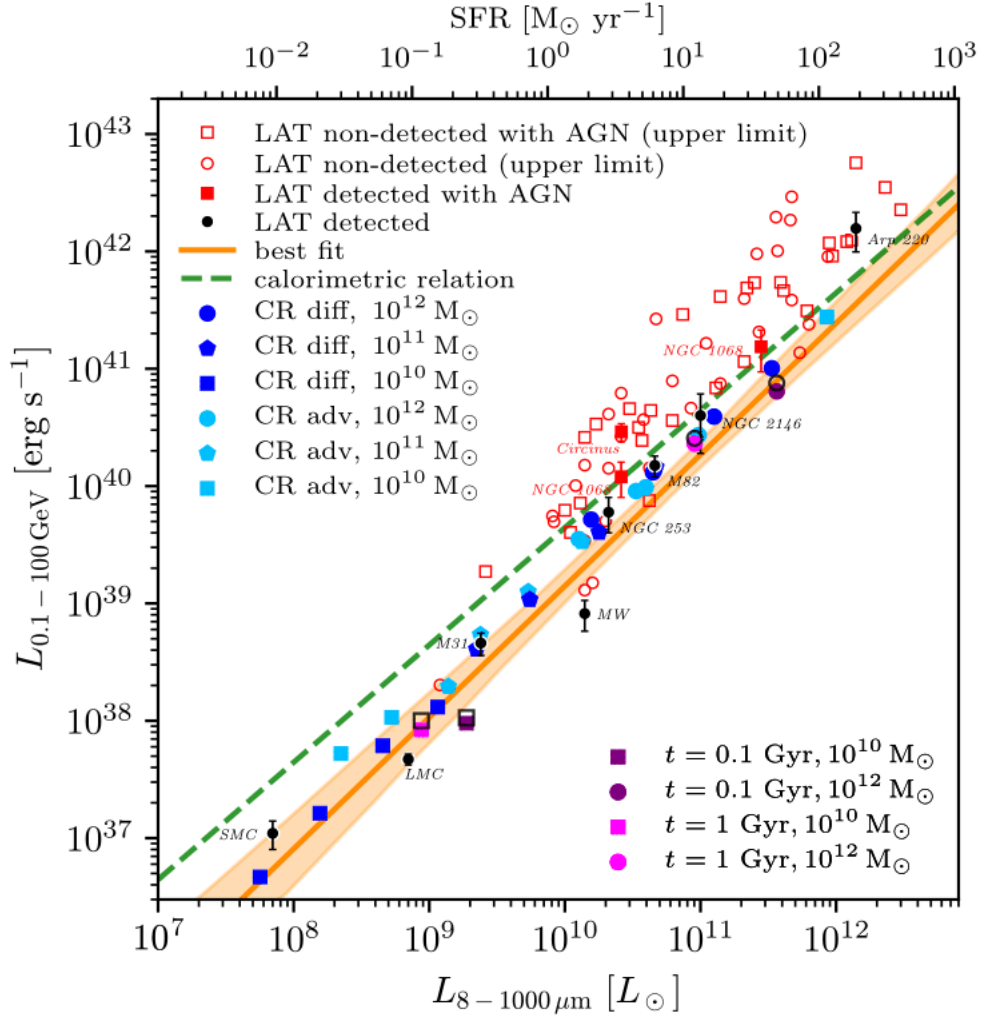


Figure 23: The FIR-gamma-ray relation, taken from Pfrommer et al. (2017b), where they show the FIR and gamma-ray luminosities for their simulated galaxies together with observational data from the Fermi-LAT (Rojas-Bravo and Araya 2016). The best fit is shown by the orange solid line, which deviates for low FIR luminosities from the calorimetric relation (green dashed line). The results from my code are shown with magenta and purple symbols, representing the two time steps that have been analyzed. The corresponding open black symbols show the results from the analytical results obtained by using the formalism by Pfrommer et al. (2017b), see text for details.

$M_{200}$	$t$ [Gyr]	SFR [ $M_{\odot} \text{ yr}^{-1}$ ]	$B$ [ $\mu\text{G}$ ]	$L_{8-1000\mu\text{m}}/L_{\odot}$	$L_{1.4 \text{ GHz, (face;edge)}}$ [ $\text{erg s}^{-1} \text{ Hz}^{-1}$ ]
$10^{10} M_{\odot}$	0.1	0.183	$1.77 \times 10^2$	$1.36 \times 10^9$	$3.85 \times 10^{19}; 3.71 \times 10^{19}$
$10^{10} M_{\odot}$	1	0.0854	$4.87 \times 10^4$	$6.36 \times 10^8$	$6.02 \times 10^{24}; 6.38 \times 10^{24}$
$10^{12} M_{\odot}$	0.1	35.41	$1.48 \times 10^3$	$2.64 \times 10^{11}$	$1.68 \times 10^{23}; 1.66 \times 10^{23}$
$10^{12} M_{\odot}$	1	8.82	$5.29 \times 10^5$	$6.57 \times 10^{10}$	$7.30 \times 10^{28}; 5.11 \times 10^{28}$

$M_{200}$	$t$ [Gyr]	$L_{\gamma}$ [ $\text{erg s}^{-1}$ ]	$L_{\pi^0 \rightarrow 2\gamma}$ [ $\text{erg s}^{-1}$ ]	$L_{\text{IC}}$ [ $\text{erg s}^{-1}$ ]	$L_{\pi^0 \rightarrow 2\gamma}/L_{\text{IC}}$
$10^{10} M_{\odot}$	0.1	$9.54 \times 10^{37}$	$6.26 \times 10^{37}$	$3.28 \times 10^{37}$	1.9
$10^{10} M_{\odot}$	1	$8.36 \times 10^{37}$	$5.91 \times 10^{37}$	$2.45 \times 10^{37}$	2.4
$10^{12} M_{\odot}$	0.1	$6.41 \times 10^{40}$	$4.46 \times 10^{40}$	$1.95 \times 10^{40}$	2.3
$10^{12} M_{\odot}$	1	$2.31 \times 10^{40}$	$1.56 \times 10^{40}$	$7.48 \times 10^{39}$	2.1

Table 1: Properties and luminosities of the simulated galaxies.

a correlation that is slightly steeper than a simple calorimetric conversion. It reads

$$\frac{L_{1.4 \text{ GHz}}}{\text{erg s}^{-1} \text{ Hz}^{-1}} = 2.26 \times 10^{28} \left( \frac{L_{8-1000\mu\text{m}}}{10^{10} L_{\odot}} \right)^{1.055} \quad (185)$$

and is reproduced very well by the simulations in Pfrommer et al. (2018, in prep.). The radio luminosities obtained in this work (see Table 1) are significantly lower than one would expect from equ. (185), where the difference decreases at later times, respectively. This arises from the fact that the magnetic field dynamo in these galaxies has not saturated yet, as discussed above. Since we analyze the galaxies at a stage where the magnetic field still grows exponentially and is thus much smaller than in more evolved galaxies observed at low redshift, the radio luminosities arising from synchrotron emission are much lower as well. Therefore, a further analysis of the simulations at later times is needed in order to compare it to the observational FIR-radio correlation, which refers to galaxies in the local Universe.

## 5 Conclusion

In this work I developed a framework to calculate the non-thermal emission from simulated galaxies originating from CRs. Therefore, all leptonic radiation processes have been elaborated considering a general momentum distribution of CR electrons in order to obtain their emitted synchrotron, IC and relativistic bremsstrahlung emission. Furthermore, I summarized the literature including the recent progress on modeling the hadronic interactions of CR protons with the ambient medium and reconciled the two latest descriptions for the cross section of pion production. This is used to determine the gamma-ray emission from neutral pion decay and the production of secondary electrons and positrons from an initial distribution of protons. The resulting code is then applied to magneto-hydrodynamic simulations of galaxies embedded in two different halo masses at two simulation times, respectively. These include a self-consistent treatment of CRs, that are injected at remnants of core-collapse SN.

First, we deduce from the CR energy density a proton spectrum, which also yields a primary electron spectrum assuming a proton-to-electron ratio. This is modified due to several energy loss processes, leading to an equilibrium spectrum under the assumption of a steady-state and neglecting spatial diffusion and advection of electrons. On the one hand, this primary spectrum of electrons enables us to calculate the leptonic emission with my code. On the other hand, the hadronic interactions of the initial distribution of protons with the ambient ISM leads to gamma-ray emission from neutral pion decay, which can also be obtained from my framework. Moreover, the code computes the production of secondary electrons and

positrons. It coincides well with the analytical approximation of the pion source function, that predicts a simple connection of the secondary electron to the proton spectrum, but yields a more exact description for low proton energies. This is then taken as another input for the leptonic radiation processes, after it has been “cooled” by means of the steady-state equation, taking into account the occurring energy losses. For the calculation of IC energy loss rate and the IC emission, we do not only take the contribution from seed photons of the CMB into account, but also a second contribution due to the stellar radiation field. Therefore, we assume that the stellar radiation from young stellar populations is mainly emitted in the UV, which is absorbed by dust and thus reradiated in the FIR. Hence, we connect the SFR to the corresponding FIR luminosity and calculate a photon radiation field for each cell as it receives from the surroundings.

We finally show spatially resolved maps of the radio and gamma-ray emission from four simulated galaxies as well as the total multi-frequency spectra. They show the time evolution of the radio synchrotron emission due to the growth of the magnetic field. Moreover, they indicate the minor contribution of the primary to the secondary leptonic emission. The emission calculated with an analytical approximation for the secondary electron equilibrium spectrum by Pfrommer et al. (2008) as well as an analytical description of the corresponding gamma-ray emission (Pfrommer et al. 2017b) seem to be in good agreement with my approach. But the more exact treatment of the pion production near the threshold leads to a decrease in the overall gamma-ray luminosity. Additionally, taking into account also the stellar radiation field, the IC emission seems to make a significant contribution as well. But still, the gamma-ray luminosities agree with the observationally motivated linear correlation with the FIR luminosity, deduced from the total SFR. In contrast to that, the radio luminosities are below the observed relation of FIR to radio luminosity, that holds for star-forming galaxies in the low-redshift universe. This is due to the fact that the simulations analyzed here are in an early stage of evolution. At that time, the magnetic field is still in the exponential growth phase, where the dynamo has not saturated yet. Thus, the magnetic fields are much smaller and hence the synchrotron radiation is much lower as well than in more evolved galaxies that we observe in the local Universe at low redshift.

We have now developed and tested a useful tool for the post-processing of simulations to generate non-thermal observables. It will be further optimized to be able to apply it to larger galaxy simulations and to analyze them at more time steps and halo masses. Furthermore, Winner et al. (2018, in prep.) develop a framework to follow the CR electron spectra attached to passive tracer particles in AREPO in order to evolve their spectra with time following the Fokker-Planck equation. This will lead to a much more realistic description of the CR spectra than the steady-state assumption made in this work. This enables us to refine the existing one-zone models of galaxies, where the FIR-radio correlation is explained by a “conspiracy scenario” (Lacki et al. 2010). This requires fine-tuning of several processes in different density regimes and the predicted spectral slopes of the synchrotron spectra are steeper than observed. Hence, with our framework we aim to gain more insight into the underlying physics of the observed FIR-radio and FIR-gamma-ray relations, which enables us to calibrate the strength of CR feedback as a function of galaxy mass and star formation rate ranging from quiescent galaxies to star-bursting phases.

## A Selbstständigkeitserklärung

Hiermit erkläre ich, dass ich die vorliegende Arbeit selbstständig und eigenhändig sowie ohne unerlaubte fremde Hilfe und ausschließlich unter Verwendung der aufgeführten Quellen und Hilfsmittel angefertigt habe. Die selbstständige und eigenständige Anfertigung versichert an Eides statt:

Berlin, den

-----  
Unterschrift

## B Danksagung

Ich möchte mich herzlich bei Prof. Dr. Christoph Pfrommer dafür bedanken, dass ich meine Masterarbeit in seiner Arbeitsgruppe am AIP anfertigen durfte. Die regelmäßigen Rücksprachen und der rege Austausch innerhalb der Gruppe haben mich sehr bereichert. Für die Hilfe bei jeglichen Zwischenfragen geht ein großes Dankeschön neben Christoph Pfrommer auch an Philipp Girichidis und Georg Winner. Ich freue mich sehr, meine Arbeit am AIP im Rahmen einer Promotion weiter führen zu dürfen. Außerdem möchte ich mich bei Prof. Dr. Dieter Breitschwerdt für die erneute Betreuung meiner Masterarbeit bedanken.

## References

- Milton Abramowitz and Irene A. Stegun, editors. *Handbook of Mathematical Functions with Formulas, Graphs and Mathematical Tables*. Dover Publications, Inc., New York, 1965.
- M. Ackermann, M. Ajello, A. Allafort, L. Baldini, J. Ballet, D. Bastieri, K. Bechtol, R. Bellazzini, B. Berenji, E. D. Bloom, E. Bonamente, A. W. Borgland, A. Bouvier, J. Bregeon, M. Brigida, P. Bruel, R. Buehler, S. Buson, G. A. Caliandro, R. A. Cameron, P. A. Caraveo, J. M. Casandjian, C. Cecchi, E. Charles, A. Chekhtman, C. C. Cheung, J. Chiang, A. N. Cillis, S. Ciprini, R. Claus, J. Cohen-Tanugi, J. Conrad, S. Cutini, F. de Palma, C. D. Dermer, S. W. Digel, E. d. C. e. Silva, P. S. Drell, A. Drlica-Wagner, C. Favuzzi, S. J. Fegan, P. Fortin, Y. Fukazawa, S. Funk, P. Fusco, F. Gargano, D. Gasparrini, S. Germani, N. Giglietto, F. Giordano, T. Glanzman, G. Godfrey, I. A. Grenier, S. Guiriec, M. Gustafsson, D. Hadasch, M. Hayashida, E. Hays, R. E. Hughes, G. Jóhannesson, A. S. Johnson, T. Kamae, H. Katagiri, J. Kataoka, J. Knödseder, M. Kuss, J. Lande, F. Longo, F. Loparco, B. Lott, M. N. Lovellette, P. Lubrano, G. M. Madejski, P. Martin, M. N. Mazziotta, J. E. McEnery, P. F. Michelson, T. Mizuno, C. Monte, M. E. Monzani, A. Morselli, I. V. Moskalenko, S. Murgia, S. Nishino, J. P. Norris, E. Nuss, M. Ohno, T. Ohsugi, A. Okumura, N. Omodei, E. Orlando, M. Ozaki, D. Parent, M. Persic, M. Pesce-Rollins, V. Petrosian, M. Pierbattista, F. Piron, G. Pivato, T. A. Porter, S. Rainò, R. Rando, M. Razzano, A. Reimer, O. Reimer, S. Ritz, M. Roth, C. Sbarra, C. Sgrò, E. J. Siskind, G. Spandre, P. Spinelli, Ł. Stawarz, A. W. Strong, H. Takahashi, T. Tanaka, J. B. Thayer, L. Tibaldo, M. Tinivella, D. F. Torres, G. Tosti, E. Troja, Y. Uchiyama, J. Vandenbroucke, G. Vianello, V. Vitale, A. P. Waite, M. Wood, and Z. Yang. GeV Observations of Star-forming Galaxies with the Fermi Large Area Telescope. *ApJ*, 755:164, August 2012. doi: 10.1088/0004-637X/755/2/164.
- F. A. Aharonian and A. M. Atoyan. Broad-band diffuse gamma ray emission of the galactic disk. *A&A*, 362:937–952, October 2000.
- F. A. Aharonian, S. R. Kelner, and A. Y. Prosekin. Angular, spectral, and time distributions of highest energy protons and associated secondary gamma rays and neutrinos propagating through extragalactic

- magnetic and radiation fields. *Phys. Rev. D*, 82(4):043002, August 2010. doi: 10.1103/PhysRevD.82.043002.
- V. N. Baier, V. S. Fadin, and V. A. Khoze. Photon bremsstrahlung in collision of high-energy electrons. *Soviet Phys. JETP*, 24(4):760, Apr 1967.
- M. G. Baring, D. C. Ellison, S. P. Reynolds, I. A. Grenier, and P. Goret. Radio to Gamma-Ray Emission from Shell-Type Supernova Remnants: Predictions from Nonlinear Shock Acceleration Models. *ApJ*, 513:311–338, March 1999. doi: 10.1086/306829.
- R. Beck and G. Golla. Far-infrared and radio continuum emission of nearby galaxies. *A&A*, 191:L9–L12, February 1988.
- R. Beig, J. Ehlers, U. Frisch, K. Hepp, W. Hillebrandt, D. Imboden, R. L. Jaffe, R. Kippenhahn, R. Lipowsky, H. v. Lo?hneysen , I. Ojima, H. A. H. A. Weidenmu?ller , J. Wess , and J. Zittartz. Physics and astrophysics of ultra-high-energy cosmic rays. In *Lecture Notes in Physics*, volume 576. Springer, 2001.
- A. R. Bell. The acceleration of cosmic rays in shock fronts. I. *MNRAS*, 182:147–156, January 1978. doi: 10.1093/mnras/182.2.147.
- E. F. Bell. Estimating Star Formation Rates from Infrared and Radio Luminosities: The Origin of the Radio-Infrared Correlation. *ApJ*, 586:794–813, April 2003. doi: 10.1086/367829.
- J. Beringer, J. F. Arguin, and R. M. et al. Barnett. Review of particle physics. *Phys. Rev. D*, 86:010001, Jul 2012. doi: 10.1103/PhysRevD.86.010001. URL <https://link.aps.org/doi/10.1103/PhysRevD.86.010001>.
- M. L. Bernet, F. Miniati, S. J. Lilly, P. P. Kronberg, and M. Dessauges-Zavadsky. Strong magnetic fields in normal galaxies at high redshift. *Nature*, 454:302–304, July 2008. doi: 10.1038/nature07105.
- H. Bethe and W. Heitler. On the Stopping of Fast Particles and on the Creation of Positive Electrons. *Proceedings of the Royal Society of London Series A*, 146:83–112, August 1934. doi: 10.1098/rspa.1934.0140.
- M. D. Bica and G. Helou. The 60 micron to 20 centimeter infrared-to-radio ratio within spiral galaxies. *ApJ*, 362:59–73, October 1990. doi: 10.1086/169243.
- S. R. Blattnig, S. R. Swaminathan, A. T. Kruger, M. Ngom, and J. W. Norbury. Parametrizations of inclusive cross sections for pion production in proton-proton collisions. *Phys. Rev. D*, 62(9):094030, November 2000. doi: 10.1103/PhysRevD.62.094030.
- G. R. Blumenthal and R. J. Gould. Bremsstrahlung, Synchrotron Radiation, and Compton Scattering of High-Energy Electrons Traversing Dilute Gases. *Reviews of Modern Physics*, 42:237–271, 1970. doi: 10.1103/RevModPhys.42.237.
- D. Breitschwerdt, J. F. McKenzie, and H. J. Voelk. Galactic winds. I - Cosmic ray and wave-driven winds from the Galaxy. *A&A*, 245:79–98, May 1991.
- G. Chabrier. The Galactic Disk Mass Function: Reconciliation of the Hubble Space Telescope and Nearby Determinations. *ApJ*, 586:L133–L136, April 2003. doi: 10.1086/374879.
- J. J. Condon. Radio emission from normal galaxies. *ARA&A*, 30:575–611, 1992. doi: 10.1146/annurev.aa.30.090192.003043.
- R. A. Crain, I. G. McCarthy, C. S. Frenk, T. Theuns, and J. Schaye. X-ray coronae in simulations of disc galaxy formation. *MNRAS*, 407:1403–1422, September 2010. doi: 10.1111/j.1365-2966.2010.16985.x.

- C. D. Dermer. Secondary production of neutral pi-mesons and the diffuse galactic gamma radiation. *A&A*, 157:223–229, March 1986a.
- C. D. Dermer. Binary collision rates of relativistic thermal plasmas. II - Spectra. *ApJ*, 307:47–59, August 1986b. doi: 10.1086/164391.
- G. Elwert. Verschaerfte berechnung von intensitaet und polarisation im kontinuierlichen roentgenspektrum. *Annalen der Physik*, 426(2):178–208, 1939. doi: 10.1002/andp.19394260206. URL <https://onlinelibrary.wiley.com/doi/abs/10.1002/andp.19394260206>.
- T. A. Enßlin, C. Pfrommer, V. Springel, and M. Jubelgas. Cosmic ray physics in calculations of cosmological structure formation. *A&A*, 473:41–57, October 2007. doi: 10.1051/0004-6361:20065294.
- V. F. Hess. Über Beobachtungen der durchdringenden Strahlung bei sieben Freiballonfahrten. *Physikalische Zeitschrift*, 13:1084–1091, November 1912.
- ENRICO Fermi. On the origin of the cosmic radiation. *Phys. Rev.*, 75:1169–1174, Apr 1949. doi: 10.1103/PhysRev.75.1169. URL <https://link.aps.org/doi/10.1103/PhysRev.75.1169>.
- T. K. Gaisser. *Cosmic rays and particle physics*. 1990.
- A. I. Golokhvastov. Koba-Nielsen-Olesen Scaling in Isospin-Coupled Reactions. *Physics of Atomic Nuclei*, 64:1841–1855, October 2001. doi: 10.1134/1.1414933.
- R.J. Gould. Energy loss of fast electrons and positrons in a plasma. *Physica*, 60(1):145 – 154, 1972. ISSN 0031-8914. doi: [https://doi.org/10.1016/0031-8914\(72\)90227-3](https://doi.org/10.1016/0031-8914(72)90227-3). URL <http://www.sciencedirect.com/science/article/pii/0031891472902273>.
- E. Haug. Contribution of electron-electron bremsstrahlung to solar hard X-radiation during flares. *Sol. Phys.*, 45:453–458, December 1975a. doi: 10.1007/BF00158461.
- E. Haug. Bremsstrahlung and pair production in the field of free electrons. *Zeitschrift Naturforschung Teil A*, 30:1099–1113, September 1975b. doi: 10.1515/zna-1975-0901.
- E. Haug. On the use of nonrelativistic bremsstrahlung cross sections in astrophysics. *A&A*, 326:417–418, October 1997.
- W. Heitler. *Quantum theory of radiation*. 1954.
- F. C. Jones. Calculated Spectrum of Inverse-Compton-Scattered Photons. *Physical Review*, 167:1159–1169, March 1968. doi: 10.1103/PhysRev.167.1159.
- E. Kafexhiu. Parametrization of the nucleus-nucleus  $\gamma$  -ray production cross sections below 100 GeV/nucleon: Subthreshold pions and hard photons. *Phys. Rev. C*, 94(6):064603, December 2016. doi: 10.1103/PhysRevC.94.064603.
- E. Kafexhiu, F. Aharonian, A. M. Taylor, and G. S. Vila. Parametrization of gamma-ray production cross sections for p p interactions in a broad proton energy range from the kinematic threshold to PeV energies. *Phys. Rev. D*, 90(12):123014, December 2014. doi: 10.1103/PhysRevD.90.123014.
- T. Kamae, N. Karlsson, T. Mizuno, T. Abe, and T. Koi. Parameterization of  $\gamma$ ,  $e^{+/-}$ , and Neutrino Spectra Produced by p-p Interaction in Astronomical Environments. *ApJ*, 647:692–708, August 2006. doi: 10.1086/505189.
- S. R. Kelner, F. A. Aharonian, and V. V. Bugayov. Energy spectra of gamma rays, electrons, and neutrinos produced at proton-proton interactions in the very high energy regime. *Phys. Rev. D*, 74(3):034018, August 2006. doi: 10.1103/PhysRevD.74.034018.
- R. C. Kennicutt, Jr. Star Formation in Galaxies Along the Hubble Sequence. *ARA&A*, 36:189–232, 1998. doi: 10.1146/annurev.astro.36.1.189.

- P. Kroupa. On the variation of the initial mass function. *MNRAS*, 322:231–246, April 2001. doi: 10.1046/j.1365-8711.2001.04022.x.
- B. C. Lacki, T. A. Thompson, and E. Quataert. The Physics of the Far-infrared-Radio Correlation. I. Calorimetry, Conspiracy, and Implications. *ApJ*, 717:1–28, July 2010. doi: 10.1088/0004-637X/717/1/1.
- M. S. Longair. *High Energy Astrophysics*. February 2011.
- K. Mannheim and R. Schlickeiser. Interactions of cosmic ray nuclei. *A&A*, 286:983–996, June 1994.
- F. Miniati. COSMOCR: A numerical code for cosmic ray studies in computational cosmology. *Computer Physics Communications*, 141:17–38, November 2001. doi: 10.1016/S0010-4655(01)00293-4.
- I. V. Moskalenko and A. W. Strong. Production and Propagation of Cosmic-Ray Positrons and Electrons. *ApJ*, 493:694–707, January 1998. doi: 10.1086/305152.
- E. J. Murphy, G. Helou, J. D. P. Kenney, L. Armus, and R. Braun. Connecting Far-Infrared and Radio Morphologies of Disk Galaxies: Cosmic-Ray Electron Diffusion After Star Formation Episodes. *ApJ*, 678:828–850, May 2008. doi: 10.1086/587123.
- R. Pakmor, V. Springel, A. Bauer, P. Mocz, D. J. Munoz, S. T. Ohlmann, K. Schaal, and C. Zhu. Improving the convergence properties of the moving-mesh code AREPO. *MNRAS*, 455:1134–1143, January 2016. doi: 10.1093/mnras/stv2380.
- C. Pfrommer and T. A. Enßlin. Constraining the population of cosmic ray protons in cooling flow clusters with  $\gamma$ -ray and radio observations: Are radio mini-halos of hadronic origin? *A&A*, 413:17–36, January 2004. doi: 10.1051/0004-6361:20031464.
- C. Pfrommer, T. A. Enßlin, and V. Springel. Simulating cosmic rays in clusters of galaxies - II. A unified scheme for radio haloes and relics with predictions of the  $\gamma$ -ray emission. *MNRAS*, 385:1211–1241, April 2008. doi: 10.1111/j.1365-2966.2008.12956.x.
- C. Pfrommer, R. Pakmor, K. Schaal, C. M. Simpson, and V. Springel. Simulating cosmic ray physics on a moving mesh. *MNRAS*, 465:4500–4529, March 2017a. doi: 10.1093/mnras/stw2941.
- C. Pfrommer, R. Pakmor, C. M. Simpson, and V. Springel. Simulating Gamma-Ray Emission in Star-forming Galaxies. *ApJ*, 847:L13, October 2017b. doi: 10.3847/2041-8213/aa8bb1.
- C. Rojas-Bravo and M. Araya. Search for gamma-ray emission from star-forming galaxies with Fermi LAT. *MNRAS*, 463:1068–1073, November 2016. doi: 10.1093/mnras/stw2059.
- G. B. Rybicki and A. P. Lightman. *Radiative Processes in Astrophysics*. June 1986.
- V. Springel. E pur si muove: Galilean-invariant cosmological hydrodynamical simulations on a moving mesh. *MNRAS*, 401:791–851, January 2010. doi: 10.1111/j.1365-2966.2009.15715.x.
- F. W. Stecker. The Cosmic  $\gamma$ -Ray Spectrum from Secondary Particle Production in Cosmic-Ray Interactions. *Ap&SS*, 6:377–389, March 1970. doi: 10.1007/BF00653856.
- F. W. Stecker. Cosmic gamma rays. *NASA Special Publication*, 249, 1971.
- S. A. Stephens and G. D. Badhwar. Production spectrum of gamma rays in interstellar space through neutral pion decay. *Ap&SS*, 76:213–233, May 1981. doi: 10.1007/BF00651256.
- P. C. van der Kruit. Observations of core sources in Seyfert and normal galaxies with the Westerbork synthesis radio telescope at 1415 MHz. *A&A*, 15:110–122, November 1971.
- P. C. van der Kruit. High-resolution Radio Continuum Observations of Bright Spiral Galaxies at 1415 MHz: A General Discussion. *A&A*, 29:263, December 1973.

- H. J. Voelk. The correlation between radio and far-infrared emission for disk galaxies - A calorimeter theory. *A&A*, 218:67–70, July 1989.
- K. C. Westfold. The Polarization of Synchrotron Radiation. *ApJ*, 130:241, July 1959. doi: 10.1086/146713.
- R.-z. Yang, E. Kafexhiu, and F. Aharonian. On the shape of the gamma-ray spectrum around the “ $\pi^0$ -bump”. *ArXiv e-prints*, March 2018.
- V. Zeković, B. Arbutina, A. Dobardžić, and M. Z. Pavlović. Relativistic Non-Thermal Bremsstrahlung Radiation. *International Journal of Modern Physics A*, 28:1350141, November 2013. doi: 10.1142/S0217751X13501418.
- E. G. Zweibel. The microphysics and macrophysics of cosmic rays. *Physics of Plasmas*, 20(5):055501, May 2013. doi: 10.1063/1.4807033.